



TUM School of Natural Sciences

Technische Universität München

Nuclear Structure Investigations of Light Nuclei  
with the R<sup>3</sup>B Experiment

Tobias Jenegger

Vollständiger Abdruck der von der TUM School of Natural Sciences der Technischen  
Universität München zur Erlangung des akademischen Grades eines  
Doktors der Naturwissenschaften (Dr. rer. nat.)  
genehmigten Dissertation.

Vorsitz:	TBA
Prüfer*innen der Dissertation:	1. TBA
	2. TBA

Die Dissertation wurde am DATUM-HIER bei der Technischen Universität München  
eingereicht und durch die TUM School of Natural Sciences am DATUM-HIER  
angenommen.





TUM School of Natural Sciences

---

Nuclear Structure Investigations of Light Nuclei  
with the R<sup>3</sup>B Experiment

---

Tobias Jenegger



Techinsche Universität München  
Fachbereich: Dense and Strange Hadronic Matter (E62)

2025



# Abstract

The nucleosynthesis of heavy elements ( $A > 56$ ) beyond iron, primarily via the rapid neutron-capture process (r-process), represents one of the most fascinating and complex phenomena in nuclear astrophysics. This process, which is responsible for the majority of heavy element production in the universe, provides a critical interface between astrophysics and nuclear physics, offering a unique "laboratory" to study nuclear reactions and properties far from stability. Neutron stars (NS), with their extreme densities and exotic compositions, are of exceptional interest in this context. These astrophysical objects serve as a natural laboratory to explore nuclear structure under extreme conditions, such as those described by the equation of state (EoS). Understanding the EoS, which governs the macroscopic properties of neutron stars, remains a formidable challenge. While astrophysical observations provide macroscopic constraints on NS models, nuclear experiments in terrestrial laboratories play a vital role in constraining the microscopic nuclear physics parameters embedded within these models. Moreover, neutron star mergers (NSMs), which are stellar collisions involving NSs, are recognized as the primary astrophysical sites for the r-process. These events generate conditions favorable for the production of neutron-rich nuclei, driving the synthesis of heavy elements. A comprehensive understanding of the r-process requires detailed knowledge of nuclear structure and reaction dynamics in regimes far from nuclear stability. However, experimental constraints on critical observables, such as fission yields and fission barriers, are limited due to the challenges associated with producing and studying these neutron-rich nuclei in laboratory settings. This doctoral thesis, titled "Nuclear Structure Investigations of Light Nuclei with the R<sup>3</sup>B Experiment", addresses these challenges by presenting the analysis of two key reaction channels using carbon isotopes. These investigations were conducted with the R<sup>3</sup>B (Reactions with Relativistic Radioactive Beams) setup during the commissioning experiment S444 as part of the FAIR Phase-0 campaign at GSI. Specifically, this work focuses on:

1. Charge-changing and total interaction cross sections: The study of  $^{12}\text{C} + ^{12}\text{C}$  collisions via the transmission method. These measurements provide critical insights into the nuclear structure and reaction mechanisms of light nuclei, which serve as essential benchmarks for understanding nuclear matter in astrophysical environments.
2. Quasi-Free Scattering (QFS) reactions: The investigation of the  $^{12}\text{C}(\text{p},2\text{p})^{11}\text{B}$  reaction as a tool to probe nuclear structure. This approach demonstrates its potential for studying the dynamics of the r-process through fission in QFS experiments, offering an innovative method to address experimental limitations in current r-process studies.

The results of these analyses contribute to our understanding of the structure of light nuclei and provide critical experimental constraints relevant to nuclear astrophysics. By advancing our knowledge of fundamental nuclear properties and reaction dynamics, this work bridges the gap between laboratory-based nuclear physics and astrophysical processes, shedding light on the origin of heavy elements in the universe.





# Contents

<b>1</b>	<b>Introduction</b>	<b>1</b>
1.1	Nuclear Structure Models . . . . .	2
1.2	R <sup>3</sup> B Experiment - "The Universe in the Lab" . . . . .	2
<b>2</b>	<b>Nuclear Scattering Reactions in the Glauber Framework</b>	<b>3</b>
2.1	Elastic scattering at low energies . . . . .	3
2.2	Nuclear Density distribution studies via elastic scattering . . . . .	4
2.3	Glauber Model for nuclear scattering at high energies . . . . .	4
2.3.1	Extensions to the Glauber model . . . . .	4
2.4	Cross sections for <sup>12</sup> C + <sup>12</sup> C . . . . .	5
2.5	Quasi-Free Scattering (QFS) Reactions . . . . .	5
2.5.1	Kinematics of QFS Reactions . . . . .	6
2.5.2	Cross Sections for QFS Reactions - Qualitative Considerations .	11
2.5.3	Application Fields of QFS Reactions . . . . .	11
<b>3</b>	<b>Experiment</b>	<b>17</b>
3.1	GSI facility . . . . .	17
3.1.1	FAIR Project . . . . .	18
3.2	R <sup>3</sup> B Setup . . . . .	19
3.3	Detector Setup in S444 Commissioning Experiment 2020 . . . . .	20
3.3.1	Multi Wire Proportional Chambers (MWPC) . . . . .	21
3.3.2	Ionisation Chambers - R <sup>3</sup> B Music/TWIM Music . . . . .	22
3.3.3	Sofia Start Detector . . . . .	25
3.3.4	GLAD Magnet . . . . .	25
3.3.5	CALIFA Calorimeter . . . . .	26
3.3.6	Sofia Time of Flight Wall . . . . .	33
3.3.7	NeuLAND Detector . . . . .	34
<b>4</b>	<b>Analysis - Total Interaction Cross Section of <sup>12</sup>C + <sup>12</sup>C</b>	<b>35</b>
4.1	Cross Section Measurement via Transmission Method . . . . .	35
4.2	Event Selection . . . . .	37
4.3	Charge Changing Cross Section Measurement . . . . .	42
4.3.1	TWIN MUSIC Calibration . . . . .	42
4.3.2	TWIN MUSIC Event Selection . . . . .	43
4.3.3	Carbon Identification . . . . .	44
4.4	Geometric Corrections . . . . .	52

4.5	Isotope Correction - Total Interaction Cross Section . . . . .	55
4.5.1	Results for Isotope Correction Methods . . . . .	62
4.6	Statistical and Systematic Error Analysis . . . . .	65
4.6.1	Statistical Uncertainties . . . . .	66
4.6.2	Systematic Uncertainties . . . . .	66
4.7	(Preliminary) Results Total Interaction Cross Section . . . . .	66
<b>5</b>	<b>Qualitative Analysis - Quasi-Free Scattering <math>^{12}\text{C}(\text{p},2\text{p})^{11}\text{B}</math></b>	<b>68</b>
5.1	Setup-Calibration . . . . .	68
5.1.1	Flight-Path Reconstruction . . . . .	68
5.1.2	Time of Flight Calibration . . . . .	71
5.2	Event Selection . . . . .	72
5.3	Fragment Identification . . . . .	73
5.4	QFS-Protons . . . . .	75
5.4.1	Missing Momentum $\mathbf{p}_{\text{miss}}$ Reconstruction . . . . .	80
5.4.2	Correlations between $^{11}\text{B}$ Fragment and the reconstructed inner Proton . . . . .	82
5.4.3	Proton Separation Energy $S_p$ . . . . .	83
5.5	Reconstruction of excited $^{11}\text{B}$ states . . . . .	86
5.6	Fission via Quasi-Free Scattering reaction . . . . .	86
<b>6</b>	<b>Machine Learning for the Cluster Reconstruction in the CALIFA Calorimeter at R<sup>3</sup>B</b>	<b>87</b>
6.1	Data Simulation and Selection . . . . .	87
6.2	Agglomerative Clustering Model . . . . .	87
6.3	"Edge Model" - Graphical NN . . . . .	87
6.3.1	Combination of both methods . . . . .	87
6.4	Results . . . . .	87
<b>Appendices</b>		<b>88</b>
<b>A</b>	<b>TWIN MUSIC Geometric Acceptance Correction via Efficiency Mea- surement</b>	<b>88</b>
<b>B</b>	<b>Flight-Path Reconstruction</b>	<b>89</b>
<b>References</b>		<b>93</b>

# 1 Introduction

The formation and evolution of astrophysical objects are intrinsically linked to the elemental abundances observed throughout the universe. Understanding the origin and distribution of these elements requires a robust theoretical framework grounded in nuclear structure models. The synthesis of elements – from the lightest nuclei formed during Big Bang nucleosynthesis to the heaviest transuranic elements produced in explosive astrophysical environments – depends critically on the properties of atomic nuclei.

The foundation for modern nuclear structure theory was laid by the atomic shell model, first introduced by Niels Bohr in 1913. This model, while initially developed for electrons in atoms, inspired the formulation of the nuclear shell model by Maria Goeppert Mayer and J. Hans D. Jensen in 1949. Their key innovation was the inclusion of a significant spin-orbit interaction term in the nuclear mean-field potential. Unlike the atomic case – where spin-orbit coupling appears as a relatively small fine-structure correction – in the nuclear shell model, the spin-orbit interaction is of comparable magnitude to the primary energy level gaps and carries an inverted sign. This results in the  $j = l + 1/2$  states lying energetically below the  $j = l - 1/2$  states.

This critical adjustment enabled the nuclear shell model to accurately reproduce the so-called "magic numbers" (2, 8, 20, 28, 50, 82, and 126), which correspond to closed shells of protons or neutrons associated with exceptional nuclear stability. Notable examples include isotopes such as those of tin ( $Z = 50$ ) and lead ( $Z = 82$ ), where large energy gaps between filled and unfilled shells lead to enhanced binding energies and structural rigidity.

While the shell model has proven highly successful in describing single-particle energy levels and making predictive statements for nuclei near closed shells, its applicability becomes limited when extended to large, deformed, neutron- or proton-rich exotic nuclei. In these regions, experimental data remain scarce, and the standard shell model must be extended or augmented to account for collective phenomena and configuration mixing. These nuclei play a central role in rapid neutron-capture processes (r-process), which are responsible for the formation of approximately half of the heavy elements beyond iron. In particular, the fate of the r-process path – its termination via fission and the possible emergence of a predicted "island of stability" in the superheavy region – depends critically on the structural properties of such exotic nuclei.

The first part of this chapter provides a concise overview of the historical and theoretical development of nuclear structure models. Emphasis is placed on the evolution of model concepts in response to the experimental and astrophysical challenges of their

time. The second part introduces the scientific objectives and research program of the R<sup>3</sup>B experiment. In particular, we highlight the role of nuclear structure studies in constraining the nuclear equation of state (EOS), especially for highly asymmetric nuclear matter. Nuclear scattering reactions at R<sup>3</sup>B offer an effective probe of these systems, and their theoretical treatment – along with a general overview of reaction mechanisms – will be presented in chapter 2.

## 1.1 Nuclear Structure Models

Influenced by the good results/predictions of the Fermi gas model -> same model applied to nucleons in nucleus -> talk about the key features and limitations of this model -> liquid drop model -> can well postulate the binding energy (model from experimental observations) From the success of the atomic shell model -> nuclear shell model -> describes well shell closures->magic numbers -> picture and description of shell model -> limitations -> maybe mention optical model -> as it is used to predict cross section in elastic scattering reactions -> mention that there are also other models as mean field, cluster models, ab initio models, collective models which exceed the topics of this thesis, but give some references to it.

## 1.2 R<sup>3</sup>B Experiment - "The Universe in the Lab"

Central formula is the equation of states (EOS). We want to study it within a wide range.

- in astrophysics NS are therefore of special interest. Measuring their mass and radius -> this relation depends on the EOS.
- since NS are highly asymmetric matter (neutrons only) they are a good playground to test the different models. Since they are all consistent at rho0 (real world) they diverge for higher matter asymmetry.
- plot of some models
- formula of Taylor expansion of Equation of state
- at FAIR we want to study nuclear matter under extreme conditions, highly asymmetric matter.
- constraining the symmetry energy
- this can be done via neutron removal cross section, cite T. Aumann, Bertulani etc.

- show picture of sensitiveness of this method, shortly mention that L was previously constrained in PREX experiments(give some literature for further readings)
- the predicted models rely on the input from reaction mechanisms ->  $^{12}\text{C}+^{12}\text{C}$  good to probe the underlying reaction mechanisms-> one part of the thesis

Moreover to study the single particle states of nucleons inside nucleus, especially when going toward exotic nuclei-> quasi free scattering experiments.-> refer to the theory of those scattering experiments This was the first time we had our CALIFA CALORIMETER in its final frame. Refer to the application section.

To point out is the pilot experiment we had in 2021 to study fission via qfs. This could have a large impact in the understanding of the dynamics of fission far off the line of stability.

Explain the fission via qfs a little bit more in detail here.

This could explain maybe better the element abundances we have and if there is any island of stability at  $Z > 126$ .

## 2 Nuclear Scattering Reactions in the Glauber Framework

Explain path to go:

- short intro why we use scattering reactions: to study structure of nuclei (mostly via e. scattering as they only interact via electromagn. force) and refer to chapter. Introduce problems qe account body problem etc
- starting from elastic scattering at low energies going to medium to high energies
- explain glauber: eikonal wave approximations, optical limit which leads to optical potential model, description via nucleon nucleon interaction

### 2.1 Elastic scattering at low energies

- Rutherford scattering,pionizing works (alpha particle on gold atoms),description in classical mechanics
- Rutherford scattering only valid if coulomb potential
- at low energies below pion production only elastic cross section
- introduce here the Scattering problem in quantum mechanics (see Schindler, p. 23)

- from classical physics we go to quantum mechanics and use partial wave decomposition with theta being the scattering angle
- include in this picture coulomb and nuclear interaction (as done in Kuk, page 120)

## 2.2 Nuclear Density distribution studies via elastic scattering

- Rutherford, Mott and Rosenbluth
- show something about form Factors
- are charge radii and nuclear radii measured?
- note approximation for  $^{12}C$  that neutron radius same as proton radius

## 2.3 Glauber Model for nuclear scattering at high energies

- explain model assumption
- eikonal wave approximation: high incoming momentum, low scattering angle
- Show picture of scattering
- optical limit: - Nucleons at high energy  $\rightarrow$  undeflected due to large momentum (linear trajectory) -Nucleus large compared to nucleon-nucleon force -Motion of nucleons independent of nucleus -overall cross-section described in terms of nucleon-nucleon cross section
- Description in the Probability Approach (also here I use all the eiconal and optical limit approximation)
- Description in the Eikonal optical-limit approximation
- Comparison of both descriptions methods for total interaction cross section, should end up with same. Advantage of PA is that you can calculate the cross section for a defined number of removed projectile nucleons (Schindler, p. 49)

### 2.3.1 Extensions to the Glauber model

- things which cannot be neglected and influence the cross section
- in medium modifications (see Lukas thesis)
- Coulomb interaction

- Pauli blocking

## 2.4 Cross sections for $^{12}C + ^{12}C$

- Total reaction cross section
- charge changing cross section; maybe I have to include lise++ calculations
- isotope corrections- neutron removal; maybe I have to include lise++ calculations

## 2.5 Quasi-Free Scattering (QFS) Reactions

Quasi-free scattering (QFS) reactions, as a subset of direct reactions, are processes where a projectile nucleon interacts with a target nucleon via the strong nuclear force in a single, fast, and highly localized event. The timescale of these interactions is extremely short, approximately  $10^{-21}$  s, implying that the relative kinetic energies of the participants are high, typically  $\gtrsim 100$  AMeV.

In QFS experiments conducted in direct kinematics, a proton serves as the projectile, colliding with a nucleon or a cluster within the target nucleus. Conversely, in inverse kinematics, the nucleus of interest becomes the projectile, while a proton or proton-like particle is used as the target. Despite these differing setups, both approaches are fundamentally equivalent, differing only due to a Lorentz transformation of the reference frame.

As the name implies, QFS reactions are conceptually similar to free nucleon-nucleon scattering, with the primary approximation being that the influence of the residual nucleus is neglected to first order. This approximation simplifies the theoretical description of the process, allowing to treat the interaction as a two-body problem within a (only weakly interfering) nuclear environment.

The first experiments confirming the existence of quasi-free scattering processes were conducted at the University of California, Berkeley, in 1952 by O. Chamberlain and Emilio Segrè[1]. In their study, lithium nuclei were bombarded with 350 MeV protons, and coincident proton pairs were observed with an opening angle of approximately  $90^\circ$ . That same year, J.B. Cladis, W.N. Hess, and B.J. Moyer published results on the scattering of 340 MeV protons on deuterium and carbon targets[2], further substantiating the phenomenon.

In 1957, Tyrén, Maris, and Hillman designed an experiment aimed at fully characterizing proton-proton collisions within the quasi-free scattering framework[3]. Their results validated the assumption of a direct and clean interaction between the projectile and the target nucleon, free from significant distortions caused by the surrounding

nucleus. Furthermore, these experiments demonstrated that QFS reactions could serve as a powerful tool for probing nuclear structure and testing predictions of the shell model. Specifically, they enabled the study of key nuclear parameters such as spin-orbit splitting and energy differences between nuclear shells and hence to probe the shell evolution.

In QFS reactions, these parameters can be extracted by analyzing the reaction products, which include the two correlated outgoing protons, the residual nucleus, and any gamma rays emitted during de-excitation of the residual nucleus. The detailed measurements of these observables provide critical insights into the underlying nuclear structure and dynamics.

The experimental discoveries and theoretical insights from these early studies catalyzed significant advancements in the theoretical modeling of QFS reactions. These models have since become essential tools for understanding nucleon-nucleon interactions within the nuclear medium and for refining our knowledge of nuclear structure and reaction mechanisms.

### 2.5.1 Kinematics of QFS Reactions

A simplified picture, which however explains the essential physics of the QFS reaction, can be found in figure 1: we have an incoming proton knocking out a nuclear constituent (proton/neutron) in a free nucleon-nucleon collision ending with a final state having the scattered proton, the scattered off nuclear constituent and the rest nucleus ( $A-1$ )<sup>1</sup>. In this picture index  $0$  is assigned to the incoming proton,  $1$  to the knocked out nucleon,  $2$  to the outgoing projectile proton,  $A$  to the initial nucleus and  $A-1$  to the final nucleus accordingly. From energy -momentum conservation the reaction can be expressed as:

$$P_A + P_0 = P_1 + P_2 + P_{A-1} \quad (1)$$

with  $P_i$  the four momentum ( $\mathbf{p}_i, E_i$ ).

In direct kinematics as presented in figure 1 the separation energy of the ejected nucleon for a certain final state of the nucleus  $A-1$  is given by<sup>1</sup>:

$$S = T_0 - (T_1 + T_2 + T_{A-1}); \text{ with } T_i \text{ the kinetic energy of particle } i \quad (2)$$

In the idealized shell model the separation energy equals to the (negative) energy of the nucleus' single-particle state. For the case the proton knocks out the least bound nucleon (proton/neutron) the final nucleus is lying in the ground state with  $E_{A-1} =$

---

<sup>1</sup>In inverse kinematics the four-momentum vectors need to be boosted to the center of mass frame of the initial nucleus via Lorentz transformation.

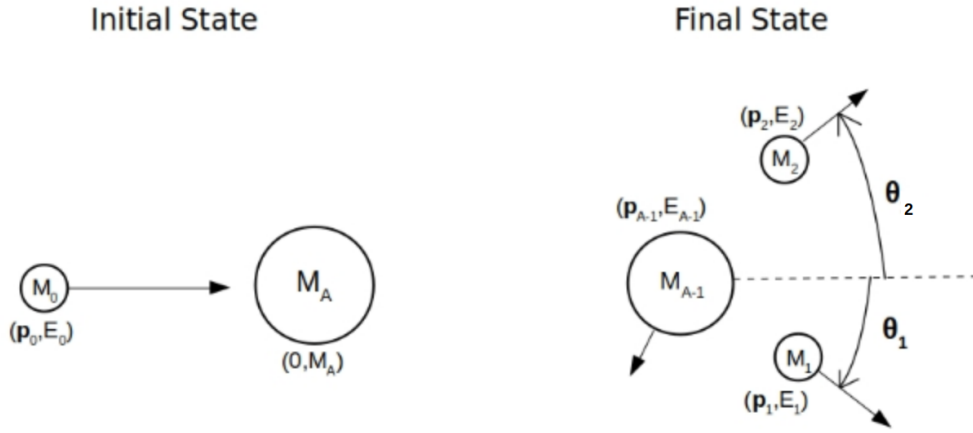


Figure 1: Simplified picture of the QFS reaction process in direkt kinematics.

$$M_{A-1}c^2 + T_{A-1}.$$

If a nucleon has been ejected from an inner shell resulting in a hole state, the final nucleus will be in an excited state:

$$E_{A-1}^* = M_{A-1}c^2 + T_{A-1} + E_{exe} \quad (3)$$

The excitation energy \$E\_{exe}\$ is reflected in the difference in the separation energy of the least bound nucleon and the ejected one. From the experimental point of view \$E\_{exe}\$ is directly accessible via gamma detection from the transition of the final nucleus from the excited to the ground state.

According to the picture of having a nucleon nucleon scattering process with no influence of the residual nucleus \$A-1\$ we can approximate the momenta of both constituents of the nucleus \$A\$ with \$\mathbf{p}\_A \approx \mathbf{p}\_i + \mathbf{p}\_{A-1}\$ where \$\mathbf{p}\_i\$ is the initial nucleon momentum inside the initial nucleus \$A\$. Since the initial nucleus is at rest (\$\mathbf{p}\_A = 0\$), the recoil momentum of the nucleus in final state \$\mathbf{p}\_{A-1}\$ equals to \$-\mathbf{p}\_i\$ the momentum of the initial nucleon pointing in opposite direction.

In addition the four-momentum of the inner nucleon can be deduced from momentum measurement of the initial and final state free nucleons:

$$P_i \approx P_{miss} \equiv P_1 + P_2 - P_0 \quad (4)$$

where \$P\_{miss}\$ is the so called "measured missing four-momentum of the reaction" [4]<sup>2</sup>. Thereupon, the separation energy measurement and the recoil momentum distribution

---

<sup>2</sup>\$P\_{miss}\$ is only equal to \$P\_i\$ for the unperturbed QFS (no ISI/FSI) case.

fully describe the single particle state in the various shell levels. In addition and as complementary method  $\gamma$  rays can be measured in coincidence with the reaction and consequently exclusive cross section and momentum distribution measurements of the single particle states are accessible as illustrated in figure blabla.

Considering the removal of a single nucleon from an initial nucleus with  $A$  nucleons and initial spin  $I$   $\Psi_i^A$  and final nucleus state  $\Psi_f^{A-1}$  with final spin  $I_f$  an overlap function between intial and final state many-body wave function can be written as:

$$\langle \vec{r}, \Psi_f^{A-1} | \Psi_i^A \rangle = \sum_j C_j^{if} \psi_j(\vec{r}), \quad \text{with } |I - I_f| < j < |I + I_f| \quad (5)$$

where  $S_j^{if} = |C_j^{if}|^2$  is the commonly named spectroscopic factor, see ref [5] sec.2.1.  $S_j^{if}$  is summed over all final single particle states  $m$  (from  $-j$  to  $j$ ). It is unity for nucleon removal from a pure single particle state and equals  $(2j+1)$  when the nucleon was removed from a filled  $j$ -subshell. The spectroscopic factor is linked to the exclusive experimental cross section measurement of a single particle state and the theoretical predicted one, as in ref [5]:

$$\sigma_{th}^{if} = \sum_j S_j^{if} \sigma_{sp}(nlj) \quad (6)$$

where  $\sigma_{sp}$  are the theoretical cross sections for the normalized wave functions  $\Psi_j$  of the final state nucleus A-1 with the appropriate quantum numbers.

From this considerations the spectroscopic factor can be used to probe the theoretical shell predictions. In past this was already done with direct QFS-reactions ( $e, e'p$ ). Results for the spectroscopic factor with data obtained at the NIKHEF facility is shown in figure 2. The substantial reduction of the spectroscopic factor with respect to the independent particle model (IPM) or mean field of  $\approx 35\%$  indicates a substantial depletion of the single-hole states and inferring from this a refined model prediction has to be applied<sup>3</sup>.

While QFS-reaction with electrons ( $e, e'p$ ) in direct kinematics is a valuable method to make precise measurements for stable (target) nuclei it is not suitable for the experimental analysis with exotic (neutron or proton rich) nuclei. Due to their instability they have a short lifetime (e.g.  $^{52}Ca$  with  $\tau = 4.6s$ ) they can hardly serve as targets. Inducing the reaction in inverse kinematics - having electrons as targets and the exotic nuclei of interest as projectiles - is also not feasible since no free electrons can be captured as target. The alternative approach is to use proton induced quasi-free scattering in inverse kinematics where the exotic beam impinges on an extended proton target such

---

<sup>3</sup>The mean field potential does not consider spin-spin interaction  $V_{ss}$ , non central tensor-potential  $V_T$  or spin-orbit interaction  $V_{LS}$ .

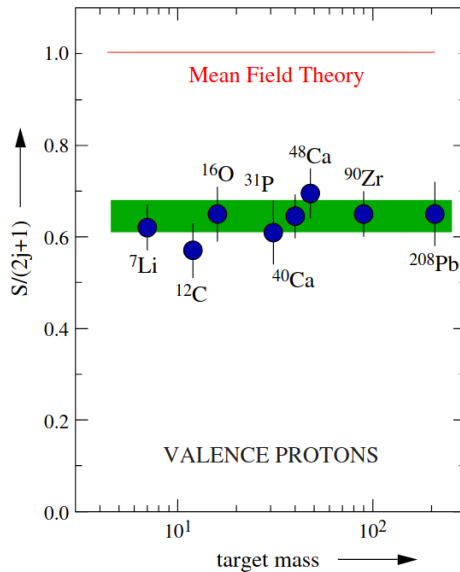


Figure 2: Normalized spectroscopic factors from the  $(e, e'p)$  reaction as a function of target mass taken from [6]. As input for the theoretical cross sections the prediction from mean field models were used.

as liquid hydrogen  $H_2$  or a fixed proton rich target such as  $CH_2$ <sup>4</sup>.

Summarizing, the QFS-reaction technique in inverse kinematics with exotic nuclei as in-flight projectiles and a proton-like target opens new possibilities to probe theoretical model predictions of deformed nuclei far off stability which haven't been accessible before.

For precise cross section measurements of the single particle states  $\sigma_{sp}$  the kinematical characteristics of the QFS-reaction products have to be considered for correct identification of QFS-events and clear background subtraction. The following descriptions are already implicitly embedded within the equation 1.

As starting point one compares the QFS-reaction of the two nucleons with the two dimensional non-central collision of free pointlike particles in nonrelativistic kinematics. Since both kinetic energy and momenta are conserved a clear signature is expected: the opening angle of the scattered particles is exactly  $90^\circ$ .

However, at kinetic energies of 400 AMeV and more, relativistic effects affects the opening angle of the scattered particles<sup>5</sup>. TODO: Formula to calculate directly from beam energy the opening angle...

For the final description of the process it has to be considered that the projectile

<sup>4</sup>Herefore a carbon target reference run is used to extract the QFS-reaction events from the  $CH_2$  target run.

<sup>5</sup>Relativistic considerations become relevant at velocities  $\beta \gtrsim 0.1c$ . This corresponds to  $\approx 4.5$  MeV.

nucleon inside the nucleus has a non negligible momentum (see  $P_i$  in equation 4) and in addition the separation energy  $S_{p/n}$  has to be expended to remove the scattered nucleon of the nuclear potential of the projectile nucleus.

To account for the nucleon momentum the picture of the fermi gas model where protons and neutrons freely move inside the nucleus' potential is applied. In the ground state of the nucleus the nucleons can reach a momentum up to the Fermi momentum  $p_F$ . Except for the light nuclei, the Fermi momentum is almost independent of A and amounts to  $\approx 250 \text{ MeV}/c$ <sup>6</sup>. The mean quadratic momenta of the nucleons is related to the Fermi momentum by:

$$\langle \mathbf{p}^2 \rangle = \frac{3}{5} p_F^2 \quad (7)$$

The width of the momentum distribution of the nucleons is given in the Goldhaber model by:

$$\sigma^2 = \sigma_0^2 K(A - K)/(A - 1), \text{ with } \sigma_0 \approx 90 \text{ MeV}/c \quad (8)$$

where A is the mass number of the projectile nucleus and K the mass number of the fragment after scattering. For a detailed derivation and further readings see ref. [7] and [8]. In the impulse approximation, where we assume that the interaction between the projectile and target nucleons has approximately the same form as the interaction between two nucleons in free space, the inner momenta of the scattered nucleons smear out the angular correlations of the outgoing fragment - which has the same momentum as the knocked out nucleon in the cms system of the nucleus but points in opposite direction - as well as of the two nucleons involved in the scattering. As consequence the opening angle distribution of the two scattered nucleons gets broadened as well as the azimuthal angular correlation which for the assumption of zero nucleon momentum sharply peaked at  $\Delta\varphi = 180^\circ$ .

In view of the added nucleon momentum the kinematics get expanded from a two dimensional scattering reaction to a three dimensional process where the reaction plane is determined by the plane spanned by the momentum vector of the projectile nucleus  $\mathbf{p}_A$  and the scattered nucleon after the reaction<sup>8</sup>. With the momentum measurement of the two correlated outgoing nucleons and the momentum of the incoming projectile nucleus it is possible to retrieve the internal momentum of the knocked out nucleon perpendicular to the reaction plane via the formula derived in reference[9]:

$$Q_{\perp i} = \sin(\theta_{1/2}) \cdot \sin(\varphi_{1/2} - \varphi_{2/1}) \cdot \mathbf{p}_{2/1} \quad (9)$$

---

<sup>6</sup>For light nuclei like  $^{12}\text{C}$ ,  $p_F \approx 230 \text{ MeV}/c$  can be assumed

<sup>7</sup>From the derivation of the mean kinetic energy of the nucleons  $\langle E_{\text{kin}} \rangle = \frac{\int_0^{p_F} E_{\text{kin}} p^2 dp}{\int_0^{p_F} p^2 dp} = \frac{3}{5} \cdot \frac{p_F^2}{2M}$

<sup>8</sup>For (p,2p) reactions there is an ambiguity which of the scattered protons  $\mathbf{p}_1$  or  $\mathbf{p}_2$  origin from the projectile nucleus or the proton like target.

In case of (p,2p) reactions it is impossible to track back the origin of each nucleon - from the projectile nucleus or the proton-like target. Iferring from this there are two possible solutions for  $Q_\perp$ . The ambiguity can be resolved by incorporating the momentum of the fragment nucleus perpendicular to the reaction plane  $Q_{\perp A-1}$ . The fragment momentum vector should be of the same amout but point in opposite direction to  $Q_{\perp i}$ . TODO: maybe insert here the plot of  $Q_\perp$  if possible...

Up to this point the scattering process was described similar to the free elastic scattering in relativistic kinematics with the projectile nucleon having a non negligible momentum. However the projectile nucleon is an off-shell particle bound inside the nucleus.

$$\mu_i = \sqrt{m_A^2 + m_{A-1}^2 + 2m_A\sqrt{m_{A-1}^2 + |\mathbf{p}_i|^2}} \quad (10)$$

in the c.m.s. of the projectile nucleus, with

$$0 < \mu_i < m_n \quad (11)$$

where  $m_n$  is the mass of the appropriate free nucleon. To knock the bound nucleon out of the nucleus the separation energy has to be overcome which can be observed in the reduced opening angle of the two outgoing correlated nucleons.

### 2.5.2 Cross Sections for QFS Reactions - Qualitative Considerations

TO DO: see more in the standard work [2], [3].

### 2.5.3 Application Fields of QFS Reactions

Over several decades of experimental and theoretical research, Quasi-Free Scattering (QFS) reactions have been firmly established as a powerful and direct tool for probing the microscopic structure of atomic nuclei. These reactions provide critical insights into nuclear correlations, single-particle properties, and the momentum distributions of nucleons within the nucleus.

The versatility of QFS extends across various applications, including the study of short-range nucleon-nucleon interactions, exotic nuclear states, and the modification of nucleon properties in nuclear matter. Advances in experimental facilities and state-of-the-art detector systems, have significantly improved the precision and scope of QFS measurements. These developments have enabled in-depth investigations of nuclear dynamics, the structure of unstable isotopes, and fundamental aspects of quantum many-body systems, contributing to a deeper understanding of nuclear and subnuclear phenomena.

This subsection will point out the most exciting and promising application fields of QFS

reactions with focus on the applicability in the R<sup>3</sup>B experimental setup. A detailed review can be found in ref [10].

**Single-Particle Spectroscopic Strength** As already mentioned in section 2.5.1 in many experiments a reduction in the spectroscopic strength of about 35% with respect to the independent particle model (IPM) and shell model predictions was observed. In one-nucleon removal reactions - experiments with isotope beams impinging on a composite nuclear target - the extraction of the missing spectroscopic strength is challenging as the kinematical pattern is highly complex. In contrast, the QFS reactions mechanism in inverse kinematics retains a clear kinematical signature which makes it a valuable tool to study the quenching of the spectroscopic factor which originates from residual correlations between bound nucleons inside the nucleus.

Several experiments were carried out at the GSI Facility to study the reduction factor of the spectroscopic strength and its evolution over a broad range in isotopic chains, such as for oxygen shown in figure 3. With the commissioning of the SIS100 and SuperFRS at GSI it will be achievable to study (p,2p) reactions with very short lived nuclei at reasonable intensities which will presumably draw even more attention to QFS reaction approach.

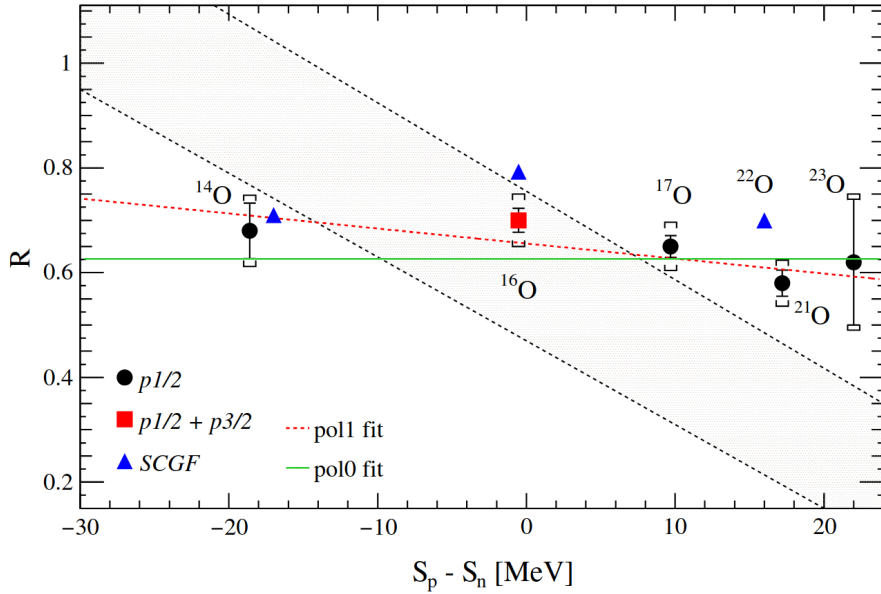


Figure 3: Extracted reduction factors of the spectroscopic strength from (p,2p) measurements (circles and square) as a function of the difference between proton and neutron separation energy  $S_p - S_n$ . The blue triangles correspond to the predictions from self-consistent green functions (SCGF). The shaded area indicates the trend from an analysis of one-nucleon removal cross sections. From Ref. [11].

**Gamma Spectroscopy** Alongside to the study of the single-particle spectroscopic strengths QFS reactions provide valuable information of the shell structure and deformation of the fragment ( $A=1$ ) via gamma spectroscopy. While quasi-free scattering with nucleons in the outermost shell yield a fragment in the ground state, the scattering with nucleons in inner shells result in bound (or unbound) excited states of the ( $A=1$ ) fragment. This excited fragment instantaneously transits to the ground state by the emission of a Doppler shifted  $\gamma$  ray.

A big advantage of the ( $p,p_2p$ ) reaction experiments is ability to make precise vertex reconstruction by accurate measurement of the two outgoing correlated protons. This is of particular importance for extended targets and determines the emission point within the target, enabling an accurate calculation of the fragment's velocity and therefore a precise Doppler correction.

From gamma spectroscopy the excitation energy  $E(2+)$ , often the first excited state in even-even nuclei, can be observed which is a fundamental observable of nuclear structure, providing key insights into the shell configuration and deformation of the nucleus[10]. Especially when going towards exotic neutron rich isotopes the study of the gamma emission lines can strongly contribute to the understanding of nuclear shell evolution.

**QFS to probe inner clustering and halo formation** Clusterization inside nuclei is a phenomenon widely observed in experimental astrophysics with large implications on processes such as the synthesis of carbon inside stars via triple  $\alpha$  clusterization [12],  $\alpha$ -radioactivity, or the evolution of core collapse supernovae[13], just to mention some. Its presence has also to be implemented in the state of the art equation of state calculations.

Single-particle cluster states can be directly accessed via QFS ( $p,p\alpha$ ) reactions. In the low energy regime of 100 AMeV the  $^{12}\text{C}(p,p\alpha)^8\text{Be}$  reaction, see ref [14], as benchmark study approved the reaction mechanism and up to a scaling factor the measured cross sections aligned exceptionally well to the free  $p-\alpha$  scattering measurements.

Moreover the QFS mechanism allows to access light nuclei going towards the neutron drip line via ( $p,pn$ ) reaction. These light nuclei are mostly weakly bound with an extended low density neutron-matter distribution forming a so-called *nuclear-halo*.

The most prominent candidate for such is  $^{11}\text{Li}$ , often called *Borromean three-body system*[15], consisting of two neutrons interacting with a core ( $^9\text{Li}$ ) via weak, short-range interactions. First evidence for the correlation between the two neutron was strongly pushed by experimental studies at GSI, see [16], and theoretical

work by Bertulani et. al.[17].

The latest experiment with the focus on the study of multi-neutron correlations in drip-line nuclei was carried out at R<sup>3</sup>B in 2022 (experiment S509) probing broad isotopic chains of Li, Be, B, C and N via the QFS mechanism.

**Short Range Correlations(SRC)** Short range correlations refer to elementary nucleon-nucleon interactions within a nucleus and occur over very short distances, typically on the order of 1-2 femtometers. These correlations are characterized by pairs of nucleons with high relative momentum ( $> k_F$ , Fermi momentum) and low total momentum. These NN-interactions are treated as good explanatory candidate for observed deviations from mean field approximation. Many phenomena, such as the above discussed reduction in the spectroscopic strength and the EMC effect[18], the observation that the cross section for deep inelastic scattering from an atomic nucleus is different from that of the same number of free protons and neutrons, are associated to the short range correlations inside the nucleus.

From isotopic chain studies[19] it has been shown that there is an indication of SRC dependency on isospin, see figure 4, where SRC are predominantly preferred by p-n pairs than by nn or pp pairs. This again can have significant impact for asymmetric nuclei and imply a stronger quenching of the spectroscopic strength for proton single particle states below the Fermi momentum for neutron rich matter.

Since pioneering experiments were made at JLab and Brookhaven via ( $e, e'p$ ) and ( $e, e'n$ ) reactions several experimental campaigns were carried out at GSI with the R<sup>3</sup>B setup probing the QFS reactions via the strong nuclear force instead of the Coulomb interaction. In 2022 the S509 experiment was performed to exploit for the first time the use of short-lived nuclei scattering off a proton probe in inverse kinematics at R<sup>3</sup>B, followed by the S091 experiment in 2024 with the focus on probing NN-correlations in atomic nuclei via ( $p, pd$ ) QFS reactions[20].

**Fission via QFS** Fission induced via quasifree scattering (QFS) provides a powerful method to extract fission barriers on an event-by-event basis. The fundamental concept involves the knockout of a proton or neutron from an incoming exotic ion beam. By measuring the energy and the angular distribution of the correlated emitted nucleons, it becomes possible to probe the excitation state of the daughter nucleus. In cases where deeply bound nucleons are knocked out, the resulting daughter nucleus either evaporates one or multiple neutrons or populates an excited state, which can be experimentally observed. The R<sup>3</sup>B setup is particularly well-suited for such investigations, as it enables full kinematic reconstruction of the reaction products and hence to pin down the complete reaction mechanism.

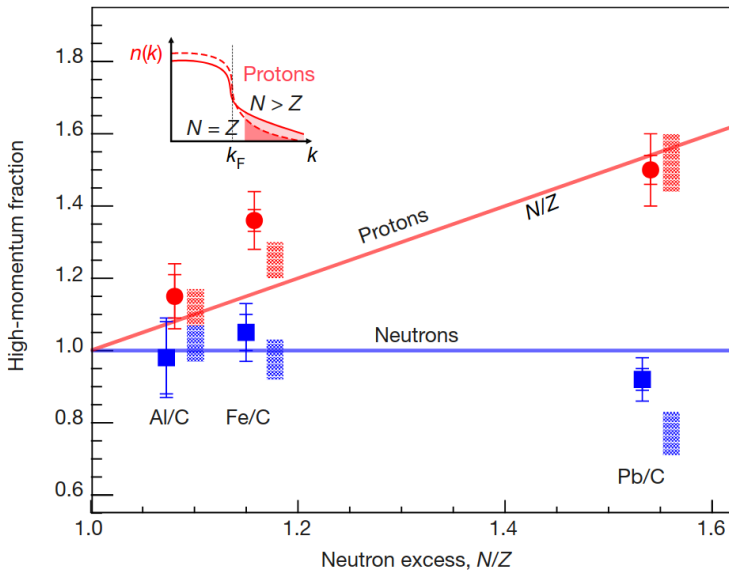


Figure 4: Fraction of high-momentum neutrons and protons with respect to the  $N/Z$  ratio for several carbon isotopes. A clear trend towards high momentum proton distribution for neutron rich carbon isotopes (red line) is shown, while the high momentum neutron distribution stays constant with respect to the  $N/Z$  ratio (blue line). From reference [19].

This approach allows for the detailed exploration of the potential-energy surface and the fission dynamics across a broad range of fissility and excitation energies, taking advantage of relativistic radioactive beams.

A pilot experiment was conducted in 2021 at R<sup>3</sup>B using a stable <sup>238</sup>U beam incident on a liquid hydrogen target. The data collected from this experiment provide simultaneous information on several key fission observables, which can be used to constrain theoretical calculations. These calculations aim to describe both the static and dynamic properties of the fission process and enable comparisons with predictions from various theoretical frameworks, including phenomenological approaches, macroscopic-microscopic models, and fully microscopic statistical or time-dependent Hartree-Fock calculations.

A critical aspect of this experimental setup is the simultaneous measurement of the two outgoing fission fragments. This is achieved using a dedicated ionization chamber (TWIM-MUSIC) and advanced tracking detectors. The success of this methodology has already been demonstrated by promising results, see [21],[22] and figure 5, highlighting the potential of this technique in advancing our understanding of nuclear fission dynamics.

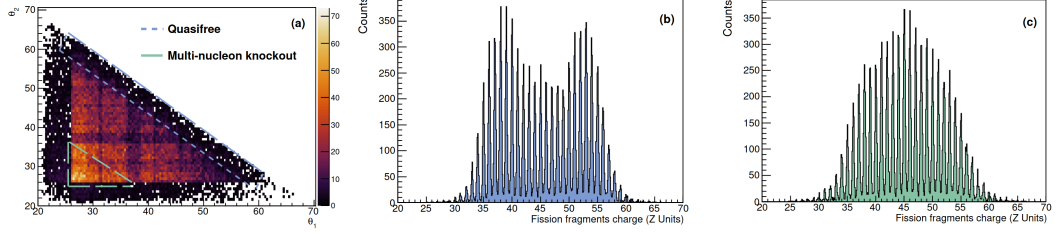


Figure 5: (a) Polar angle correlations of the two protons from fission via QFS event. In (b) the charge distribution for quasi-free ( $p,2p$ ) fission reactions is selected while (c) displays the charge distribution for multi-nucleon knockout reactions of FSI. From Ref [21], S455 Experiment in 2021 at  $R^3B$ , GSI.

### 3 Experiment

The here presented commissioning experiment was performed in 2020 at the FAIR Facility at GSI (Gesellschaft für Schwerionenforschung) in Darmstadt (Germany). The GSI operates a unique accelerator facility for heavy ions and focuses on several cutting-edge research fields. These include:

1. **Nuclear Physics:** Studying the properties of atomic nuclei, exploring the forces that bind protons and neutrons, and investigating exotic nuclei far from stability, see e.g. HISPEC/DESPEC experiment [23].
2. **Hadron and Quark Matter:** Investigating the behavior of hadrons (particles made of quarks) and the state of matter under extreme conditions, such as those found in neutron stars or during the early universe, see e.g. HADES experiment [24].
3. **Atomic Physics:** Examining the structure and dynamics of atoms, including highly charged ions, to understand fundamental atomic interactions and refine quantum electrodynamics, see e.g. [25].
4. **Plasma Physics:** Creating and analyzing high-energy-density plasmas to simulate conditions found in stellar interiors and other astrophysical phenomena, see e.g. PHELIX laser facility [26].
5. **Biophysics and Medical Research:** Exploring the effects of ion beams on biological systems for applications in cancer therapy, particularly using heavy ion therapy, and studying radiation protection for space missions.
6. **Materials Research:** Investigating the response of materials to high radiation doses to develop more resilient materials for use in various technologies, including nuclear reactors and space exploration.

#### 3.1 GSI facility

The GSI Helmholtzzentrum für Schwerionenforschung GmbH was founded in 1969 (as "Gesellschaft für Schwerionenforschung mbH) looks back on a successful research history. In the time between 1981 and 2010 six new superheavy elements were discovered<sup>9</sup>. In the medical research field GSI has developed advanced cancer therapy techniques

---

<sup>9</sup>A comprehensive overview work of five decades of GSI superheavy element discoveries can be found here [27]

using heavy ion beams which target tumors with high precision, minimizing damage to surrounding healthy tissues.

Along with those groundbreaking discoveries in research the facility at GSI has always been an inspiring source of drive for new technologies.

The key devices and apparatus enabling heavy-ion experiments at GSI, which operates one of the most advanced accelerator facilities in the world, include:

The starting point for the production of relativistic heavy ions at GSI is the ion source where ions are generated by stripping electrons off the shell of the atoms. Depending on the experimental needs the ion sources at GSI are able to produce ions of many different kinds of elements (up to Uranium)[28].

On the first acceleration stage the stable primary ions are injected from the ion source into the UNIversal Linear Accelerator (UNILAC). On a length of 120 meters ions are accelerated up to maximum energy of 11.4 AMeV. The low energy beam is now injected into the ring accelerator SIS18 (Schwerionensynchotron 18). Here the ion beam is further accelerated up to 4.7 GeV/u (for protons) / 1 GeV/u (for Uranium). The magnets and the ultra-high vacuum ( $\sim 10^{-9}$  Pa) keep the ions well on their circular path (SIS18 has a circumference of 216 meters)[29]. For the production of rare heavy isotopes the primary ion beam from SIS18 can be impinged on a light nuclear target, e.g beryllium, the so called production target. These secondary beams of radioactive isotopes can be either stored in the experimental storage ring (ESR) for later use or transferred to the FFragment Separator (FRS). The FRS as a high-resolution magnetic spectrometer is capable to precisely select specific isotopes and to forward the desired beam of exotic relativistic nuclei to the various experiments or direct it to the ESR for later use.

### 3.1.1 FAIR Project

The Facility for Antiproton and Ion Research (FAIR), located adjacent to GSI, will be one of the most advanced and extensive accelerator complexes in the world. The construction of the superconducting ring accelerator SIS100, with a circumference of 1.1 km, along with associated storage rings and experimental sites, began in the summer of 2017. The commissioning of parts of the facility is planned for 2027, followed immediately by the Early Science Program.

The so-called First Science Phase, which will mark the full operation of SIS100 and the complete commissioning of FAIR equipment, will be the next step. Prior to the commissioning of SIS100, several high-priority experiments with significant scientific impact will take place as part of the Early Science Program in the newly established experimental halls. These include experiments utilizing the R<sup>3</sup>B setup in the High-

Energy Cave (HEC), focusing on key aspects of nuclear structure and reactions under extreme conditions.

### 3.2 $R^3B$ Setup

The  $R^3B$  (Reactions with Relativistic Radioactive Beams) experiment in Cave C at the GSI in Germany is a cutting-edge research experiment focused on the study of nuclear reactions and structure using high-energy radioactive ion beams. The experiment aims to investigate exotic nuclei far from stability, offering insights into the fundamental properties of nuclear matter, nucleosynthesis processes, and the forces governing nuclear interactions. A schematic overview of the  $R^3B$  setup can be seen in Figure 6.

The short living (neutron rich) isotopes are injected to the Cave C from the FRS, which

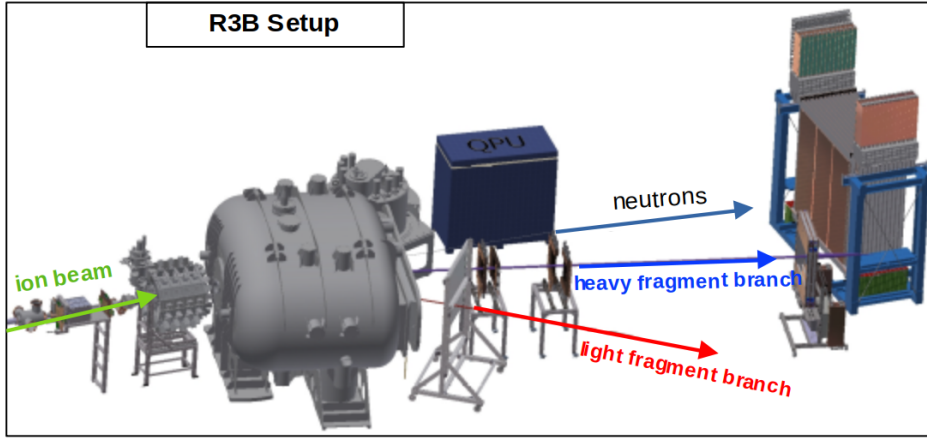


Figure 6: Overview of the  $R^3B$  setup in Cave C with detectors for the specific fragment branch identification.

preselects as mass spectrometer the isotopes of interest, and impinge on a fixed target. The  $R^3B$  setup is designed for kinematically complete reaction studies. To fulfill this requirement the incoming ions are tracked and identified on an event-by-event basis by dedicated detectors in the FRS via time-of-flight and  $\Delta E$  measurement techniques [30]. Depending on the settings and composition of the incoming ion beam different type of reactions take place in the target area with a large variety of reaction products: heavy ions (as products from fission/spallation reactions), neutrons, light charged particles and gamma rays. For the detection of gammas and light charged ions from reactions with the target the dedicated CALIFA calorimeter (see more in section 3.3.5) and various tracking detectors are installed in the target region. The GLAD (GSI Large Acceptance Dipole) magnet, located at the center of the Cave C, allows fragment identification for the forward boosted charged reaction residues. The magnetic rigidity of the charged reaction residues is measured by a combination tracking detectors and a time of flight

wall after the GLAD magnet. This allows to identify the charged reaction residues and their momenta. For the detection of the neutrons, not deflected by the magnetic field of the GLAD magnet, the new array neutron detector (NeuLAND) is positioned after GLAD on the zero degree line with the incoming ion beam.

The R<sup>3</sup>B setup offers high flexibility, allowing operation both in vacuum and in atmospheric conditions. Over the past few years, during the so-called *Phase-0*, numerous experiments have been conducted, each utilizing different configurations and newly developed or upgraded detector systems.

The combination of a broad spectrum of incoming ion beams across a wide energy range, provided by the FRS facility, and the versatility of the R<sup>3</sup>B setup – equipped with state-of-the-art detectors tailored for specific physics studies – makes it an exceptional platform for experimental astrophysics.

### 3.3 Detector Setup in S444 Commissioning Experiment 2020

The S444 Experiment (successor experiment of the FAIR Phase-0 program in 2019, see ref. [31]) for the commissioning of the CALIFA Calorimeter in its final mechanical design took place in February 2020. The choice to operate with stable <sup>12</sup>C primary beam with four beam energy settings - 400/550/650/800 AMeV gave the opportunity to use it as preparation for the following up S467 experimental run with neutron-rich *Ca* isotopes as medium-heavy incoming beam. The detectors for positional tracking, charge identification and time measurement were provided by the SOFIA(Study on Fission with ALADiN<sup>10</sup>) collaboration. These detectors are optimized for fission experiments with medium to heavy reaction fragments. As for the S444 experiment with primary <sup>12</sup>C incoming beam no fission reaction with multiple heavy charged fragments is expected the Sofia detectors were adapted accordingly (e.g. only one of the four sections of the Twin-Music Ionisation chamber was operated, see more in section 3.3.2).

For this commissioning experiment, most detectors and components of the setup were operated in air. The target chamber, as well as the GLAD magnet, was filled with gaseous helium at room temperature to reduce unwanted interactions.

However, the presence of air in the setup leads to ion interactions with atmospheric particles, causing angular straggling in the flight path reconstruction. This effect can limit the resolution of the reconstructed momenta from reactions occurring at the target.

---

<sup>10</sup>ALADiN magnet was the predecessor of GLAD.

### 3.3.1 Multi Wire Proportional Chambers (MWPC)

The positional tracking of the incoming ions as well as the charged reaction products were performed by using Multi Wire Proportional Chambers (MWPC). A MWPC operates on the principle of proportional counters that are arranged side by side in a plane, thereby providing spatial resolution for particle radiation. The multi wire proportional chambers were developed in late 1960s by George Charpak<sup>11</sup> at CERN[32].

The MWPC operates in the same way as aligned proportional counters with the difference of not having dividing walls between the anode wires. This reduces the material budget, hence improving the spatial resolution and reducing reactions with the detected particle.

In the general design the MWCP is made up of a plane of anode wires enclosed between two cathode planes which are aligned parallel or vertical to the anode wires. Depending on the beam conditions the anode wires are set to high voltage ( $\sim 1100$  V) while the cathode planes are grounded.

The volume between the two cathode planes is filled by a gas mixture of 84% Argon and 16% CO<sub>2</sub>. The decision of the gas mixture is driven by a balanced ratio between amplification and quenching properties of the gas.

When a charged particle passes through the detector it ionizes the gas. Primary electrons are created followed by a secondary ionization via electron avalanche. The electron avalanche drifts towards the wires (anodes) while the positive ions drift towards the grounded cathode planes. As the MWPCs are operated in the proportional region, the number of created electrons/ions is proportional to the initial ionization. Instead of reading out the signal from the wires it is read out from the strips of the cathode plane, see figure 7. This improves the position resolution in case the cathode planes are aligned perpendicular to the wires. In case multiple (neighboring) strips give signal the signal distribution over the strips is analyzed and fitted to provide the position information.

In the R<sup>3</sup>B setup for the S444 experiment four MWPCs were installed:

1. MWPC0: right at the beginning of the beam entrance in Cave C, 184 cm upstream to the target position to detect x- and y positions of the incoming ions.
2. MWPC1: 88 cm downstream to the target for positional tracking in x and y of the outgoing reaction fragment

---

<sup>11</sup>George Charpak received the Nobel Prize in Physics in 1992 for his invention and development of particle detectors, in particular, the multiwire proportional chambers.

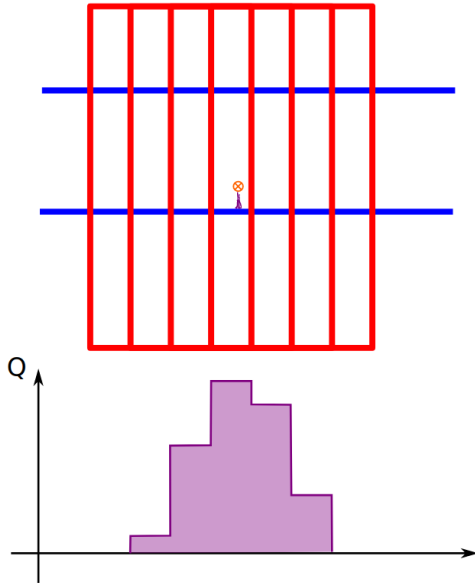


Figure 7: Schematic representation of the charge distribution when reading out the signal from the cathode pads (red) instead of the anode wires (blue). The red cross symbolizes the incident ion.

3. MWPC2: 154 cm downstrem also for positional tracking of the fragment
4. MWPC3: after the GLAD magnet. The x position of this detector gives the information about the magnetic rigidity of the reaction fragment.

Despite having the same mode of operation, they slightly differ in their construction design and positional resolution. For the technical specifications of the individual MW-PCs, see table 1.

### 3.3.2 Ionisation Chambers - R<sup>3</sup>B Music/TWIM Music

For the S444 experiment at R<sup>3</sup>B two types of **M**ulti **S**ampling **I**onisation **C**hambers (MUSICs) were installed: the R<sup>3</sup>B MUSIC, centered 153 cm upstream to the target, and the TWIN-MUSIC, 132 cm downstream to the target. Like the MWPCs (see 3.3.1) the ionisation chambers are gas-filled detectors for tracking down charged particles. While MWPCs consist only of a few mm of active gaseous volume, the ionsiation chambers have an expanded gaseous volume which allows to make precise energy loss measurements from the ionisation process of the gas. The multi sampling ionsiation chambers consist of a cathode plane and an anode plane, consisting of multiple anode strips. When a charged particle crosses the chamber the gas gets ionized and the created electrons and ions are separated by the strong electric field. While the ions drift towards the cathode plane the electrons move to the anodes where each anode is read out separately.

Common MWPC Settings	
Gas	84% Ar, 16% CO <sub>2</sub>
Windows	Mylar®
Anode wires voltage	1100 V
Cathode planes voltage	Ground
Wire pitch	2.5 mm
Wire diameter	5 μm
Width of X pads	3.125 mm

MWPC0	
X pads	64 pads, vertically segmented into two equal parts
Y pads	64 pads, horizontally segmented (3.125 mm width)
Active surface	200 × 200 mm <sup>2</sup>

MWPC1 & MWPC2	
X pads	64 pads, vertically segmented into two equal parts
Y pads	40 pads (5 mm width), horizontally segmented
Active surface	200 × 200 mm <sup>2</sup>

MWPC3	
X pads	288 pads
Y pads	120 pads (5 mm width)
Active surface	900 × 600 mm <sup>2</sup>

Table 1: SOFIA MWPCs - Technical specifications

Since the energy loss of the passing through particle is proportional to the square of its charge ( $\Delta E \sim Z^2$ ) the signal from the anodes allow to precisely measure the charge of the particle. Moreover multi-sampling ionisation chambers measure the drift time of the electrons created by the ionisation process on each anode (compared to one or more reference anodes). Assuming a constant electron drift velocity ( $\sim 40\text{mm}/\mu\text{s}$ ) over the gaseous volume the time information of each anode signal can be used to reconstruct the x-position of the passing through particle.

### R<sup>3</sup>B MUSIC

The R<sup>3</sup>B MUSIC, installed 153 cm upstream to the target, is used to measure both the charge of the incoming ion before impinging on the target and the angle of the particle's trajectory. The detector has an active gaseous dimension of 20 x 20 x 40 cm<sup>3</sup>, confined on one side by a cathode plane and on the other side by an anode plane

consisting of 10 anodes ( 8 readout anodes and 2 screen anodes). For the technical specifications, see table 2.

<b>Dimensions</b>	
Detector dimension:	51 x 54 x 53 cm <sup>3</sup>
Active dimension:	20 x 20 x 40 cm <sup>3</sup>
Dimension of one anode:	20 x 20 x 5 cm <sup>3</sup>
Dimension of one screen anode:	20 x 20 x 2 cm <sup>3</sup>
<b>Gas</b>	
P75 (Ar 25%, CH <sub>4</sub> 75%)	
<b>Voltage</b>	
Cathode (left to beam direction):	-(2 – 6)kV
Anode (right to beam direction):	+300V

Table 2: R<sup>3</sup>B MUSIC - Technical specifications

## TWIN MUSIC

The TWIN MUSIC is a double ionisation chamber with one central cathode plane and two independent drift volumes and anode planes on each side. Each of the anode planes consists of 16 anodes for readout plus two screen anodes. Furthermore each anode is again segmented into up/down which splits the detector into four dedicated sections. As the TWIN MUSIC is placed 132 cm downstream to the target it is employed to measure charge and angular direction of the outgoing medium-to-heavy fragments. The detector was designed for the requirements in fission experiments where two or more fission fragments are created. If each fragment is flying through one of the four sections ( which is mostly the case due to momentum conservation rules) charge and angle of each fragment can be measured independently.

To fulfill the required permanence of the field in both extended gaseous volumes (of dimension 11x22x40 cm<sup>3</sup>) a Frisch grid is located 3 mm from the anode planes. The Frisch grid is metal mesh grid that shields the anode from the movement of ions produced during ionization process in the chamber ensuring that only the electrons that reach the anode contribute to the signal. Additionally, the shielding of the anodes by the Frisch grid account for the fast rise time of the signal at the anodes which diminishes pile-up effects and makes the detector high beam-rate capable (up to 100kHz). Further technical specifications you can find in table 3.

---

**Dimensions**

Detector dimension:	43 x48 x55 cm <sup>3</sup>
Active dimension:	two halves each 11x22x40 cm <sup>3</sup>
Distance central cathode - Frish grid:	11 cm
Distance Frish grid from anode planes:	3mm

**Gas**

CH4 [79%], Ar [20%] and CO2 [1%]

**Voltage**

Central cathode:	-(2 – 6)kV
Anode planes:	+600V
Frish Grid:	+250V

**Resoultions**

$\Delta E/E$	< 5% FWHM, total < 2% FWHM
$\Delta X$	< 40 $\mu$ m

---

Table 3: TWIN MUSIC - Technical specifications, see also [33]

### 3.3.3 Sofia Start Detector

The SOFIA Start detector is positioned right after the R<sup>3</sup>B MUSIC ionisation chamber and gives a time reference for the incoming ion. It is a 1 mm thin scintillating plastic blade attached with a photo multiplier tube on each side. The scintillator light from excitation of the incoming ions produce a clear CFD signal on both photomultiplier tubes used for the time measurement:

$$t_{start} = 0.5 \cdot (t_{left} + t_{right})$$

To shield the plastic detector from daylight it is wrapped in mylar foil (300 $\mu$ m thickness).

### 3.3.4 GLAD Magnet

The **GSI Large Acceptance zero degree superconducting Dipole magnet GLAD** sits in the center of the R<sup>3</sup>B setup in the Cave C, see figure 8. With an adjustable field integral up to 5 Tm it has a high acceptance range in magnetic rigidity which is crucial for the identification of highly asymmetric reaction fragments. The homogeneous magnetic field in GLAD allows to achieve momentum resolutions  $\Delta p/p$  of 10<sup>-3</sup> in combination with the dedicated tracking system.

The large opening angle of  $\pm 80$  mrad makes the GLAD magnet highly transmissive for

evaporated or scattered neutrons in the reaction process which will be subsequently detected in the NeuLAND detector.

The default bending angle of the beam with respect to the beam line was set to  $18^\circ$ . Herefore the currents where adjusted according to the beam energy:

1. 400 AMeV beam: 1444 Ampere
2. 550 AMeV beam: 1778 Ampere
3. 650 AMeV beam: 1957 Ampere
4. 800 AMeV beam: 2223 Ampere

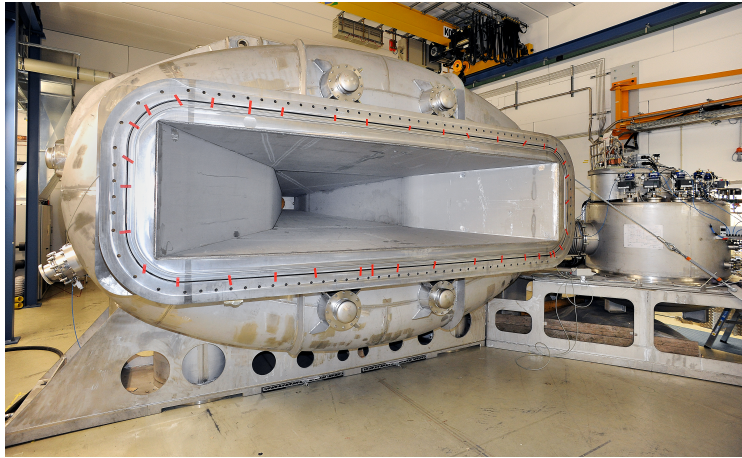


Figure 8: Upstream view of GLAD magnet in the center of Cave C after installation in February 2016. Picture from [34]

### 3.3.5 CALIFA Calorimeter

The **CAL**orimeter for **I**n **Flight detection of  $\gamma$ -rays and high energy charged p*A*rticles, CALIFA, is one of the main detector components of the R<sup>3</sup>B setup. It surrounds the target area and covers the full azimuthal range and a polar angular acceptance from  $7^\circ$  up to  $140^\circ$  in the target region. The calorimeter serves for the detection of gamma rays in the energy region  $100 \text{ keV} \lesssim E_\gamma \lesssim 30 \text{ MeV}$  and light charged particles, mostly protons, up to  $E_p \lesssim 700 \text{ MeV}$ . To fulfill the demands requested by the different experimental campaigns an energy resolution of  $\frac{\Delta E}{E}(@1\text{MeV}) \sim 6\%$  in the gamma-ray energy regime  $\frac{\Delta E}{E}(@100\text{MeV}) \sim 1\%$  in the proton range regime is required.**

#### Geometry

The CALIFA detector is a highly segmented detector with 2544 CsI(Tl) crystals installed in the final design. Since experiments in the R<sup>3</sup>B setup operate in relativistic

kinematics both the incoming ions as well as the measured particles originating from reactions within the source experience relativistic effects, more precisely the so called relativistic Doppler effect. The emitted gamma rays and protons are not isotropically distributed around the source region but are instead boosted in the forward direction. Furthermore, the energy measured in the laboratory frame differs from the kinetic energy in the rest frame of the incoming ion due to relativistic effects.

The relativistic Doppler effect has a huge impact on the geometric design and requirements of CALIFA. Herefore the detector was subdivided into three polar angle ranges<sup>9</sup>:

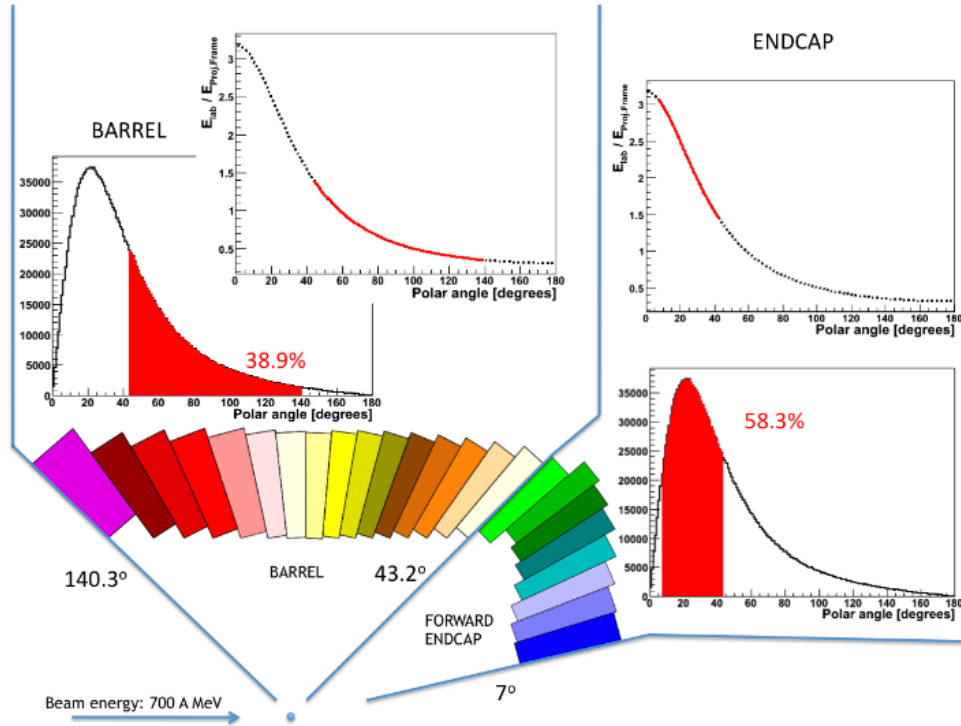


Figure 9: Schematic view of the Barrel and Endcap(iPhos and CEPA) segments of CALIFA and the according angular and energy distribution of emitted  $\gamma$  rays (monoenergetic in the projectile frame at beam energy of 700 AMeV). From [35]

- $7^\circ \leq \theta \leq 19^\circ$  - CEPA (CALIFA Endcap Phoswich Array): The most forward segment consists of 112 CsI(Tl) crystals. Due to the aforementioned relativistic Doppler effect this area will have the highest intensities and energies. For high beam energies most of the particles will not be stopped inside the crystal and will escape as "punch-throughs". Despite the "punch-through" ions deposit only a fraction of their kinetic energy ( $\Delta E$ ) in CALIFA it is possible to reconstruct the initial energy of the particle<sup>12</sup>. In CEPA crystals with a length of 15 cm are

<sup>12</sup>This is done by exploiting the distinct scintillation components of CsI, see more in chapter 5 of

used and cover each a polar angle of  $\approx 2^\circ$ . The finer segmentation in the polar angular range provides the advantage of compensating for high event rates while enabling high-resolution Doppler correction.

- $19^\circ \leq \theta \leq 43^\circ$  - Intrinsic Phoswich (iPhos): In conjunction with the CEPA, the iPhos region forms the hindmost part of the CALIFA Endcap. The iPhos region is, same as for the CEPA, affected by high rates. Protons reaching this region have high kinetic energies ( $E_{kin,p} \leq 600\text{MeV}$ ) and therefore a large fraction of "punch-throughs" are expected. In the iPhos region 480 CsI(Tl) crystals with a length of 22 cm<sup>13</sup> are installed and cover each a polar angle of  $\approx 3^\circ$ .(For more information see Endcap TDR:[37]).
- $43^\circ \leq \theta \leq 140^\circ$  - Barrel: This segment covers the region where the lowest rates and energies are expected. The Barrel region contains 1952 CsI(Tl) crystals. The most forward crystals have a length of 22 cm (which allow to stop protons with  $E_{kin,p} \leq 315\text{MeV}$ ). This length is reduced down to 12 cm for the most backward crystals (For more information see Barrel TDR:[35]).

The crystals are arranged in carbon fibre alveoli with a nominal wall thickness of 230  $\mu\text{m}$ [35] that provide a support structure for the crystals and keep the material bunched as low as possible. The alveoli in turn are held and covered by individual aluminium tiles. The volume enclosed by the alveoli and the aluminium tiles is flooded with nitrogen to keep humidity low on the surface of the crystals. For a sufficient suspension of the aluminium cover a robust external holding structure was designed, see figure 10.

In 2019 CALIFA was for the first time integrated into the R<sup>3</sup>B setup in form of the CALIFA demonstrator, a prototype consisting of seven mechanically separate petals, each of it containing a set of 64 crystals.

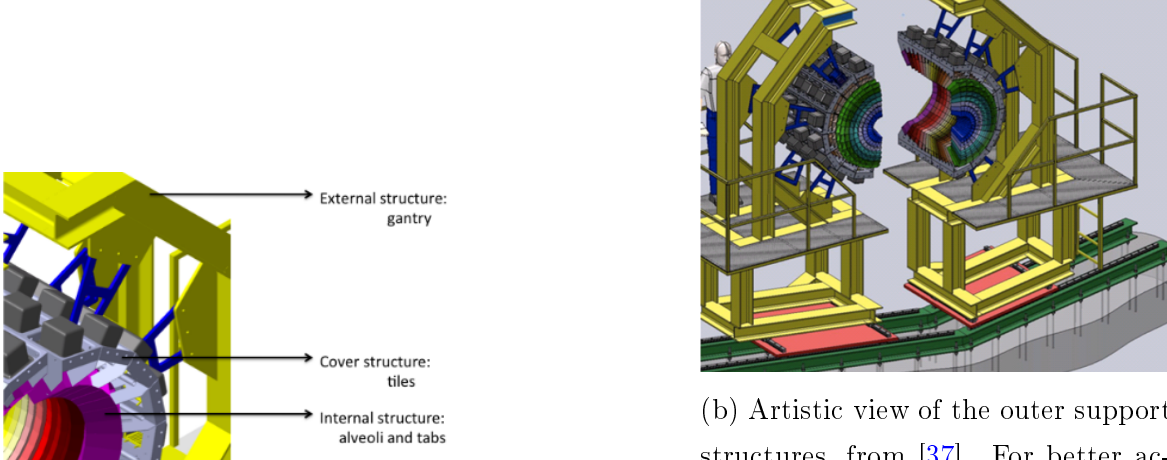
At the end of 2019 the CALIFA frame in its final design was installed and the forward barrel part ( $43^\circ \leq \theta \leq 90^\circ$  and full azimuthal coverage) was equipped with 1024 crystals.

For the S444 and the S467 experiment in 2020 CALIFA was equipped with 180 more crystals in the iPhos region ( $19^\circ \leq \theta \leq 43^\circ$ ) which corresponds to a coverage of 37.5 % in azimuthal angle for that region. Right before the S455 fissioning experiment [22] the full installation of the iPhos region was completed.

---

[36]

<sup>13</sup>To fully stop protons with  $E_{kin,p} \approx 600\text{AMeV}$  crystals with a length of 60 cm would be needed. Such long crystals would have multiple drawbacks: reduced energy resolution due to worse scintillator light transport, enhanced nuclear reactions inside the crystals and challenging demands on stability of the detector holding structure



(a) Zoomed view between inner and outer structure layers, from [35]. The black boxes symbolize the preamplifiers, which are directly mounted on the aluminium tiles.

(b) Artistic view of the outer support structures, from [37]. For better access to the target area the detector infrastructure is split into two halves, the left side commonly referred as "Messel" and the right side as "Wixhausen" (in-beam-view).

Figure 10: CALIFA internal and external holding structure

In February 2024 the full CEPA region ( $7^\circ \leq \theta \leq 19^\circ$ ) with 112 crystals was commissioned for the first time together with a new equipped part of the backward barrel ( $90^\circ \leq \theta \leq 102.5^\circ$ , 128 crystals).

### Energy and particle reconstruction with CsI(Tl) scintillator crystals

Scintillator material, as caesium iodide doped with thallium CsI(Tl), is widely used in experimental physics to detect ionizing radiation from  $\gamma$ - rays or charged particles. The energy from the incoming radiation excites the electrons in the CsI crystal from their ground state to higher energy levels (excited states). The deexcitation, followed by photon emission (scintillation light), occurs via various complex mechanisms<sup>14</sup>. The efficiency and properties of the scintillation process can be fine-tuned by doping CsI with small amounts of other materials, such as thallium. Thallium-doped Cesium Iodide produces light with a peak emission around 550 nm (green light) and has high light output<sup>15</sup>. The high density of CsI with  $4.51 \text{ g/cm}^3$  makes it to an optimal scintillator material to efficiently absorb  $\gamma$ - rays and high-energy particles. Moreover the CsI(Tl) crystal is well transparent to its own scintillation light, which is essential for the transport and consequent detection of the scintillator light. CsI(Tl) crystals are in addition relatively robust compared to other crystals and only slightly hygroscopic

<sup>14</sup>A comprehensive overview of scintillation mechanisms and the corresponding models can be found in Refs. [38, 39, 40].

<sup>15</sup>The light output per MeV deposited energy in CsI(Tl), measured in [41], resulted in  $5.2 \cdot 10^4$  (scintillation) photons/MeV.

making them suitable for long-term use in experimental setups.

In a first approximation, the total amount of emitted light is proportional to the energy deposited in the scintillator. For  $\gamma$ -rays this is valid for  $E_\gamma \gtrsim 400\text{keV}$ [42]. However, for charged particles significant deviations from linearity are observed, a so-called *quenching*[38].

Although the the energy calibration of CsI(Tl) crystals for charged particles is challenging, CsI(Tl) as such has the benefical property of having a complex time dependend light emission consisting of two distinct exponential components. The time dependend light emission response of CsI(Tl)  $L(t)$  can be approximated as:

$$L(t) = \frac{N_f}{\tau_s} \exp(-\frac{t}{\tau_f}) + \frac{N_s}{\tau_s} \exp(-\frac{t}{\tau_s}) \quad (12)$$

Where  $N_f$  is the amplitude of the fast component and  $N_s$  the amplitude of the slow component. Accordingly  $\tau_f$  the life time of the fast component ( $\tau_f \approx 650 - 770\text{ns}$ ) and  $\tau_s$  the lifetime of the slow component ( $\tau_s \approx 3.2 - 3.5\mu\text{s}$ ). It has been found that the proportion between the two components is energy and particle dependend. This property can be used to identify isotopes by extracting the  $N_f$  and  $N_s$  values from pulse shape analysis (PSA) on the according light emission response<sup>16</sup>, as shown in figure 11.

### From scintillator light to electrical signal

The scintillator light produced by the ionisation processes has first to be transported to the back-end of the crystal. The optimum design has been determined to be frustum-shaped crystals, wrapped into enhanced specular reflector (ESR) foil which provides excellent reflectivity. Finally at the backside of the crystals a large area avalanche photodiode (LAAPD) is attached<sup>17</sup>. Avalanche photodiodes (APDs) operate on the same fundamental principle as conventional photodiodes, converting scintillation light into electrical signals. However, they offer the advantage of being insensitive to magnetic fields, making them particularly suitable for applications in environments with strong magnetic interference. As a result of an additional highly doted p-layer a region with very high field is formed which accounts for amplification factors up to  $\approx 100$ .

For the next amplification step the electric signal is forwarded via thin ribbon cables to the back end of the preamplifiers from Mesytec[46] which can serve up to 32 input channels. For CALIFA two general types of peramplifiers are in use:

1. Dual Range (DR) Preamplifiers: They are used in the iPhos and CEPA region where both high energetic protons as well as gammas are expected. They cover

---

<sup>16</sup>The method has been implemented in the CALIFA Firmware as *QuickParticleIdentification – QPID*. For more information see [43] and [44]

<sup>17</sup>Detailed information about the crystal wrapping and LAAPD gluing can be found in this work:[45]

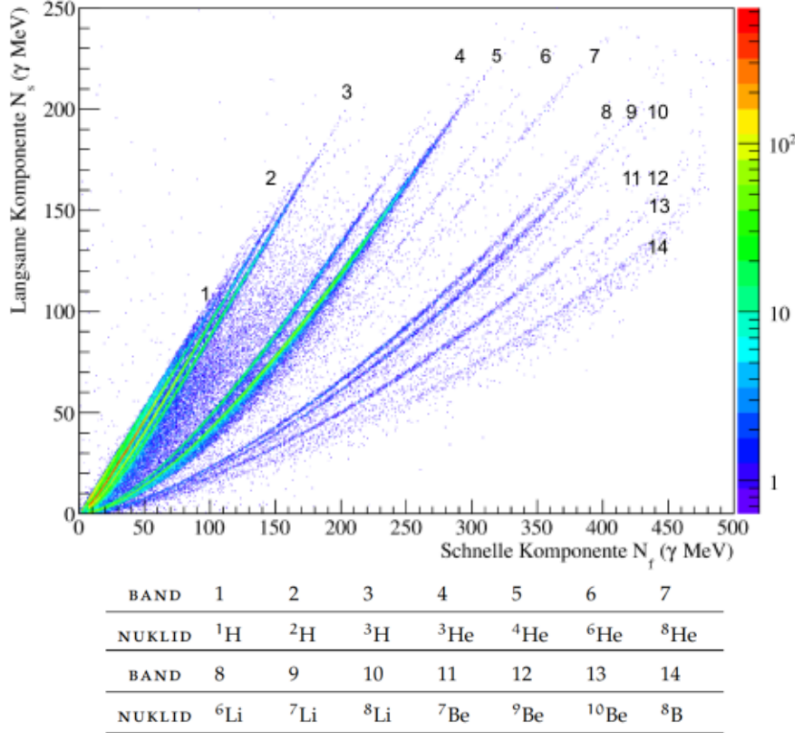


Figure 11: Quick Particle Identification(QPID) via fast and slow component  $N_f/N_f$ . Each correlation band corresponds to a nuclide, from Ref.[44].

two amplification ranges in parallel: the *gamma range* with low input signal and high amplification and the *proton range* with high input signal with low amplification. Following from this they have 64 channel differential signal output.

2. Single Range (SR) Preamplifiers: In the Barrel region, where mostly  $\gamma$  rays are expected, only one amplification range is needed. Depending on the experimental demands these preamplifiers can be switched to *gamma* or *proton range*. These preamplifiers have a 32 channel differential signal output.

The fall time for the preamplifiers  $\tau_{RC}$  has been chosen to  $\approx 35 \mu\text{s}$ . This is a trade-off between the ballistic deficit on one side (reduction of the signal amplitude due to low  $\tau_{RC}$ , see also [43], chapter 3.4.5) and rate capability (restricted by large  $\tau_{RC}$  value) on the other side.

The differential signal output of the preamplifiers is then transmitted over shielded and twisted line pairs to the input of the FEBEX Addon Boards (FAB) for further processing.

### Signal Processing and readout system

The central hardware module for the signal processing in CALIFA is the FEBEX 3B Module (Front End Board with optical link EXtension[47]). Attached on it is a so-

called AddOn board developed by TUM. The signal from the preamplifier gets here first filtered by a low pass two pole bessel filter ( $f_c \approx 25MHz$ ). Furthermore, since the input of the FEBEX ADCs cover a range of  $\pm 0.9$  V while the signal output from the preamplifier only has one polarity, an offset to the signal is applied to use the full range of the ADCs. The signal from the ADCs is read out continuously on the FEBEX card and split up into two branches:

1. Fast/trigger branch: After being fed to a trapezoidal filter the signal is examined by three leading edge discriminators with configurable thresholds. Depending on the experimental requirements a coincident matrix between one or more discriminators and optionally external triggers validates the signal as event ready for data recording.
2. Slow branch: The validated signal gets delayed over a ring buffer and a pulse shape analysis is performed via various steps - signal decimation, moving average unit -technique, baseline subtraction and moving window deconvolution (MWD) - to recall the major steps<sup>[18](#)</sup>. From the resulting pulse shape pulse height measurement the energy deposited in the scintillator is determined. In addition the algorithm for the quick particle identification (QPID) is applied on the incoming signal which provides the fast( $N_f$ ) and slow( $N_s$ ) component of the signal for isotope identification and differentiation of stopped and punch-through particles. The CALIFA Firmware also allows to make time over threshold (TOT) measurements which is convenient for energy reconstruction when the incoming signals exceed the ADC range (which might happen when the preamplifier is set to *gamma range*)<sup>[19](#)</sup>.

Central hub for internal and external trigger forwarding are the Exploder modules<sup>[\[49\]](#)</sup>. The FEBEX crates are connected over an eight fold flat cable to the Exploder to the triggerbus. The trigger bus between the data acquisition PCs and the FEBEX cards is controlled by the TRIXOR card. This card sits inside the data acquisition PCs and is connected via ECL-lines to the Exploders and the PEXOR(PCIE Optical Link Interface) card via 26 fold flat cable. The PEXOR card is responsible for the data transfer between FEBEX cards and the data aquisition PCs. It is connected via glas fibre cables to the FEBEX crates and stores locally in a 576 MB large RLDRAM (Reduced Latency

---

<sup>[18](#)</sup>A really detailed description of the pulse shape analysis in CALIFA can be found in Philipp Klenze's<sup>[\[48\]](#)</sup> and Max Winkel's thesis<sup>[\[44\]](#)</sup>.

<sup>[19](#)</sup>The TOT energy-reconstruction method has the drawback of being really sensitive to pile-up events overestimating the energy deposition. Hence more suitable for regions with low event rates, such as Barrel region.

Dynamic Random Access Memory) the data which conecutively gets transmitted via DMA (Direct Memory Access - data transmission speed up to 560 MB/s) to the RAM of the data acquisition PCs.

Since the Exploder provides various input and output lines and an internal switchable bypass matrix the CALIFA calorimeter can be operated as free running system with internal event validation only or by (additional) external validation. In case of internal validation only the signal from the preamplifiers has to exceed predefined threshold(s) to be accepted. This kind of configuration can be used for the purpose of calibration (with  $\gamma$ -ray sources like  $^{22}\text{Na}$  or  $^{60}\text{Co}$ ) and expected low event rate experiments. For high event rates and event coincidence with other subdetectors additional external validation (e.g. clean CFD signal from START detector) is implemented.

To overcome dead time initiated by the readout/data transmission procedure each FEBEX channel allows to store up to 254 recoded events on the local memory. Each FEBEX channel has two available memory banks. Whenever one FEBEX channel reaches its preconfigured maximum number of events the full FEBEX crate is read out. To avoid dead time all channels force a memory bank switch thus allowing continuous dead time free event recording.

The Multi Branch System (MBS), developed at the GSI Helmholtz Center for Heavy Ion Research, is used on the data acquisition PCs. This software consists of several components that control and read out detectors, store the data, or forward it via various network protocols. The system also allows for the joint readout of multiple systems. For this, the trigger modules (TRIXOR) are connected via a special trigger bus to exchange trigger signals and dead time information. The triggered data is then collected, time sorted and cross-detector events are build by the dedicated MBS event builder<sup>[20](#)</sup>.

### 3.3.6 Sofia Time of Flight Wall

The Sofia Time of Flight Wall (or "Stop detector") is positioned at the very end of the experiment setup at approximately 6.6 m distance from the target position. It consists of a plane of 28 vertically aligned scintillator bars, each of dimension 32x600x5 mm. The scintillator plastics are numbered from 0 to 27 from left to right (when looking in beam direction). The time of flight of the ions between Start and ToFW can be measured by substracting the time measurement of the Start detector from the ToFW. In optimal operating conditions, the combined time resolution of the Start and TOFW detectors can reach 40 ps, enabling precise time-of-flight measurements, for an average time of flight of 30 ns[[33](#)]. For the technical specifications of the Sofia ToFW, see table

---

<sup>20</sup>A more detailed explanation about the readout system and the critical FEBEX timing topic can be found in Philipp Klenze's thesis [[48](#)].



Figure 12: Sofia ToFW in Cave C, from [33].

Plastic	EJ-232, no quencher
Plastic dimensions	5x32x600 mm <sup>3</sup>
Detector dimension	5x900x600 mm <sup>3</sup> (28 plastics)
Photo-multiplier tubes	Hamamatsu 6533 and 10580
Total number of PMTs	56 (two per plastic - top and bottom)

Table 4: Sofia ToFW - Technical specifications

4 and reference [50].

### 3.3.7 NeuLAND Detector

For the detection of knocked-out or evaporated neutrons the **New Large-Area Neutron Detector (NeuLAND)** is installed at zero degrees after GLAD. In its final design it will consist of 30 double planes with each 100 plastic scintillators of size 5x5x250 cm<sup>3</sup> providing an active detector surface of 2.5x2.5 m<sup>2</sup> and thickness of 3m. Its high detection efficiency, a time resolution of  $\sigma_t \leq 150\text{ps}$  and a mult-neutron efficiency of 50% to 70% for four-neutron events are crucial detector features for complete kinematics experiments at R<sup>3</sup>B. For more detailed information, see [51] and [52].

For the S444 commissioning experiment in 2020 eight double-planes of the NeuLAND detector have been used.

## 4 Analysis - Total Interaction Cross Section of $^{12}\text{C}$ + $^{12}\text{C}$

This chapter will go through the analysis step by step from the unpacking stage to the final measurement of the total interaction cross section. It will start by a short overview of the transmission method used for the cross section measurements. The next step is the selection of clean incoming  $^{12}\text{C}$  isotopes. Following the identification of the carbon isotopes after the target - for the measurement of the charge changing cross section - and as final step the interaction cross section measurement.

All relevant detector related geometrical and efficiency corrections will be addressed and their influence to the final result and its uncertainty will be discussed.

### 4.1 Cross Section Measurement via Transmission Method

In its most generic form cross sections give a measure of the probability that a specific reaction will take place when two or more particles collide. The cross sections measured in scattering experiments, as well as the energy and angular distribution of the reaction products, provide information about the dynamics of the interaction between the projectile and the target particle, i.e., about the shape of the interaction potential and the coupling strength.

The cross section  $\sigma$  can be derived by looking at the relation between the number of incoming particles ( $N_1$ ) and unreacted particles after the target ( $N_2$ ). For an experiment with fixed target with thickness  $z$  and volumetric number density  $n$  the number of reacted particles in the infinitesimal thin target layer  $dz$  can be expressed as:

$$\frac{dN_2}{dz} = -n\sigma N_2 \quad (13)$$

Solving this differential equation for  $N_2$  (with the condition  $N_2 = N_1$  for  $z = 0$ ) discloses an exponential relation:

$$N_2 = N_1 e^{-n\sigma z} = N_1 e^{-N_t \sigma} \quad (14)$$

Where  $n \cdot z$  can be summarized as  $N_t$ , the total number of scattering centers per unit area. The relation  $(N_2/N_1)$ , number of unreacted particles after the target versus number of incoming particles, is often called survival probability  $P_{surv}$ . For an idealistic experimental setup with full detector efficiency and no interactions in the setup material the cross section could simply be deduced from equation 14. To account for reactions of the projectile that occur within the setup material and first order detector specific distortions of output signals the survival probability  $(N_2/N_1)$  has to be divided by the survival probability for an empty target run  $P_{surv}^E = (N_2^E/N_1^E)$ , where  $N_1^E$  is

the number of incoming particles and  $N_2^E$  the number of unreacted particles after the target for an empty run respectively. Thereby the setup specific efficiency( $\epsilon_{setup}$ ) and transmission factor( $t_{setup}$ ) are cancelled out to obtain the underlying number of unreacted particles after the target  $\tilde{N}_2$ :

$$N_2 = \tilde{N}_2 \cdot t_{setup} \cdot \epsilon_{setup}$$

$$N_2^E = \tilde{N}_2^E \cdot \epsilon_{setup} \text{ with } \frac{\tilde{N}_2^E}{N_1^E} \text{ the setup specific transmission factor } t_{setup}$$

The final formula for the cross section for a so called transmission measurement is:

$$\sigma = -\frac{1}{N_t} \ln\left(\frac{N_1^E}{N_2^E} \cdot \frac{N_2}{N_1}\right) = -\frac{1}{N_t} \ln\left(\frac{N_1^E}{\tilde{N}_2^E \cdot \epsilon_{setup}} \cdot \frac{\tilde{N}_2 \cdot t_{setup} \cdot \epsilon_{setup}}{N_1}\right)$$

With  $\frac{\tilde{N}_2^E}{N_1^E} = t_{setup}$  (15)

$$\sigma = -\frac{1}{N_t} \ln\left(\frac{1}{t_{setup}} \cdot \frac{\tilde{N}_2 \cdot t_{setup}}{N_1}\right) = -\frac{1}{N_t} \ln\left(\frac{\tilde{N}_2}{N_1}\right)$$

From the above formula 15 it is evident that for cross section measurements with the transmission method three types of observables have to be measured:

## ■ Number of scattering centers $N_t$

The number of scattering centers per unit area of the target is a target specific number. It depends from the target thickness and and its density. The values herefore are taken from [53]<sup>21</sup>:

(a) Thin target:

target thickness  $d = 0.5451 \text{ cm}$ ;  $N_t = 5.0588795 \cdot 10^{22}$ ;  $\Delta N_t = 0.0648\%$

(b) Medium target:

target thickness  $d = 1.0793 \text{ cm}$ ;  $N_t = 1.0016600 \cdot 10^{23}$ ;  $\Delta N_t = 0.2620\%$

(c) Thick target:

target thickness  $d = 2.1928 \text{ cm}$ ;  $N_t = 2.0350598 \cdot 10^{23}$ ;  $\Delta N_t = 0.0322\%$

where  $N_t$  was calculated by:

$$N_t = \frac{\rho \cdot d \cdot N_A}{M} \quad (16)$$

with  $\rho$  the target density<sup>22</sup>,  $N_A$  the Avogadro constant ( $6.02214076 \cdot 10^{23} \text{ mol}^{-1}$ ) and  $M$  the molar mass of the target (for carbon  $M = 12.011 \text{ g} \cdot \text{mol}^{-1}$ ).

---

<sup>21</sup>For the purpose of this work the target thicknesses were remeasured at GSI with a chromatic sensor giving 2D depth profiles of each target.

<sup>22</sup> $\rho = 1.851 \text{ g/cm}^3$ , from [53]

### ■ Number of incoming projectiles ( $^{12}\text{C}$ ) $N_1$

For the measurement only events with well identified incoming  $^{12}\text{C}$  projectiles are chosen. Herefore strict cuts on the detectors upstream the target area are set. This strict event selection makes sure that we only consider events with single  $^{12}\text{C}$ . This will be discussed in more detail in section 4.2.

### ■ Number of unreacted projectiles ( $^{12}\text{C}$ ) $N_2$ after the target

Detectors downstream the target area are used to count the number of unreacted projectiles  $^{12}\text{C}$ . To reduce detector specific influences which could distort the result it is advisable to use only as few as requirable detectors for the clear identification of unreacted projectiles. Moreover detector specific efficiencies are cancelled out by including both empty and target runs in the cross section calculation(see equation15). For all downstream detectors used in this analysis it is critical to minimize any selection cuts and systematically check their effects on  $N_2$ .

## 4.2 Event Selection

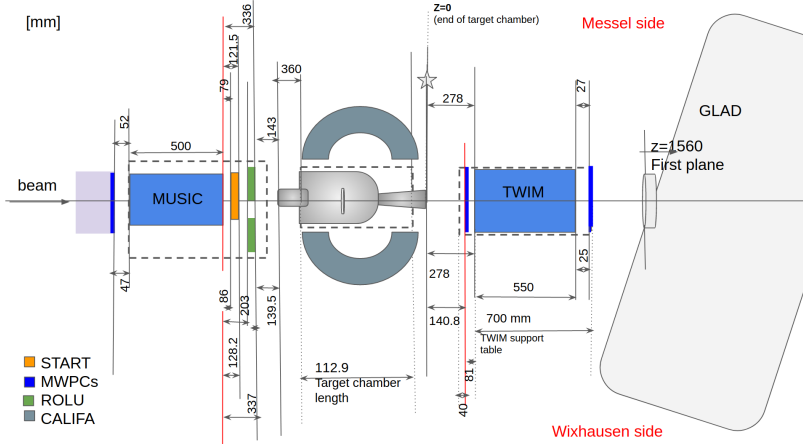


Figure 13:  $\text{R}^3\text{B}$  setup for the S444 experiment in the target region. TODO: select overview with less numbers/measures...

For event selection, all three upstream detectors are utilized: the MWPC0, the  $\text{R}^3\text{B}$  MUSIC Ionization Chamber, and the start detector. To ensure a clean incoming event selection, the following prerequisites must be met:

1.  **$^{12}\text{C}$  identification of incoming projectile by upstream detectors:**

In the S444 experiment the incoming beam was directly delivered by the SIS18 ring accelerator, which is operated in ultra-high vacuum. Herefore the level of contamination is low.

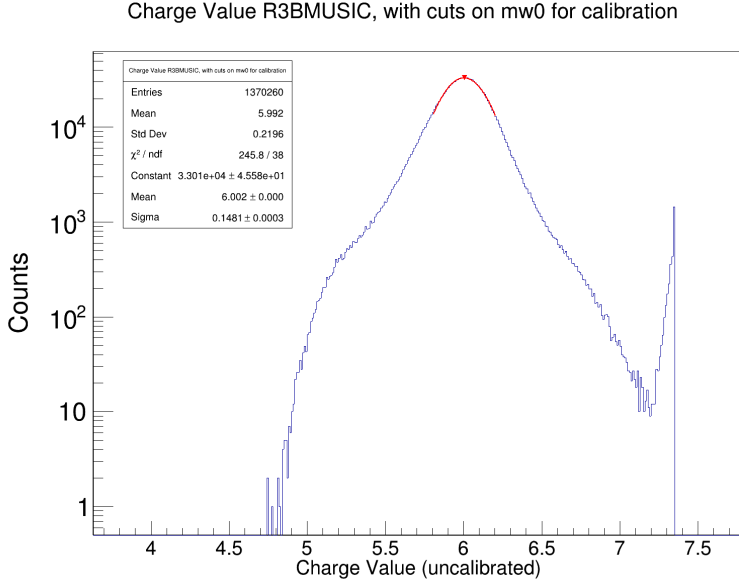


Figure 14: Charge distribution on  $\text{R}^3\text{B}$  MUSIC with predefined calibration parameters with already applied positional cuts on MWPC0 - positioned upstream to the ionisation chamber. The rise beyond  $Z \geq 7.2$  comes from pile-up events.

For the charge identification of the incoming ion the  $\text{R}^3\text{B}$  MUSIC ionisation chamber is used which is positioned directly after the MWPC0 at the beam entrance in Cave C, see figure 13. The  $\text{R}^3\text{B}$  MUSIC detector measures anode-wise the energy loss of the passing-through ion which in the first order is proportional to the square of its charge ( $\Delta E \sim Z^2$ ). Therefore the calibration parameters from the online analysis are used<sup>23</sup>. Figure 14 shows the measured charge distribution in  $\text{R}^3\text{B}$  MUSIC. To select  $Z = 6$  incoming ions the distribution is fitted with a gaussian fit function. All ions with charge within the  $\pm 1\sigma$  range are accepted. Figure 15 summarizes the  $\pm 1\sigma$  cuts on the  $\text{R}^3\text{B}$  MUSIC charge for empty/target runs for all beam energies.

## 2. Pileup rejection and TPat selection:

The overall recoding and merging of the data from various subdetectors is one of the tasks of the Data Acquisition (DAQ) system. Whether an event is recorded or not depends on the pre-established trigger logic. Various detectors can send out triggers to the main DAQ when certain conditions are given (e.g. CALIFA can be configured to send out a trigger when a hit with more than 20 MeV is recorded in the calorimeter). The different triggers are processed by the trigger logic and summarized as a defined trigger pattern, so called TPat, which is stored in a 16-bit mask for each event. Table 5 gives an overview of the trigger logic

---

<sup>23</sup>These are generic parameter values used to the detector performance during the experiment phase.

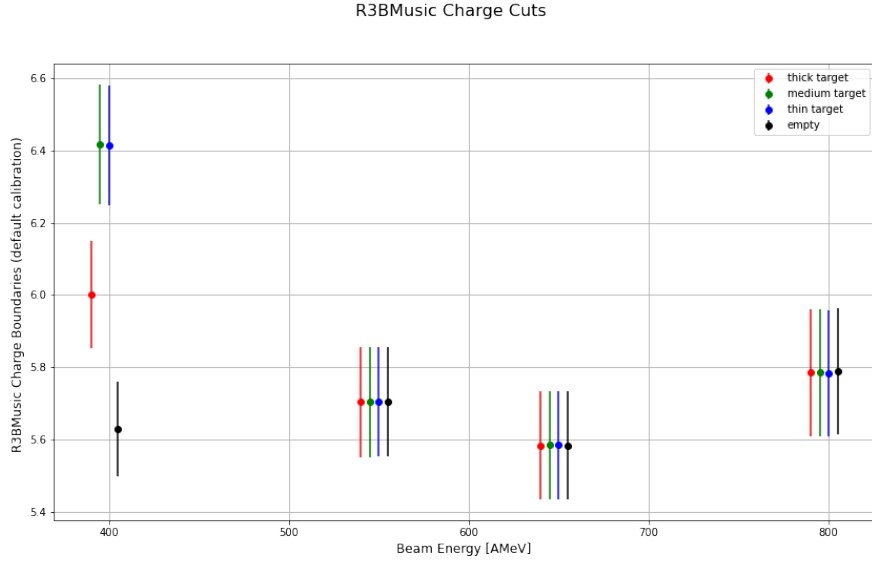


Figure 15: Strict  $\pm 1\sigma$  charge cuts with  $R^3B$  MUSIC for incoming particle selection. Fixed predefined calibration parameters were used which do not compensate different gain settings between runs. This is in particular the case for the 400 AMeV beam energy runs.

and the trigger patterns set in the S444 experiment. For this analysis the "*Min. Bias*" trigger is required<sup>24</sup>.

Since the TPat selection itself does not necessary set any pileup constraints it

Bit Position	TPat Name	Description
0	Min Bias	Hit in Start detector
1	Reaction	"CalifaOR" -high energy hit in CALIFA
2	Neutron	Hit in NeuLAND
3	p+n	Hit in CALIFA and Neuland
8	Califa	high energy hit in califa - off-spill
9	NeuLAND	Hit in NeuLAND - off-spill

Table 5: List of TPats set for S444 experiment. As for the selected runs low beam rates ( $< 10kHz$ ) were expected no dead time issues should arise for the in-beam detectors, therefore no downscaling of the *Min. Bias* TPat was deployed.

is important to analyse the signals of the detectors upstream carefully to insure yourself that only events with one incoming  $^{12}\text{C}$  ion at a time get selected. Here-

<sup>24</sup>This includes also "*Reaction*" and "*Neutron*" TPat since these patterns contain also "*Min. Bias*" TPat as necessary condition.

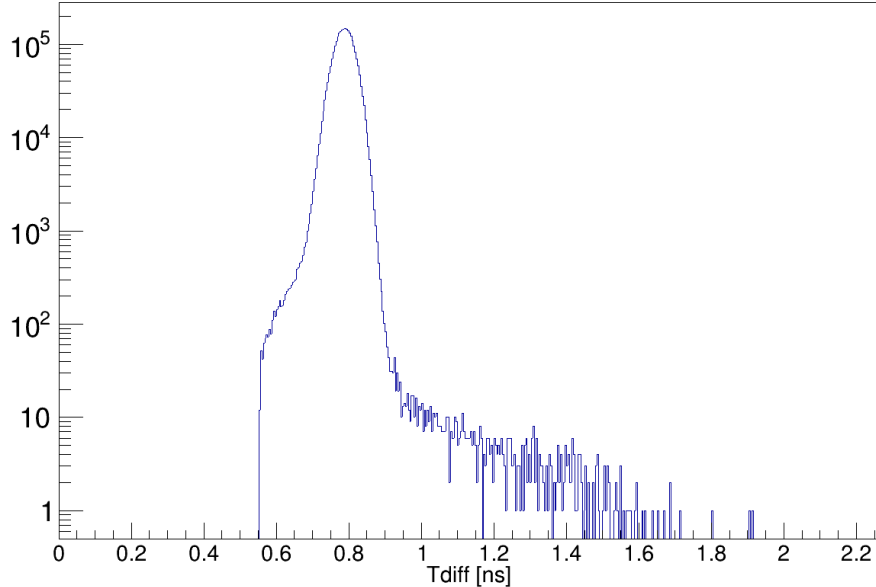


Figure 16:  $\Delta t_{\text{right-left}}$  between hits in the Start detector for events with exactly one hit on the left and right preamplifier and limiting the time difference in the range 0.555 ns to 1.946ns.

fore events with incoming ions with charge  $Z = 6 \pm 1\sigma$  are chosen, as discussed in the previous point. Moreover it is required that both left and right preamplifiers of the start detector have seen a coincident signal within a time-window of 1.391 ns.—TODO: why this time window?— The overall searching window of the start detector was set to 2  $\mu\text{s}$ , see figure 16. For the MWPC0 which is mounted right at the beam entrance of Cave C no hit multiplicity cuts were applied considering its operating mode, which is designed for charge sharing between the readout pads.

### 3. Projectile's focus on the active target region:

To assure that the incoming  $^{12}\text{C}$  ion hits the target it is necessary to select only events where the projectile is focussed to the active target region. Therefore strict cuts on the MWPC0 x and y position are applied. This was achieved by fitting the x and y distribution of the MWPC0 (without any restrictions on it) by a gaussian function. The selection of focused incoming projectiles was then restricted to events with hits in MWPC0 within the  $\pm 1\sigma$  region in the x and y position, see figure 17 and 18.

The MWPC0 x-position and the available projectile angle in the x-y plane from the R<sup>3</sup>B MUSIC is used to propagate the corresponding x-position on the target location to further check that the selected projectiles hit the target parallel to the z-position (= beam direction) and do only have a minimal incident angle, see figure 19.

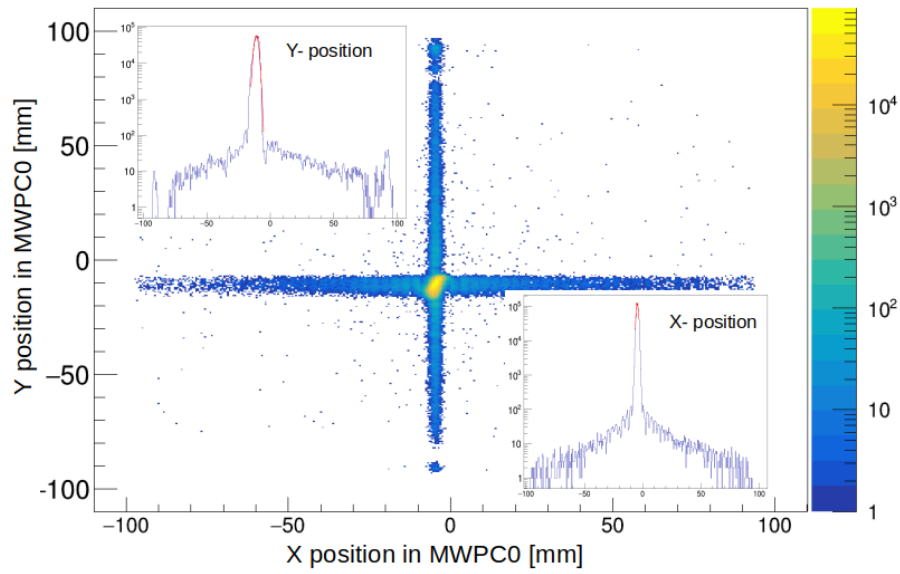


Figure 17: x-y position of incoming ion on MWPC0.

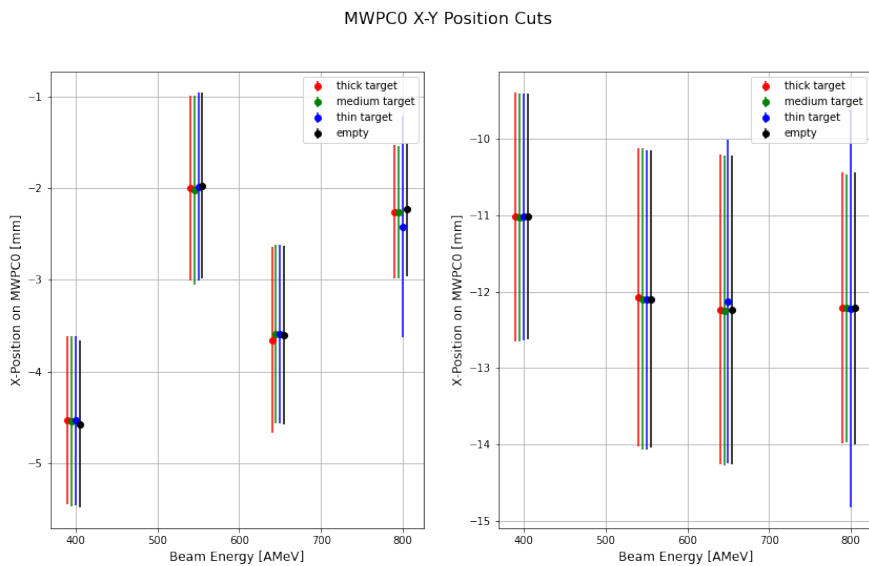


Figure 18: Overview of  $\pm 1\sigma$  cuts in x and y in MWPC0 for empty/target runs. TODO: labelling on the right side is wrong! (should be y!)

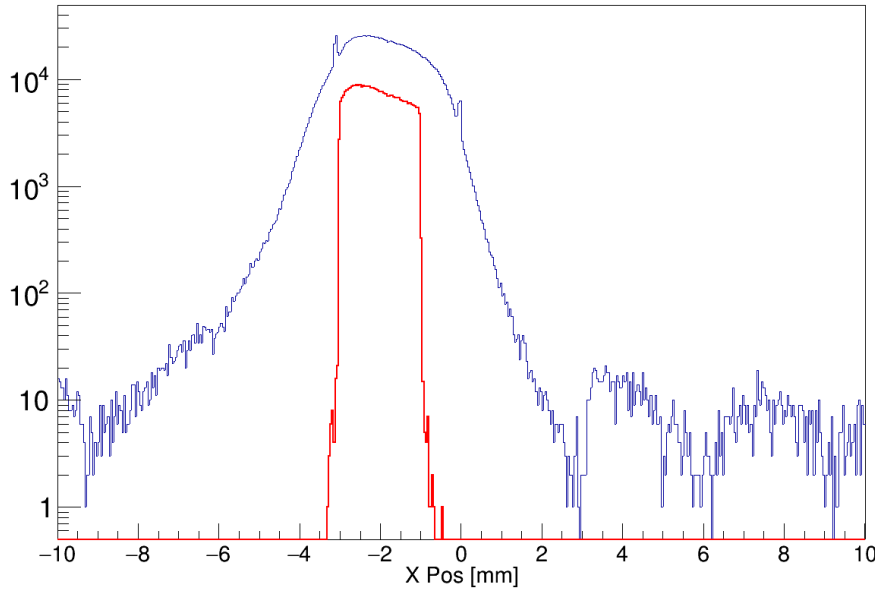


Figure 19: Propagated x-position on target location from measured x-value on MWPC0 and x-y plane angle measurement from R<sup>3</sup>B MUSIC. The target area is 3 x 3 cm. In red the selected events with  $\pm 1\sigma$  cut in x and y position in MWPC0, in blue all events. TODO: which run is this?

### 4.3 Charge Changing Cross Section Measurement

The charge changing cross section refers to a measure of the probability that the incoming projectile will undergo a reaction inside the target that changes its charge. To measure the charge changing cross section it can be referred to formula 15 where in this case  $N_2$  is the number of survived carbon isotopes, i.e. projectiles which did not change their charge state. For this measurement only the data from the double ionisation chamber TWIN MUSIC (see section 3.3.2) needs to be read out and analyzed.

While for the event selection before the target the cut conditions can be arbitrarily strict (it will only have an impact to the statistics and the derived statistical error), cuts on the downstream detectors need to be avoided if at all possible. Too selective cuts on the identification of  $N_2$  can distort the measurement.

#### 4.3.1 TWIN MUSIC Calibration

For the analysis of data in TWIN MUSIC – different to the upstream detectors, where calibrated data with default calibration parameters is used – the so called *mapped* raw level data is processed. In the mapped level TWIN MUSIC provides following information:

- **SectionID:** The detector is a double ionisation chamber and as such divided into

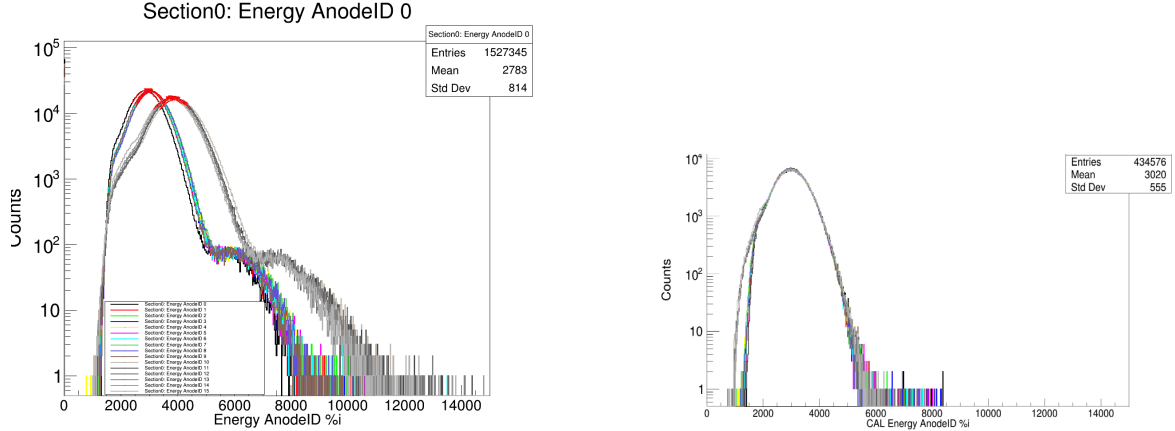
four parts (in beam perspective): section 1 - right down; section 2 - right up; section 3 - left down; section 4 - left up. For the S444 experiment only section 1 was operated and accordingly centered on the beam spot.

- **AnodeID:** TWIN MUSIC has 16 anodes for energy-loss readout and one reference anode (anodeID = 17).
- **Time:** Each hit in each anode gets assigned to a time. Each time has individually no meaning. The drift time (in ns) of the electrons from the ionisation process of the gas by the inflying projectile (or the fragments of it) to the anode is calculated by subtracting the individual anode time by the time of the reference anode. The reference anode receives its clean signal from a constant fraction discriminator of the start detector.
- **Energy:** Each hit in each anode gets assigned to an energy - except the hit in the reference anode. To reconstruct the charge of the crossing through charged particle anodewise or detectorwise the parametrization formula  $Z = [0] + [1]*\sqrt{E} + [2]*E$  is used.

The calibration of the TWIN energy for each anode is done run-wise. For the TWIN MUSIC only events where all anodes having exactly one hit (including the reference anode) are chosen. The most prominent peak ( $Z = 6$ ) was fitted with gaussian function. The calibration was then done by determining the scaling factor for each anode that shifts the mean of the gaussian fits to the same position, see figure 20. For this analysis the peaks were shifted to  $\Delta E = 6$ . Since  $\Delta E \propto Z^2$  holds, the scaled  $\Delta E$  value, even though peaking at 6, is not equate the charge  $Z = 6$ .

### 4.3.2 TWIN MUSIC Event Selection

As previously stated cuts on the downstream detectors are avoided. However, events which have hits in one or several anodes in TWIN MUSIC but no signal in the reference anode are discarded as a whole neither contributing to  $N_1$  (incoming selected ions) nor to  $N_2$  (unreacted ions). If no reference time from start CFD signal is available it is not possible to measure the drift time in the individual anodes which makes it not possible to distinguish between signal and noise hits for multi-hit anode events in TWIN MUSIC. The number of events affected by this cut is in the region of few tens. This is negligible to the number of incoming ions  $N_1$  and should not have any dependence whether the projectile reacted or not.



(a) Uncalibrated raw  $\Delta E$  distributions for all 16 anodes for the thick target run, 550 AMeV beam energy. The last six anodes have a slightly different electronics amplification chain.

(b) Gaussian fit applied to prominent peak and shifted to same position.

Figure 20: Fitting procedure in TWIN.TODO: nicer labeling!

#### 4.3.3 Carbon Identification

The identification of carbon isotopes in TWIN is done by reconstructing fragments with charge  $Z = 6$  from 2D plots where coincident mean energy losses  $\Delta E$  for different anode combinations are plotted. Since the TWIN MUSIC is multi-hit capable various strategies were developed to deal with multi-hit events, i.e. when having anodes with multiple hits, decide which hit originates from the final state products from the reaction and which from background and noise.

The default strategy is to use the time information of each hit for selection. It has to be remarked that for the S444 experiment the TWIN MUSIC was read out by two independent MDPP modules[54]. The signals from the first reference anode and the first eight upstream anodes were sent to module 1, the ones from the last eight downstream anodes and the second reference anode were forwarded to module 2. For the first eight upstream anodes the drift time is calculated by subtracting the hit time in each anode by the reference time from the first reference anode and for the last eight downstream anodes accordingly the second reference anode was used.

The time based selection algorithm for multi-hit anodes works as follows:

1. Get the mean drift time for the eight upstream anodes( $t_{mean\_up}$ ) and the eight downstream anodes( $t_{mean\_down}$ )<sup>25</sup>. Anodes with multiple hits do not contribute

<sup>25</sup>For the case all eight downstream anodes have multiple hits, set  $t_{mean\_down} = t_{mean\_up}$  and vice

# incoming projectiles $N_1$	400 MeV/nucleon	550 MeV/nucleon	650 MeV/nucleon	800 MeV/nucleon
Empty	574279(*451*)	453729(*34*)	522451(*44*)	395451(*52*)
thin	569503(*422*)	476323(*33*)	538037(*43*)	481459(*36*)
medium	606578(*431*)	451137(*27*)	500688(*40*)	345654(*46*)
thick	655762(*497*)	436457(*30*)	530869(*29*)	479679(*61*)

(a) Number of clean selected incoming  $^{12}\text{C}$  ions. In brackets number of rejected events because of missing tref in TWIN MUSIC. TODO: change the bracket notation, looks like error number!!

# survived carbon isotopes $N_2$	400 MeV/nucleon	550 MeV/nucleon	650 MeV/nucleon	800 MeV/nucleon
Empty	563382(1.898%)	444618(2.008%)	511923(2.015%)	387513(2.007%)
thin	538245(5.489%)	449422(5.648%)	507557(5.665%)	454099(5.683%)
medium	552763(8.872%)	410376(9.035%)	455159(9.093%)	314119(9.123%)
thick	553935(15.528%)	368004(15.684%)	446115(15.965%)	402696(16.049%)

(b) Number of survived carbon isotopes after the target identified via 2D gaussian fit with borders within  $3.5\sigma$  cut. In brackets the percentage of projectiles with a charge state of  $Z < 6$  after the target.

Table 6: Numbers of incoming projectiles  $N_1$  and survived carbon isotopes  $N_2$  for all energy and target runs.

to this calculation.

2. If there are anodes with multiple hits compare the hit time with the according mean drift time ( $t_{mean\_up}$  for any of the eight upstream anodes,  $t_{mean\_down}$  for any of the eight downstream anodes). Calculate herefore the absolute difference between mean drift time and each hit time:

$$\Delta t = |\bar{t} - t_{drift}^i|; i = \text{anodeID } (1-16) \text{ with } \bar{t} = \begin{cases} t_{mean\_up} & \text{for } i \leq 8 \\ t_{mean\_down} & \text{for } i \geq 9 \end{cases} \quad (17)$$

3. For each anodes with multiple hits select the hit with lowest drift time difference to the mean drift time.

After having selected the appropriate hit for single and multi-hit anodes the mean value for the pre-calibrated  $\Delta E$  loss, see figure 20b, for the eight upstream and accordingly for the eight downstream anodes is determined. Finally, to select the number of anodes with multiple hits to be considered for the analysis, the following selection criteria is applied. The selection is done in two steps. First, the number of anodes with multiple hits is limited to a maximum of 4. Second, the number of anodes with multiple hits is limited to a maximum of 2. This is done to avoid that the analysis is dominated by anodes with multiple hits. The selection is done in two steps. First, the number of anodes with multiple hits is limited to a maximum of 4. Second, the number of anodes with multiple hits is limited to a maximum of 2. This is done to avoid that the analysis is dominated by anodes with multiple hits.

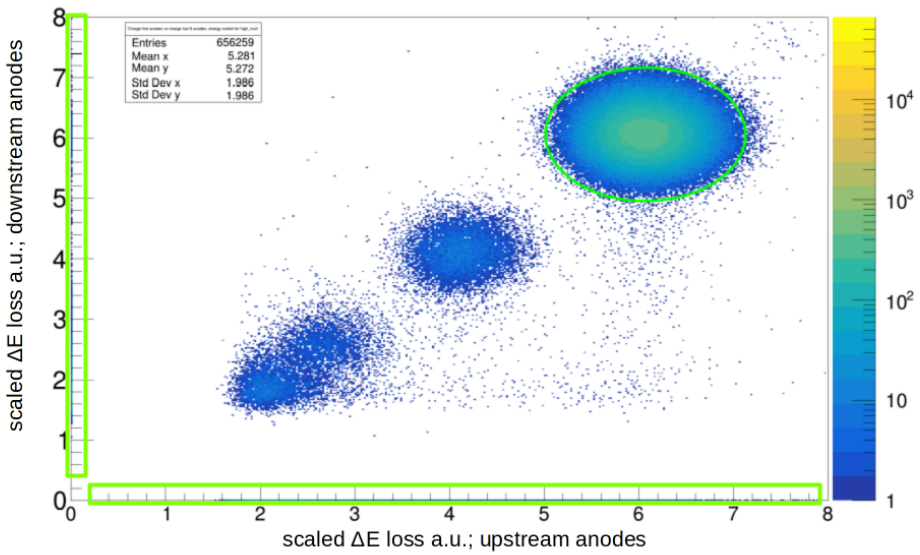


Figure 21: Two dimensional gaussian fit with  $3.5\sigma$  cut on identified carbon isotopes in TWIN MUSIC. The horizontal and vertical side bars contain events where either the eight upstream anodes or downstream anodes have no hit entry. The cluster at scaled  $\Delta E$  loss  $\approx 4.5$  corresponds to boron isotopes ( $Z=5$ ). The clusters for  $Z=4$  (Be) and  $Z=3$  (Li) overlap.

survived carbon isotopes the mean  $\Delta E$  of the eight upstream anodes versus the mean  $\Delta E$  of the eight downstream anodes is plotted. To retrieve the number of survived carbon isotopes following two-dimensional gaussian fit is applied on the 2D plot on the charge  $Z = 6$  blob, see figure 21:

$$f(x) = Ae^{-\frac{1}{2}\left(\left(\frac{x-\bar{x}}{\sigma_x}\right)^2 + \left(\frac{y-\bar{y}}{\sigma_y}\right)^2\right)} \quad (18)$$

where  $x$  is the mean rescaled energy loss of the first upstream anodes and  $y$  the according eight downstream anodes. The number of survived carbon isotopes is given by the integral of events within the 2D gaussian fit. Since the anodes were read out by two independent MDPP modules with slightly different thresholds also events along the histogram axes with no hit entry in either the upstream anodes or downstream anodes are analyzed. For those events a one dimensional gaussian cut is applied using the parameters from equation 18 (see horizontal and vertical bars in figure 21).

To get the charge changing cross section values equation 15 has to be applied where both the number of survived carbon isotopes for target run and empty run are determined via the 2D gaussian fit as in figure 21. The number of target particles, are defined by the target thickness and its density and are listed in section 4.1. The resulting charge changing cross sections are summarized in figure 22 once with consideration of the vertical/horizontal bars in figure 21 and once without. Hits within the  $3.5\sigma$  gaussian

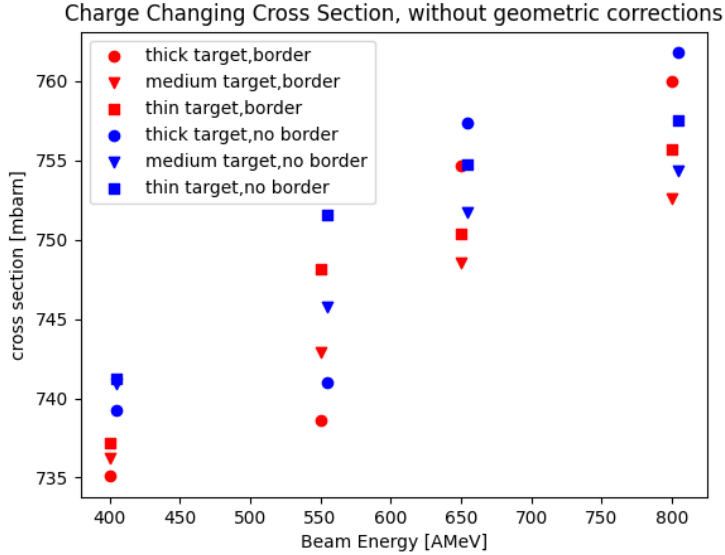


Figure 22: Charge changing cross section without geometry corrections. The red data points result from considering also events with only hits in the upstream or downstream anodes, the blue data points don't take these events in consideration.

fit are identified as carbon isotopes. To get the optimal  $\sigma$  cut on the two dimensional gaussian fit on the energy losses of the upstream anodes versus downstream anodes the charge changing cross section for all targets and all energies was systematically measured for  $\sigma$ -cuts in the range of 1 to 5  $\sigma$ , see figure 23. In the region  $\sim 3.5\sigma$  the variation of the cross section is minimal.

Another method to assert the number survived carbon ions is to apply a diagonal cut

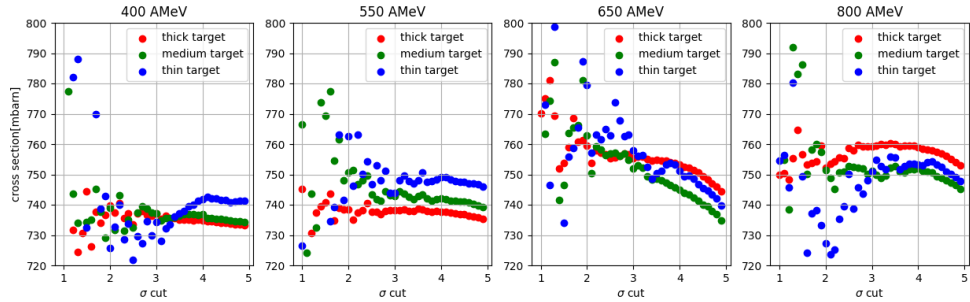


Figure 23: Measured charge changing cross sections according to the  $\sigma$  cut applied on the figure 21 (with borders) for the different target thicknesses and beam energies.

on the 2D  $\Delta E$  histogram. To set the slope and offset of the diagonal cut line firstly the two dimensional gaussian fit is applied, same as for the previous method. Then the intersection point between the  $3.5\sigma$  ellipse and the identity line ( $\Delta E$  upstream anodes =  $\Delta E$  downstream anodes) is found. Through this point, perpendicular to

the identity line, the diagonal line is drawn. Everything above the diagonal line is considered as survived carbon ions. Moreover the borders are considered within the  $3.5\sigma$  cut, see figure 24. The effects of the two different methods used for the identification

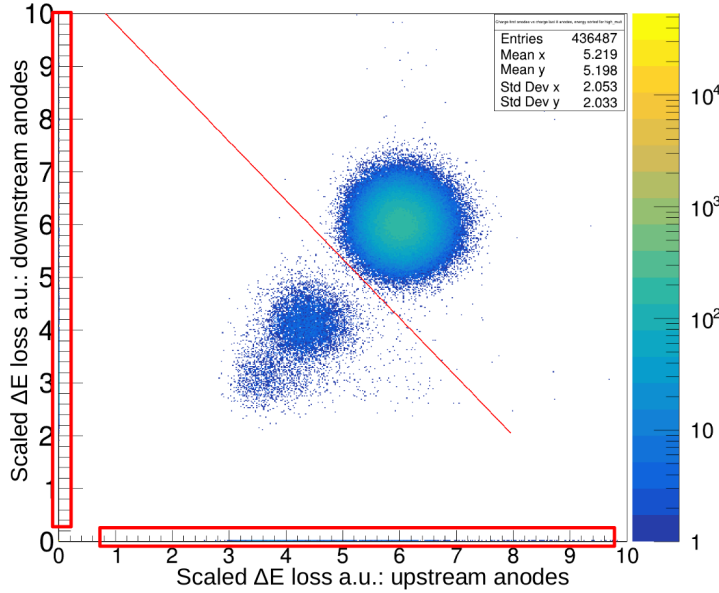


Figure 24: Diagonal cut on identified carbon isotopes along the gaussian  $3.5\sigma$  cut with borders. All hits above the diagonal line are counted as carbon isotopes. Histogram from thick target run, 550 AMeV beam energy.

of the carbon isotopes for the charge changing cross section is summarized in figure 25. The differences in the measured cross sections are within the margin of error herefore both methods are comparable, as expected. To check wether single anodes or groups of anodes are malfunctioning the charge changing cross section measurement was repeated using only certain anodes for the charge identification:

- a) anodes 2-8 versus anodes 9-15 (omitting first and last anode)
- b) anodes 1-4 versus anodes 5-8 (upstream anodes)
- c) anodes 5-8 versus anodes 9-12 (central anodes)
- d) anodes 9-12 versus anodes 13-16 (downstream anodes)

The results from the measurement are summarized in figure 26. The difference between the default gaussian fit method (with  $3.5\sigma$  cut and considering the borders) considering all 16 anodes and applying the same method but omitting the first and last anode is minimal over all four beam energies. When selecting only 8 out of 16 anodes instead the cross sections are systematically lower when going to high beam energies. The energy loss inside the TWIN MUSIC decreases with higher beam intensities, according to the Bethe-Bloch formula:

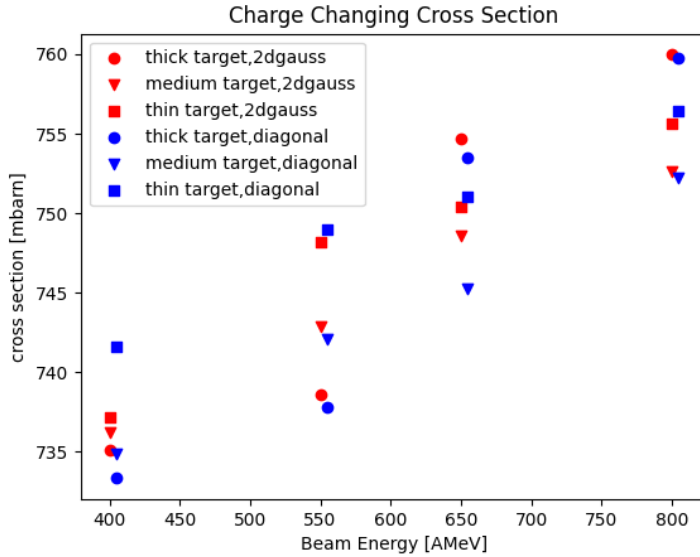


Figure 25: Comparison of charge changing cross section measured via 2D gaussian fit cut and diagonal cut. The differences are within the margin of error.

$$-\frac{dE}{dx} = K z^2 \frac{Z}{A} \frac{1}{\beta^2} \left( \frac{1}{2} \ln \frac{2m_e c^2 \beta^2 \gamma^2 T_{\max}}{I^2} - \beta^2 - \frac{\delta(\beta\gamma)}{2} \right) \quad (19)$$

where:

$$K = 4\pi N_A r_e^2 m_e c^2 \approx 0.307 \text{ MeV cm}^2 \text{ g}^{-1},$$

$z$  = charge of the incident particle (in elementary charge units),

$Z$  = atomic number of the target material,

$A$  = atomic mass of the target material,

$\beta = \frac{v}{c}$  = velocity of the particle relative to the speed of light,

$\gamma = \frac{1}{\sqrt{1 - \beta^2}}$  = Lorentz factor,

$T_{\max}$  = maximum kinetic energy transferable to an electron in one collision,

$I$  = mean excitation potential of the target material,

$\delta(\beta\gamma)$  = density effect correction.

The behaviour of  $dE/dx$  for small  $\beta$ - values are dominated by the  $1/\beta^2$  term. The decrease of deposited energy for larger beam energies has as consequence a lower relative resolution in the two dimensional  $\Delta E$  loss histogram (see figure 21) reflecting the poissonian distribution properties. In addition reducing the number of readout anodes by a factor two degrades the resolution by a factor  $\sqrt{2}$ <sup>26</sup>. This has as consequence that

<sup>26</sup>It can be assumed a similar  $\Delta E$  distribution for all anodes. Hence the central limit theorem can

the ellipsis with  $3.5\sigma$  cut incorporates a non negligible amount of boron isotopes which are counted as survived carbon isotopes which in turn reduces the measured charge chaning cross section.

While in the above measurements a time based selection algorithm for multi-hit an-

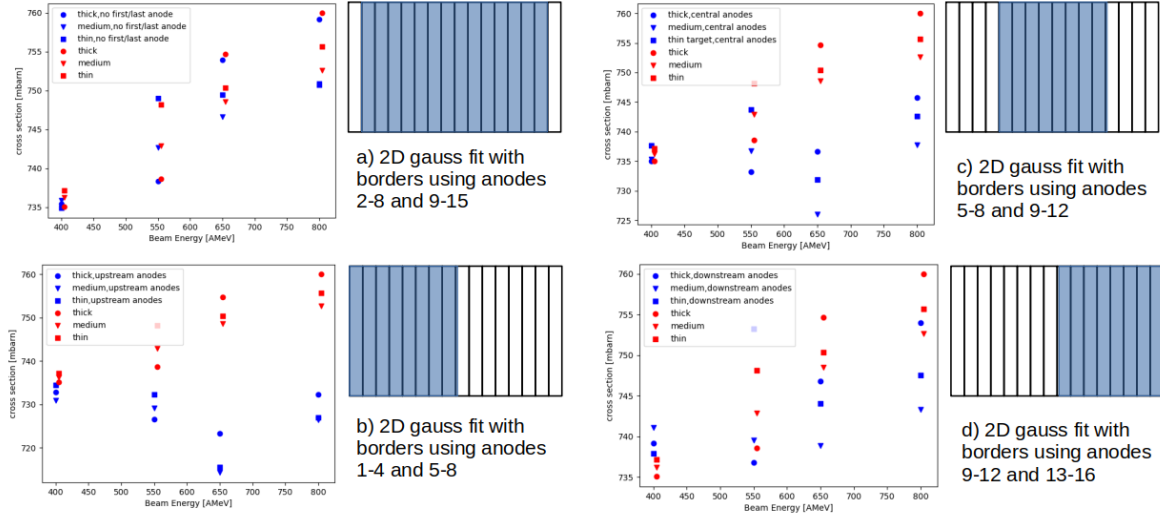


Figure 26: Measurement of charge changing cross sections using different anode sections to make the two dimensional gaussian fit on the identified carbon isotopes. Red: using all 16 anodes. Blue: the various combinations.

odes was used also an energy based selection was tested. This algorithm selects for multi-hit anodes the hit with the highest energy as physical hit and discards all others, as they are considered as background/noise. Figure 27 compares the time based method versus the energy based method. In both cases a two dimensional gaussian  $3.5\sigma$  cut is applied as in figure 21 and the borders are counted as well. The difference in the outcome is negligible. This can be explained since noise or background signal should be both uncorrelated to the event time and at a low energy level and are therefore filtered by both algorithms. The final charge changing cross section measurements with 2D gaussian fit applying a  $3.5 \sigma$  cut and including the borders of the histogram are summarized in figure 28. At this stage also the statistical errors are incorporated.

---

be applied where  $\sigma = \frac{\sigma_{anode}}{\sqrt{(n)}}$  with  $n = \text{number of anodes}$ .

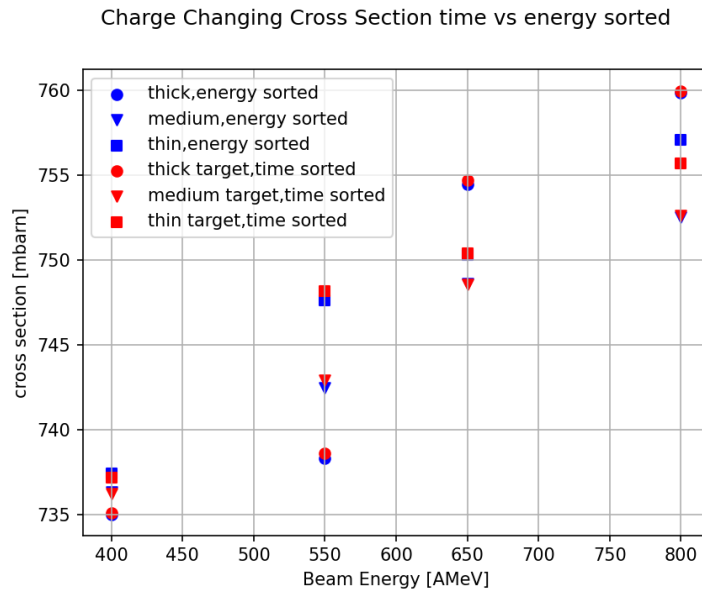


Figure 27: Comparison of charge changing cross section measurements when using time sorting algorithm(red) and energy sorting algorithm(blue) for multi-hit anodes.

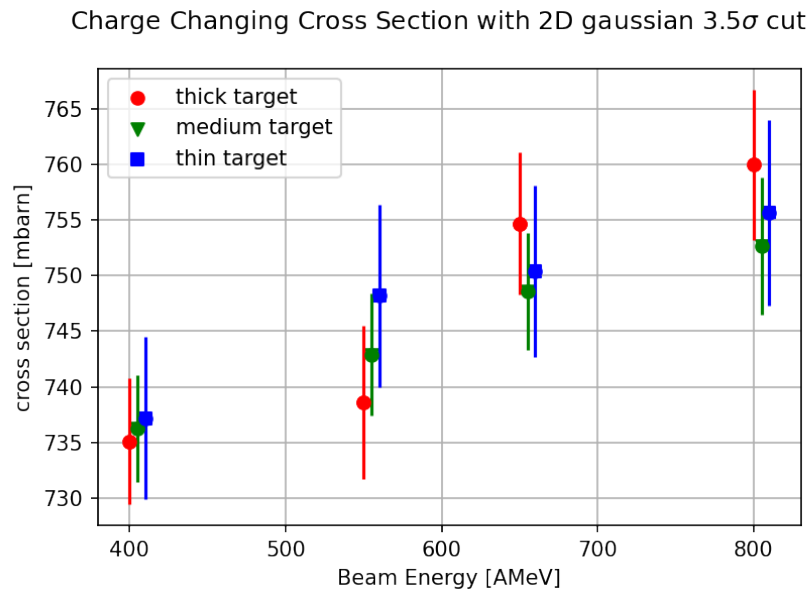


Figure 28: Measurement of charge changing cross sections using all 16 anodes of the TWIN MUSIC applying the 2D gaussian fit and considering the borders as in figure 21.

## 4.4 Geometric Corrections

For the S444 experiment only section 1 (right down) of the TWIN MUSIC, which was centered on the beam spot, was operated. As consequence full geometric efficiency could not be assumed. To visualize the restricted geometric efficiency of the TWIN MUSIC the position in x and y (perpendicular plane to the beam direction) on the MWPC1 in front of the ionisation chamber was plotted, once without any conditions on the TWIN MUSIC and once with the condition of having identified a carbon isotope (with the 2D gauss-fit method as described in chapter 4.3.3), see figure 29. The large active surface area of  $200 \times 200 \text{ mm}^2$  of the MWPC1 affirms that all the carbon fragments are detected<sup>27</sup> whereas the TWIN MUSIC behind it, with an active surface of  $55 \times 110 \text{ mm}^2$  (section 1), is not sensitive to the scattered fragments with large deflection angle.

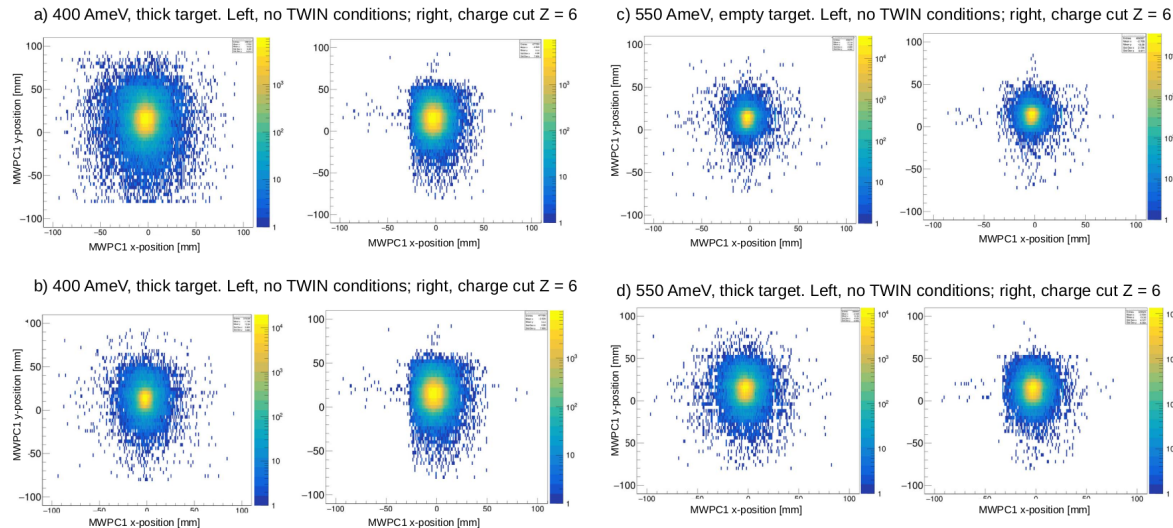


Figure 29: Distribution in x and y on MWPC1 for different energies with and without target. TODO: subplot b) wrong naming,it's the empty run 400 AMeV.

The efficiency loss depends on the target thickness - for thicker targets the geometric distribution of the fragments is broader and therefore the efficiency loss larger - and the beam energies - for larger beam energies the scattering angles decrease due to the boost effects, the efficiency loss gets smaller. This means, that the efficiency loss needs to be compensated runwise. These efficiency effects can be observed in figure 29.

To compensate correctly for the geometric efficiency it has to be considered that for the charge changing cross section measurement only the carbon isotopes after the target are counted in the TWIN MUSIC. Therefore the correction should only be applied to

<sup>27</sup>This statement does not hold for light fragments as protons or deuterons. Their deflection angle exceeds the geometric acceptance of the MWPC1.

the carbon isotopes ( $Z = 6$ ) on the x-y distribution on the MWPC1, see figure 29. The geometric efficiency correction is done graphically on the x-y distribution of the MWPC1 for carbon isotopes by following procedure:

### 1. Correction for the x-position distribution:

- (a) First fit x-distribution with double-gaussian function with five free parameters and common mean value  $\mu_x$

$$f(x) = A \cdot \exp\left(-\frac{(x - \mu_x)^2}{a^2}\right) + B \cdot \exp\left(-\frac{(x - \mu_x)^2}{b^2}\right) \quad (20)$$

- (b) Fit again within range  $\mu_x \pm \epsilon_x$ . The parameter  $\epsilon_x$  is fixed by educated guess, TODO. As  $\mu_x$  take the value from the fit in the previous step. A fit for the central region of the x-distribution is obtained,

$$f(x)_{central}(A_{central}, a_{central}, B_{central}, b_{central}, \mu_{central}).$$

- (c) The obtained fit function  $f(x)_{central}$  is then used to compare with the data distribution( $f(x)_{data}$ ) in the border regions  $[-100, \mu_{central} - \epsilon_x]$  and  $[\mu_{central} + \epsilon_x, 100]$ . Since only the left border region (low x-positions) is affected by the limited geometric acceptance, the right border region can be used for correction:

$$\Delta_{xcorr} = \int_{\mu_{central} + \epsilon_x}^{100} f(x)_{data} - f(x)_{central} - \int_{-100}^{\mu_{central} - \epsilon_x} f(x)_{data} - f(x)_{central} \quad (21)$$

### 2. Correction for the y-position distribution:

- (a) First fit y-distribution with double-gaussian function with five free parameters and common mean value  $\mu_y$

$$f(y)_{fit} = C \cdot \exp\left(-\frac{(y - \mu_y)^2}{c^2}\right) + D \cdot \exp\left(-\frac{(y - \mu_y)^2}{d^2}\right) \quad (22)$$

- (b) The obtained fit function  $f(y)$  is then used to compare the data distribution( $f(y)_{data}$ ) in the border regions  $[-100, \mu_y - \epsilon_y]$  and  $[\mu_y + \epsilon_y, 100]$ . The parameter  $\epsilon_y$  is fixed by educated guess, TODO. As  $\mu_y$  take the value from the fit in the previous step. Same as for the x-correction both border regions are compared. The high border region (high y-positions) affected by the limited geometric acceptance while the low border region (low y-positions) has full geometric acceptance.

$$\Delta_{ycorr} = \int_{-100}^{\mu_{central} - \epsilon_y} f(y)_{data} - f(y)_{fit} - \int_{\mu_y + \epsilon_y}^{100} f(y)_{data} - f(y)_{fit} \quad (23)$$

3. To correct the number of survived carbon isotopes  $N_2 = N_{carbon}$  both corrections in x and y are applied<sup>28</sup>

$$N_2^{corr} = N_2 + \frac{\Delta_{xcorr} + \Delta_{ycorr}}{N_2} \quad (24)$$

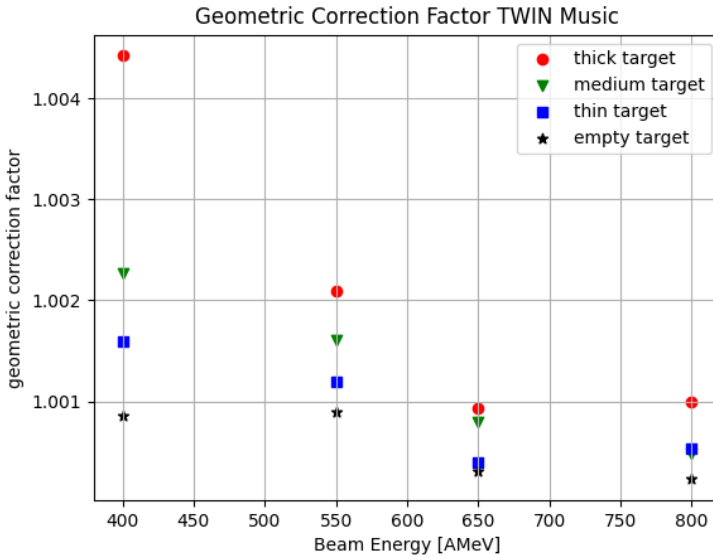


Figure 30: Geometric correction factors from limited geometric efficiency of TWIN MUSIC.

Figure 30 summarizes the geometric correction factors  $\epsilon_{geo\_corr}$  obtained from the graphical reconstruction of missed TWIN MUSIC events as described above. The correction factor is subsequently applied to the charge-changing cross-section, resulting in the final corrected charge-changing cross-section:

$$\sigma_{geo\_corr} = -\frac{1}{N_t} \ln\left(\frac{N_1^E N_2}{N_2^E N_1} \cdot \epsilon_{geo\_corr}\right) = -\frac{1}{N_t} \left( \ln\left(\frac{N_1^E N_2}{N_2^E N_1}\right) + \ln(\epsilon_{geo\_corr}) \right) \quad (25)$$

Figure 31 shows the measured charge changing cross section once without considering the the limited geometric acceptance of the TWIM MUSIC and once applying the geometric correction factors as presented in equation 25. As expected significantly affected by the geometric correction are runs with 400 and 550 AMeV beam energy whereas at beam energies of 650 and 800 AMeV the effect is exceptionally small since at high beam energies the fragments after the target preceive a strong boost effect in beam direction which constrains the distribution in the x-y-plane.

---

<sup>28</sup>Under the assumption that x and y are uncorrelated where the x-y distribution on the MWPC1 is given by  $f(x,y) = f(x) \cdot f(y)$ .

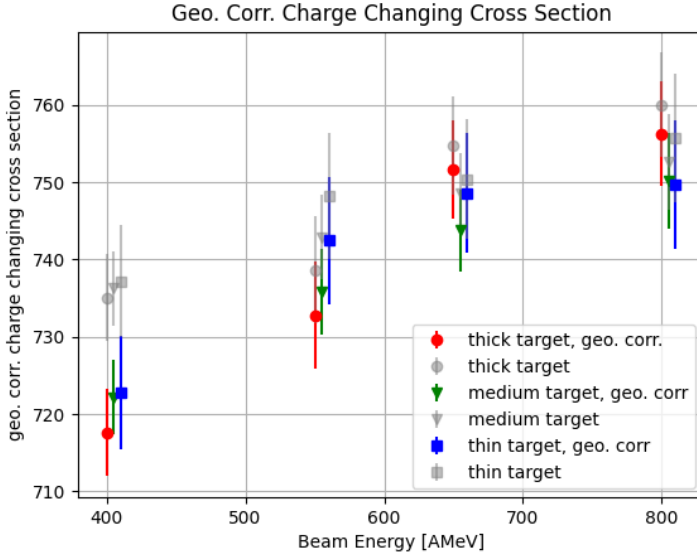


Figure 31: Charge changing cross section with applied geometry corrections. In gray: charge changing cross section measurements before applying corrections, as in figure 26.

## 4.5 Isotope Correction - Total Interaction Cross Section

The general formulation for the calculation of cross sections in equation 15 can be used to determine the cross section for specific channels depending on the definition of  $N_2$ . In the previous subsection 4.3 where the charge changing cross section was measured,  $N_2$  had to be sensitive to the charge of the outgoing fragment. Therefore  $N_2$  was defined as the number of survived carbon isotopes, i.e.  $N_2 = N_2^{Z=6}$ . For the measurement of the total interaction cross section  $N_2$  has to be sensitive to both proton and neutron number of the fragments.  $N_2$  is therefore restricted to the number of survived  $^{12}\text{C}$  isotopes, i.e.  $N_2 = N_2^{^{12}\text{C}}$ . Since  $N_2^{^{12}\text{C}}$  is a subset of  $N_2^{Z=6}$ ,  $N_2^{^{12}\text{C}}$  can be determined by identifying and disentangling the number of survived  $^{12}\text{C}$  isotopes from the set of events with carbon isotopes  $N_2^{Z=6}$ . For that reason the positional correlations on the x-coordinate of MWPC2 (upstream to GLAD) and the MWPC3 (downstream to GLAD) are exploited. The GLAD magnet, which acts as a mass spectrometer, deflects the passing through fragment. Depending on its proton to neutron ratio the fragment is deflected more or less, described by the formula for magnetic rigidity:

$$B \cdot \rho = \frac{\gamma \cdot m \cdot v}{q} \quad (26)$$

where:

- $B$  is the strength of the magnetic field,
- $\rho$  is the radius of curvature of the particle's trajectory,
- $\gamma$  is the Lorentz factor,
- $v$  is the velocity of the particle,
- $m$  is its mass,
- $q$  is its charge.

Figure 33 shows the x distribution on MWPC2 versus MWPC3 for the thick target run at a beam energy of 400 AMeV. The main diagonal line corresponds to the  $^{12}\text{C}$  isotopes. From all isotopes they have the largest mass to proton ratio ( $n+p/p$ ) and are therefore less deflected by the magnetic field of GLAD. The less prominent line below corresponds to  $^{11}\text{C}$  isotopes and on the lower edge few events with  $^{10}\text{C}$  are visible. To identify the number of survived  $^{12}\text{C}$  fragments a graphical selection of the  $^{12}\text{C}$  isotopes - the main diagonal line - is applied.

#### Graphical Selection Algorithm:

- Fit the main diagonal line, which corresponds to the  $^{12}\text{C}$  isotopes, with a linear fit function  $f(x_{mw2}) = a \cdot x_{mw2} + b$ .
- To get the most accurate intersection line between  $^{12}\text{C}$  isotopes and all lighter carbon isotopes the linear fit function from the previous step is taken as starting point. Iteratively the offset value  $b$  is reduced by  $b_i = b_{i-1} - 1$ . For all iteration steps the ratio  $r_{^{12}\text{C}(i)}$  of hits below the linear fit function and the total number of hits in the histogram is calculated.
- The derivative  $\frac{dr_{^{12}\text{C}}(i)}{db_i}$  is calculated.
- Finally the offset  $b_i$  with the largest value for  $\frac{dr_{^{12}\text{C}}(i)}{db_i}$  is selected as cutting line between  $^{12}\text{C}$  isotopes and  $^{11}\text{C}/^{10}\text{C}$  isotopes<sup>29</sup>.

The ratio  $r_{^{12}\text{C}}$  is unaffected by detector efficiencies of MWPC2 and MWPC3<sup>30</sup> and therefore the ratio  $r_{^{12}\text{C}}$  can be applied directly as isotope correction to calculate the total interaction cross section:

$$\sigma_I = \sigma_{geo\_corr} + \sigma_{iso}$$

With the isotope correction cross section  $\sigma_{iso}$ :

$$\sigma_{iso} = -\frac{1}{N_t} \ln(r_{^{12}\text{C}})$$

---

<sup>29</sup>For empty target runs the offset  $b$  is manually selected

<sup>30</sup>Under the assumption of constant efficiency over  $x_{mw2}$  and  $x_{mw3}$

To calculate the isotope correction cross section six different methods were employed and compared with each other:

- **MWPC2 and MWPC3 hit-level data:**

For all MWPCs the standard *cal-to-hit* step sorts the calibrated hits in the detector according to the calibrated charge deposited in the pads. The final position (in mm) is determined by selecting the hit with the highest charge deposition  $Q_{max}$  and its left ( $Q_L$ ) and right neighbour ( $Q_R$ ) pads<sup>31</sup>. These charge and position values are inserted in the "hyperbolic squared secant" function [55] with the following charge distribution function:

$$Q(x) = \frac{a_1}{\cosh^2\left(\frac{\pi(x-a_2)}{a_3}\right)}$$

where  $a_1$  is the amplitude of the distribution  $Q_{max}$ ,  $a_2$  its centroid, and  $a_3$  derives as follows:

$$a_3 = \frac{\pi\omega}{\cosh^{-1}\left(0.5 \times \left(\sqrt{\frac{Q_{max}}{Q_L}} + \sqrt{\frac{Q_{max}}{Q_R}}\right)\right)}$$

$\omega$  being the width of the pads. The centroid of the distribution, which is used as final hit position in the *hit-data* level, can be deduced from:

$$a_2 = \frac{a_3}{\pi} \times \tanh^{-1}\left(\frac{\sqrt{\frac{Q_{max}}{Q_L}} - \sqrt{\frac{Q_{max}}{Q_R}}}{2 \sinh\left(\frac{\pi\omega}{a_3}\right)}\right)$$

Figure 32 shows the "hyperbolic squared secant" function with the inserted values for  $Q_{max}$ ,  $Q_R$  and  $Q_L$ . The "hyperbolic squared secant" function is used to determine the x hit position as well as the y hit position for all MWPCs. Figure 33 shows the  $x_{mw2}$  versus  $x_{mw3}$  distribution of carbon isotopes for the 400 AMeV run with the thick target. The two correlated lines corresponding to the  $^{12}\text{C}$  and  $^{11}\text{C}$  isotopes can clearly be distinguished. The vertical line can be interpreted as amount of events where the incoming centered carbon fragment gets scattered by air or the detector material in place between MWPC2 and MWPC3. The horizontal wide spread line has no physical interpretation and can rather be explained by the *cal-to-hit* step in MWPC2: For events where there is not a spatially constrained hit cluster but sparse hits the hyperbolic squared secant function may pick the wrong  $Q_{max}$  and therefore wrongly reconstructs the x position in MWPC2.

- **MWPC2 and MWPC3 data with own "hit-clustering" level:**

To overcome the issue with potentially wrong x-position reconstruction in the

---

<sup>31</sup>In case no charge deposition in one or both neighbours the charge value is set to 1 respectively.

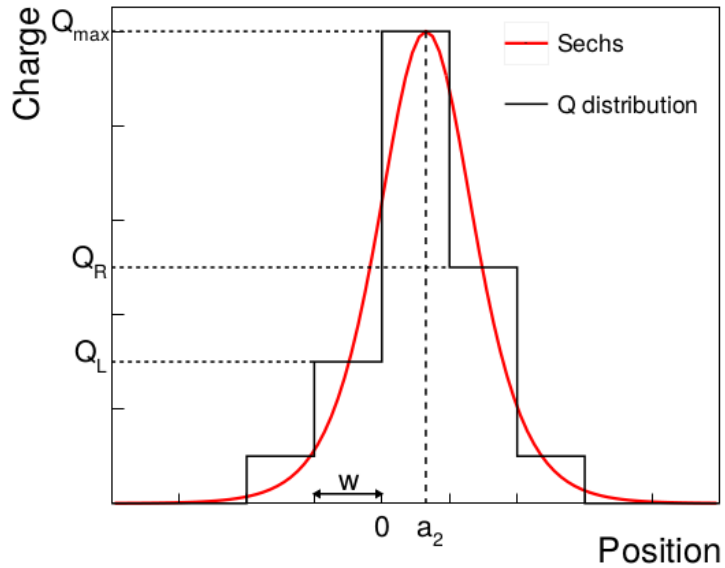


Figure 32: Figure taken from [33], with  $w$  being the width of the cathode pads of the MWPC and  $a_2$  the final position value of the hit determined by the hyperbolic squared function (in red). In black the measured charge deposition distribution in the MWPC.

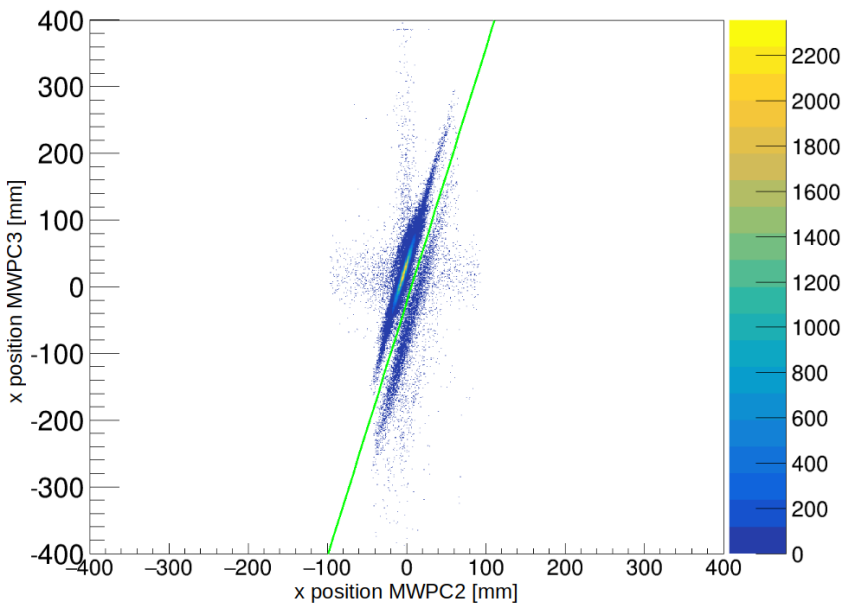
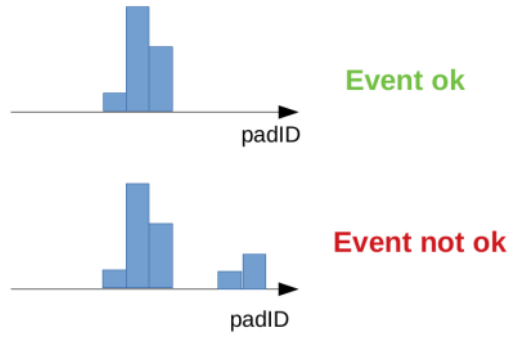


Figure 33: Distribution of  $x$  in MWPC2 and MWPC3 for the 400 AMeV run with thick target. The green line corresponds to the intersection line between  $^{12}\text{C}$  and  $^{11}\text{C}/^{10}\text{C}$  isotopes fixed on the graphical selection algorithm.

Figure 34: Restricted event selection for MWPC2 and MWPC3: only events with one single coherent (i.e. without any holes) cluster are accepted.



MWPCs the event selection on MWPC2 and MWPC3 was restricted to events where both MWPC2 and MWPC3 have only one spatially constrained cluster (see figure 34) to avoid ambiguities in the position determination. This method strongly retains uncorrelated hits in MWPC2 and MWPC3.

Figure 35 shows the distribution of  $x$  in MWPC2 and MWPC3 using the own hit-clustering reconstruction. This reconstruction method removes the uncorrelated horizontal line which was observed in figure 33. However the statistics are reduced by  $\approx 35\%$ <sup>32</sup>.

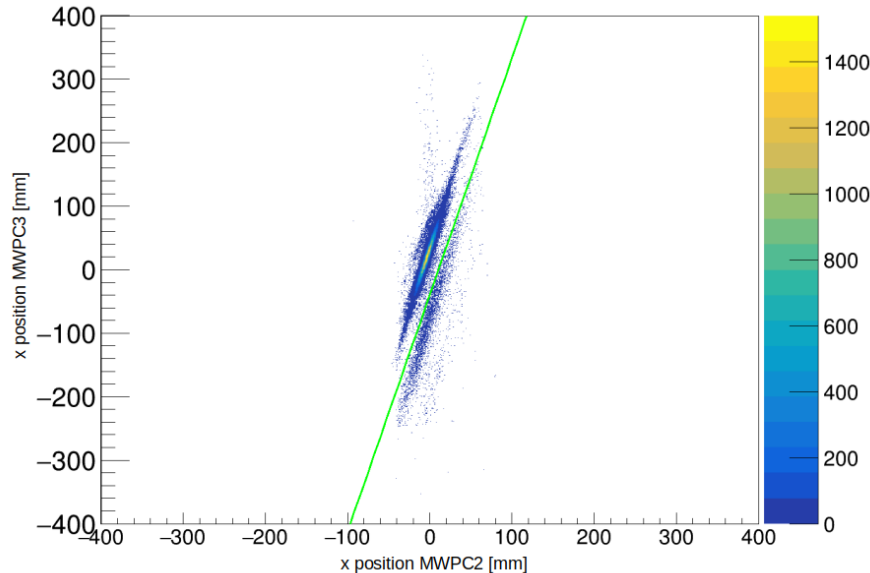


Figure 35: Distribution of  $x$  in MWPC2 and MWPC3 using the own hit clustering reconstruction. Thick target run, beam energy 400 AMeV. The green line corresponds to the intersection line between  $^{12}\text{C}$  and  $^{11}\text{C}/^{10}\text{C}$  isotopes fixed on the graphical selection algorithm.

---

<sup>32</sup>Number of entries in the 2D plot for default reconstruction method: 533816, for the own hit clustering reconstruction: 346315 for the 400 AMeV run with thick target.

- **MWPC1 and MWPC3 hit-level data:**

To get the ratio  $r_{12\text{C}}$  it is necessary to correlate the x positon before and after the GLAD magnet. This task can be completed by MWPC3 with respect to MWPC2 or MWPC1. Since the MWPC1 is upstream to MWPC2 the positional distribution of the carbon fragments narrower which as consequence makes it more difficult to disentangle  $^{12}\text{C}$  and  $^{11}\text{C}/^{10}\text{C}$  isotopes, see figure 36. Moreover MWPC1 had two noisy pads which distorts the distribution when using the standard *cal-to-hit* step to get the position value, see figure 36.

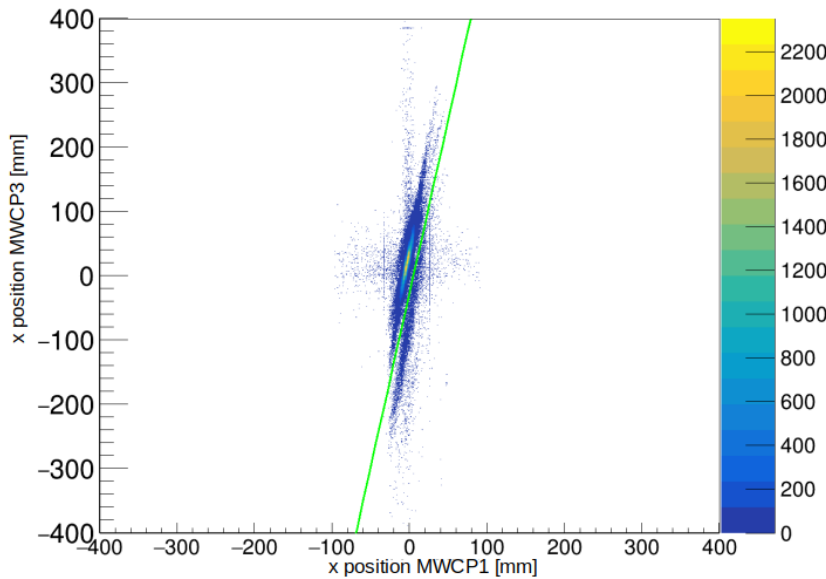


Figure 36: Distribution of x in MWPC1 and MWPC3. Thick target run, beam energy 400 AMeV. The two vertical lines stem from two noisy pads in MWPC1.

- **MWPC1 and MWPC3 data with own "hit-clustering" level:**

Again, to overcome the issue with potentially wrong x-position reconstruction in the MWPCs the own hit clustering reconstruction method, as described above, was applied to MWPC1 and MWPC3 resulting in the 2D plot 37.

- **MWPC2 and MWPC3 with own clustering, quadrant selection in MWPC2:<sup>33</sup>**

The limited geometric acceptance of TWIN MUSIC, described in section 4.4, affects the isotope correction too. The x distribution on the MWPC1/2/3 is cut off on the lower end and the y distribution on the higher end, see figure 29. The  $^{11}\text{C}/^{10}\text{C}$  isotopes are expected to have a broader x and y distribution. Missing the lower and higher edges in the x and y distribution respectively distorts the  $r_{12\text{C}}$  ratio towards higher values. This results in a lower cross section contribution

---

<sup>33</sup>I did the quadrant selection also in MWPC2, outcome really similar, TODO: add to appendix...

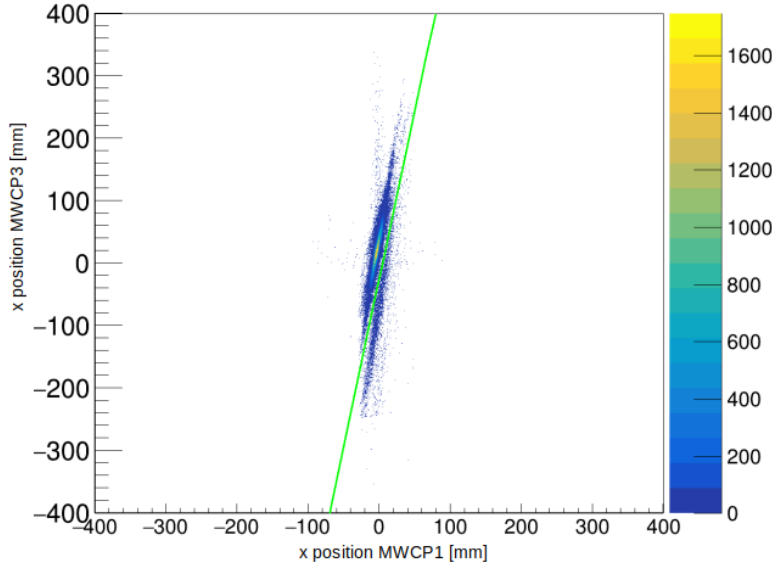


Figure 37: Distribution of x in MWPC1 and MWPC3 using the own hit clustering reconstruction. Thick target run, beam energy 400 AMeV.

of the isotope correction, especially for the low energy runs. To correct for this the x-y distribution in MWPC1 was split into four quadrants, see figure 38. The intersection lines were derived by the mean of the gaussian fit of the x and y distribution. The cross section contribution of the isotope correction was measured for all four quadrants.

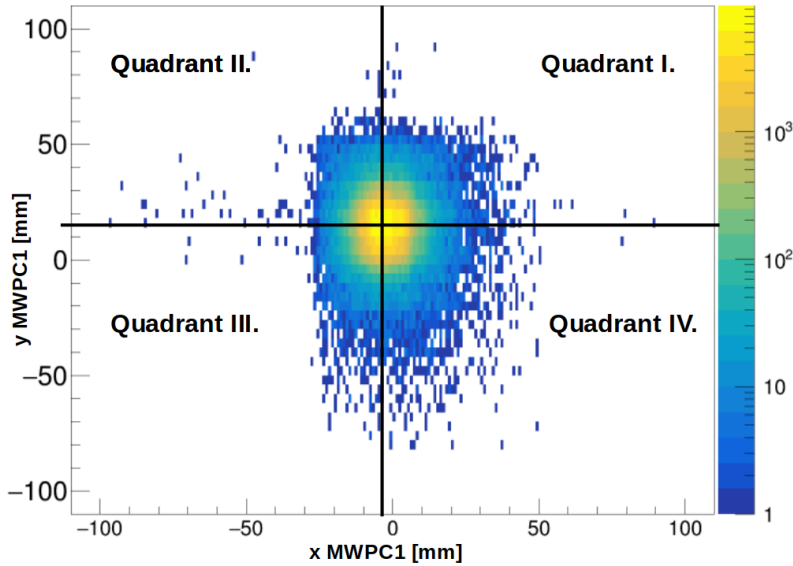


Figure 38: Distribution of x and y in MWPC1 split up in four quadrants. Thick target run, beam energy 400 AMeV.

#### 4.5.1 Results for Isotope Correction Methods

- MWPC2 and MWPC3 hit-level data:

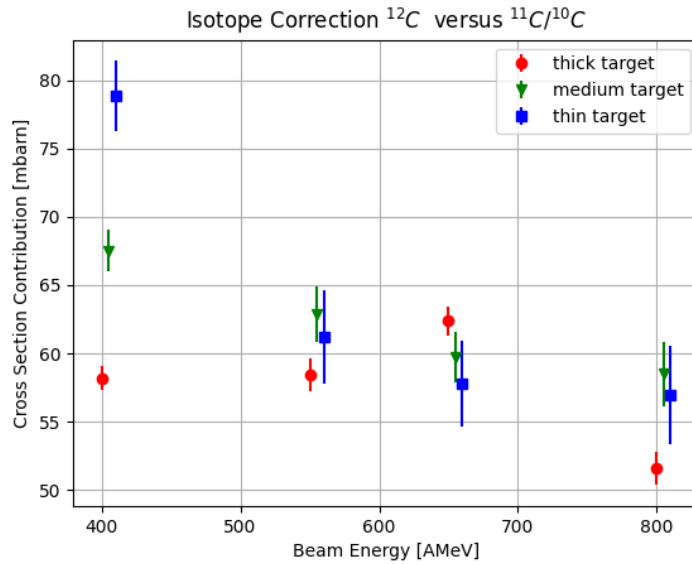


Figure 39: Isotope correction contribution to the total interaction cross section using standard hit level data in MWPC2 and MWPC3.

- MWPC2 and MWPC3 data with own "hit-clustering" level:

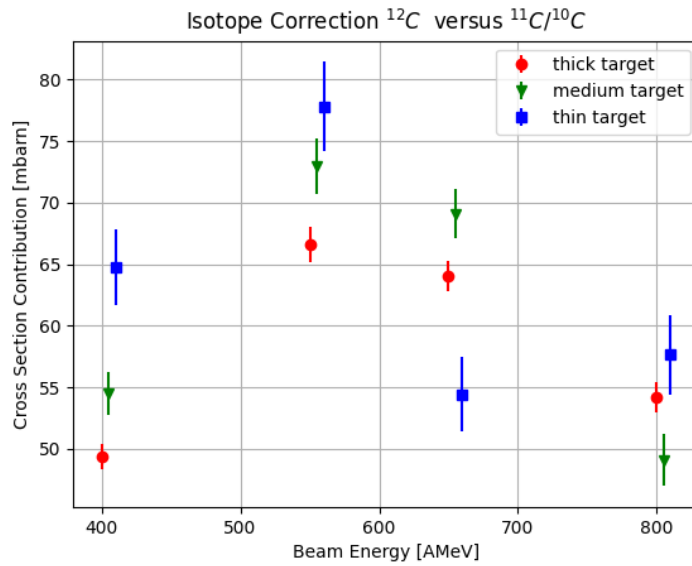


Figure 40: Isotope correction contribution to the total interaction cross section using own hit clustering in MWPC2 and MWPC3.

- MWPC1 and MWPC3 hit-level data:

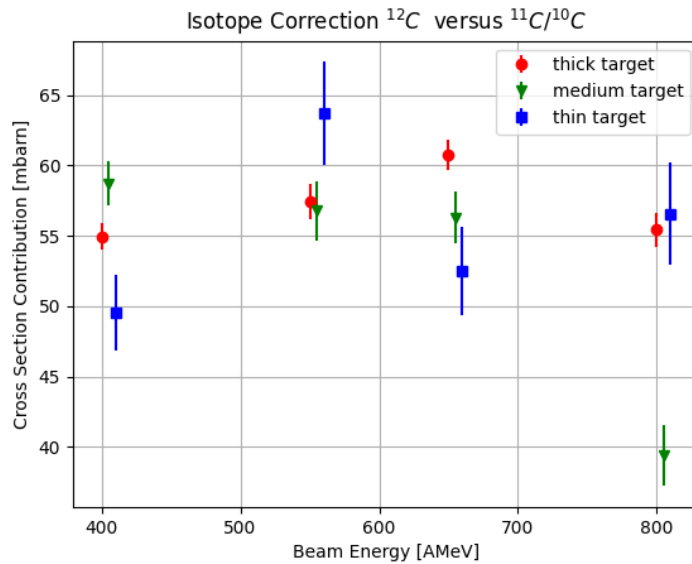


Figure 41: Isotope correction contribution to the total interaction cross section using standard hit level data in MWPC1 and MWPC3.

- MWPC1 and MWPC3 data with own "hit-clustering" level:

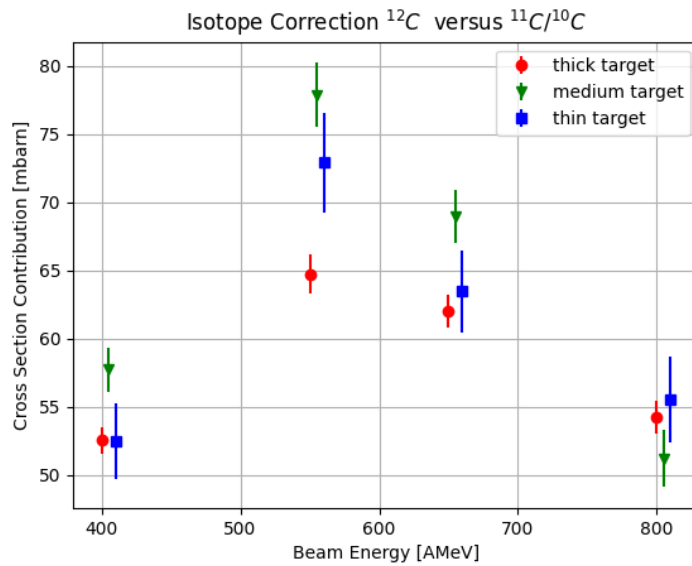


Figure 42: Isotope correction contribution to the total interaction cross section using own hit clustering in MWPC1 and MWPC3.

- MWPC2 and MWPC3 with own clustering, quadrant selection in MWPC1:

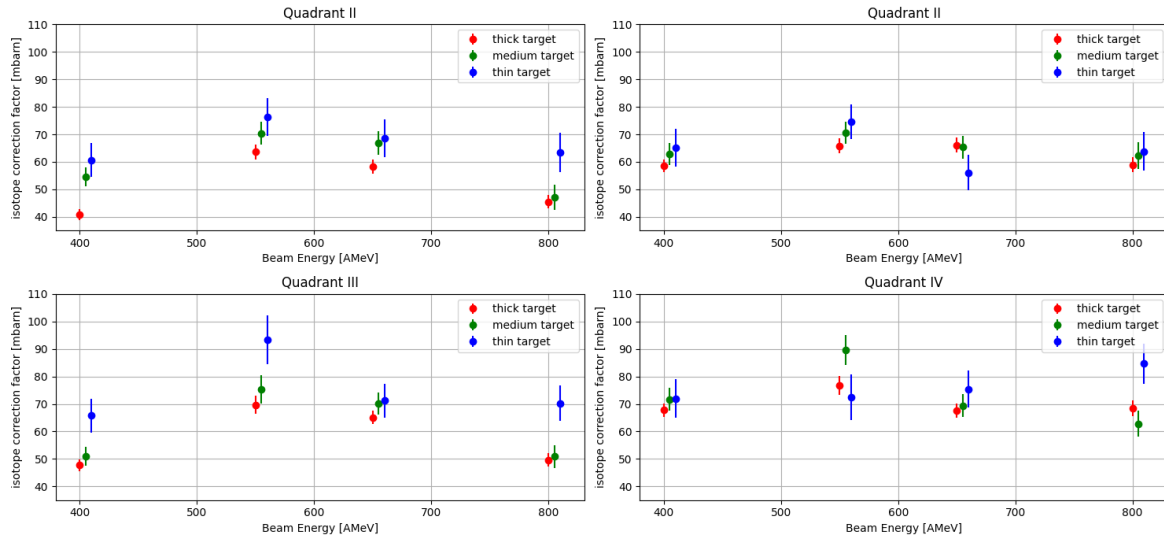


Figure 43: Isotope correction contribution to the total interaction cross section using own hit clustering in MWPC2 and MWPC3. Comparison for different quadrant selection in MWPC1. Quadrant four is the preferred one as it is not affected by limited geometric acceptance of TWIN MUSIC.

## 4.6 Statistical and Systematic Error Analysis

All three measurements presented in this section, the charge changing cross section, the isotopic cross section correction cross section and the total interaction cross section, rely on the transmission method and the error analysis of those measurements are treated the same accordingly. The generic formula for all three measurements was presented in section 4.1, equation 14.

Since all quantities in equation 14 are mutually independent, the gaussian error propagation for statistical and systematical uncertainties is given by:

$$\Delta_{stat./syst.} = \sqrt{\sum_{i=1}^n \left( \frac{\partial f}{\partial x_i} \cdot \Delta_{x_i} \right)^2} \quad (27)$$

with:

$f(x_1, x_2, \dots, x_n)$  the error prone cross section function,

$x_i$  the independent variables ( $N_1, N_2, N_t$ ; see equation 14),

$\Delta_{x_i}$  stat./syst. uncertainties associated to independent variable  $x_i$

#### 4.6.1 Statistical Uncertainties

For the charge changing cross section the combined statistical error is:

$$\Delta\sigma_{\text{stat.}|cc} = \sqrt{\left(\frac{\partial\sigma_{cc}}{\partial N_t}\Delta N_t\right)^2 + \left(\frac{\partial\sigma_{cc}}{\partial P_{\text{surv}|cc}}\Delta P_{\text{surv}|cc}\right)^2 + \left(\frac{\partial\sigma_{cc}}{\partial P_{\text{surv}|cc}^E}\Delta P_{\text{surv}|cc}^E\right)^2} \quad (28)$$

where  $\Delta N_t$  accounts for the uncertainty in the measurement of the target thickness.  $P_{\text{surv}|cc}$ , the surviving probability of having a carbon isotpe in the final state, follows a binomial distribution with  $N_1$  independent experiments and a boolean valued reaction output (survived vs. non-survived). Therefore  $P_{\text{surv}|cc}$  follows the standard error of binomial distributed variable:

$$\Delta P_{\text{surv}|cc}^{(E)} = \sqrt{\frac{P_{\text{surv}|cc}^{(E)} \cdot (1 - P_{\text{surv}|cc}^{(E)})}{N_1^{(E)}}} \quad (29)$$

Inserting in equation 28 gives:

$$\Delta\sigma_{\text{stat.}|cc} = \sqrt{\left(\frac{\sigma_{cc}\Delta N_t}{N_t}\right)^2 + \frac{1}{N_t^2} \left(\frac{1 - P_{\text{surv}|cc}}{P_{\text{surv}|cc}N_1} + \frac{1 - P_{\text{surv}|cc}^{(E)}}{P_{\text{surv}|cc}^{(E)}N_1^E}\right)} \quad (30)$$

Similar for the isotopic correction cross section with  $P_{\text{surv}|iso}$  the ratio of reconstructed  $^{12}C$  isotopes to all identified carbon isotopes in the x-position correlation plots for MWPC2 and MWPC3:

$$\Delta\sigma_{\text{stat.}|iso} = \sqrt{\left(\frac{\sigma_{iso}\Delta N_t}{N_t}\right)^2 + \frac{1}{N_t^2} \left(\frac{1 - P_{\text{surv}|iso}}{P_{\text{surv}|iso}N_1} + \frac{1 - P_{\text{surv}|iso}^{(E)}}{P_{\text{surv}|iso}^{(E)}N_1^E}\right)} \quad (31)$$

For viewing the statistical uncertainties of the total interaction cross section measuerments the uncertainties in the target thickness as well as the uncertainties of the carbon isotope surviving probability  $P_{\text{surv}|cc}$  and the  $^{12}C$  surviving probability  $P_{\text{surv}|iso}$  have to be accounted for:

$$\Delta\sigma_{\text{stat.}|tot} = \sqrt{\left(\frac{\sigma_{tot}\Delta N_t}{N_t}\right)^2 + \frac{1}{N_t^2} \left(\frac{1 - P_{\text{surv}|cc}}{P_{\text{surv}|cc}N_1} + \frac{1 - P_{\text{surv}|cc}^{(E)}}{P_{\text{surv}|cc}^{(E)}N_1^E}\right) + \frac{1}{N_t^2} \left(\frac{1 - P_{\text{surv}|iso}}{P_{\text{surv}|iso}N_1} + \frac{1 - P_{\text{surv}|iso}^{(E)}}{P_{\text{surv}|iso}^{(E)}N_1^E}\right)} \quad (32)$$

#### 4.6.2 Systematic Uncertainties

### 4.7 (Preliminary) Results Total Interaction Cross Section

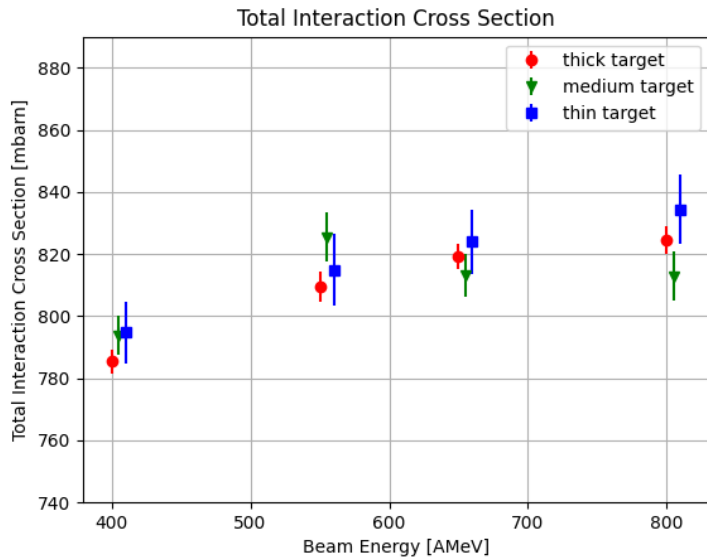


Figure 44: Total interaction cross section using the quadrant IV. selection in MWPC1 x-y plot (see figure 38) for the isotope correction and applying the geometric correction on the charge changing cross section.

## 5 Qualitative Analysis - Quasi-Free Scattering $^{12}\text{C}(\text{p},2\text{p})^{11}\text{B}$

Until the S444 experiment in 2020 CALIFA consisted out of a prototype frame filled with up to 64 CsI(Tl) crystals. The geometric coverage was therefore limited. For the S444 experiment CALIFA got its final frame and was fully filled in the forward barrel and 35%filled in the iPhos region, CEPA was not installed yet. With these improvements it was possible to commission QFS-experiments with CALIFA at  $\text{R}^3\text{B}$ . In the follow up experiment S467, also in 2020, the first experimental run to study single-particle structures of neutron-rich Ca isotopes via QFS reactions was carried out.

Even though great improvements in the detector development were achieved the correction factors to correct for geometric acceptance would be much too high ( $\approx 10$ ) for precise cross section measurements for QFS-reactions since the correction factors would in turn rely on a simplified reaction model. A precise analysis of the acceptance correction factor and the development of a more sophisticated and data driven reaction model is out of the scope of this work. Therefore this analysis focusses on the methods of QFS-reaction identification and the extraction of the key informations dicussed in section 2.5. TODO: add more stuff here...

### 5.1 Setup-Calibration

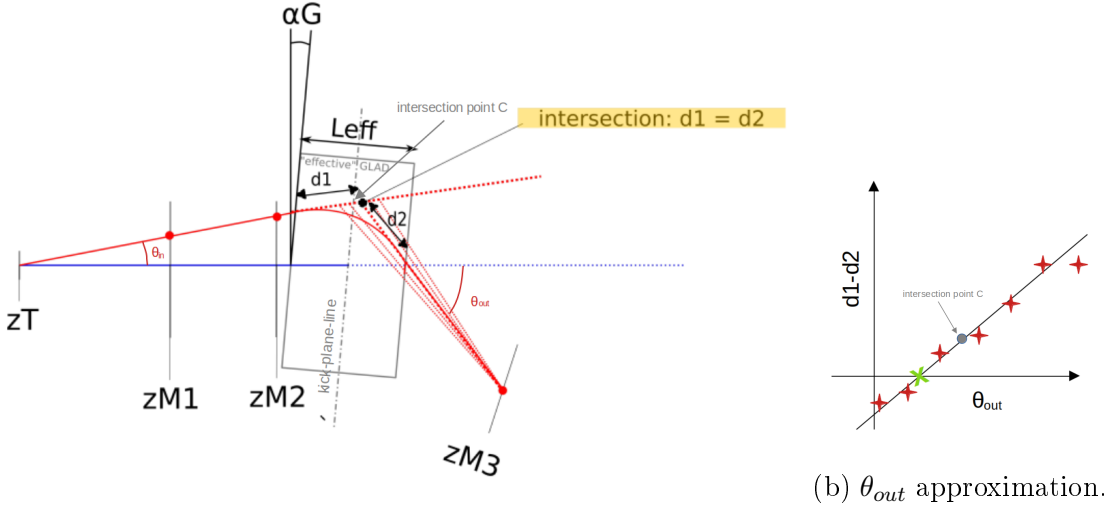
For setup description refer to section 4. For all detectors except the SOFIA (Study On FIission with Aladin) Time of Flight Wall the calibration parameters investigated by the respective detector-expert group were adopted. Herefore we will subsequently only describe the Time of Flight Wall calibration in this subsection.

#### 5.1.1 Flight-Path Reconstruction

The procedure to calibrate the Time of Flight (ToF) Wall involves beforehand a precise flight-path reconstruction of the projectile from the entrance of Cave C downstream to the ToF Wall. Since only one tracking detector downstream to GLAD was in operation for the S444 experiment no angle of the deflected fragment/beam  $\theta_{out}$  could be directly extracted. Herefore an advanced tracking algorithm was developed, motivated from ref. [56] (section 3.4).

- The first step is to measure the scattering angle after target,  $\theta_{in}$ , and draw an extended line from the target position through the effective magnetic field of GLAD.

- Draw a trajectory line from the hit position in MWPC3 to the intersection point C (see figure 45a) of the "kick-plane-line" and the reconstructed and extended track line upstream to GLAD.
- Now sweep along the reconstructed track line upstream to GLAD. For each step a value for  $\theta_{out}$  and  $d1 - d2$  is gathered, see figure 45b.
- As in figure 45b shown, fit the data-points from previous step with a linear fit function and find the corresponding  $\theta_{out}$  value where the fit line intersects with the abscissa. This corresponds to the case where  $d1 = d2$ . This is the approximated "kickpoint" in GLAD.
- Previous steps need to be executed for all events accordingly.



(a) Flighpath reconstruction with "Leff" being the effective active width of the magnetic field of GLAD For detailed information see text.

Figure 45: Flighpath tracking and reconstruction of the fragment/beam after the target.

Now that the scattering angle after the target  $\theta_{in}$  and the angle after GLAD,  $\theta_{out}$  is known and the position outside the magnetic field of GLAD are fixed, with  $(z_1, x_1)$  the entrance point on the GLAD field and  $(z_2, x_2)$  the exit point, the bending radius  $r$  from the magnetic deflection can be determined:

$$r = \frac{L_{eff}}{2 \cdot \sin\left(\frac{\theta_{in} + \theta_{out}}{2}\right) \cdot \cos\delta} \quad (33)$$

where  $L_{eff}$  is the effective active width of the magnetic field of GLAD, which corresponds  $\approx 2.06\text{ m}$ . This value could also be verified by extracting  $L_{eff}$  from the formula for

the magnetic rigidity  $B \cdot r = \gamma\beta m/q$  for empty target runs with known values of the B-field<sup>34</sup>.

The angle  $\delta$  in equation 33 is given by the trajectory line going through  $(z_1, x_1)/(z_2, x_2)$  and the line parallel to the GLAD magnet width  $L_{eff}$ .

A detailed derivation of equation 33 can be found in appendix B. The arc trajectory  $l_{GLAD}$  of the fragment within GLAD can be reconstructed using the bending radius  $r$  and the entry and exit points  $(z_1, x_1)/(z_2, x_2)$ :

$$l_{GLAD} = r \cdot \omega \quad \text{with} \quad \omega = 2 \cdot \arcsin(t_{1/2}(2 \cdot r)) \quad (34)$$

where  $\omega$  is the central angle and  $t_{1/2}$  is the cord length between  $(z_1, x_1)$  and  $(z_2, x_2)$ .

At this stage the full pathlength  $L$  from the Start detector to the ToFW is fixed:

**From Start to the target  $l_{ST}$ :** For this path section a straight flightpath parallel to the z-coordinate is assumed. The pathlength is taken from the position measurements of the Start detector and the target accordingly ( $= 118.3\text{ cm}$ ).

**Target to GLAD entrance point  $(z_1, x_1)$ ,  $l_{in}$ :** For the exact position assignment of  $(z_1, x_1)$  both MWPC1 and MWPC2 position measurements have been calibrated with empty target runs by including an offset value in order to center the x-position in both detectors around zero. From the position measurement of the central position of GLAD, its tilting angle  $\alpha$  and  $L_{eff}$  the intersection point of the fragment trajectory before GLAD and the "effective GLAD magnetic field rectangle",  $(z_1, x_1)$ , can be determined and with it the according flightpath section  $l_{in}$ .

**Arc trajectory within GLAD,  $l_{GLAD}$ :** This flightpath passage is determined by reconstructing  $(z_1, x_1)$  and  $(z_2, x_2)$ , as it has been described in detail in the previous section. Hence the magnetic bending radius can be determined, see equation 33, and finally the arc trajectory  $l_{GLAD}$  as in equation 34.

**GLAD exit point  $(z_2, x_2)$  to ToFW,  $l_{out}$ :** The hit position  $(z_{MWPC3}, x_{MWPC3})$  in MWPC3 is given by the reconstructed hit position in this detector and the position measurement of the detector itself. The exit point  $(z_2, x_2)$  was reconstructed in the previous steps. Hence the trajectory line from  $(z_2, x_2)$  to  $(z_{MWPC3}, x_{MWPC3})$  is fixed and is expanded to the intersection with the ToFW plane for the concluding  $l_{out}$  measurement.

---

<sup>34</sup>For detector calibration, primarily for the ToFWall, we had several "empty sweep runs", with empty target and different B-field strength settings. Those runs were optimal to validate  $L_{eff}$ .

The resulting flightpath  $L$  recombines from:

$$L = l_{ST} + l_{in} + l_{GLAD} + l_{out}$$

In the flightpath reconstruction the deflections in the y-dimension were omitted as the angular straggling in the target is small (TODO: give sigma value) and since the deflection of the fragment within GLAD is independent from its y-position this contribution can be disregarded.

### 5.1.2 Time of Flight Calibration

For the time of flight measurement in the S444 setup the time is recorded and digitized by the VFTX, VME-FPGA Time-to-Digital Converter (TDC) Modules based on tapped delay line (TDL) TDCs[57]. These modules provide for each detected signal a coarse time, is determined by counting cycles of a 200 MHz readout clock, resulting in a 5 ns binning resolution, and a fine time, which is obtained using an FPGA-based Time-to-Digital Converter (TDC), which employs a tapped delay line (TDL). In this approach, the signal propagates through a series of delayed logic modules within the FPGA until the subsequent clock cycle terminates the sampling process. The number of delay elements traversed by the signal is used to compute the time difference between the signal onset and the end of the clock cycle. The translation of the resulting fine time, with reasonable assumption of an uniform distribution, is achieved via a calibrated linear function. This procedure assigns to each preamplifier signal in the start detector (left/right) and the ToF Wall (up/down) a calibrated raw time  $raw\_t$ :

$$raw\_t = coarse\_time\_clocks \cdot 5\text{ns} + offset[fine\_time]$$

Finally, the raw time of flight is reconstructed by combining all four time measurements:

$$RawTof = 0.5 * (raw\_t_{i,down} + raw\_t_{i,up}) - 0.5 * (raw\_t_{start,right} + raw\_t_{start,left}) \quad (35)$$

where  $i$  ( $\in 0 \dots 27$ ) refers to the scintillator number of the ToF Wall. Since the mentioned time measurements are standalone and not synchronized the  $RawTof$  has to be corrected by an offset which has to be determined again for each scintillator bar  $i$  of the ToF Wall:

$$\Delta_{ToF}[i] = \overline{L[i]} / v_{beam} - \overline{RawTof[i]}$$

where  $\overline{L[i]}$  is the mean reconstructed path length for all events in empty target runs which hit scintillator bar  $i$  of the ToF Wall. The beam velocity  $v_{beam}$  is directly taken

from the given beam settings, e.g. 400 AMeV beam, empty target corresponds to  $v_{beam} = 214,2 \text{ mm/ns}$ . The mean raw ToF  $\overline{\text{RawTof}[i]}$  again results from all events which hit scintillator bar  $i$  and is extracted from the mean value of a gaussian fit to the raw ToF. The resulting calibrated ToF can then be expressed as:

$$\text{ToF}[i] = 0.5 * (\text{raw\_}t_{i,down} + \text{raw\_}t_{i,up}) - 0.5 * (\text{raw\_}t_{start,right} + \text{raw\_}t_{start,left}) + \Delta_{\text{ToF}}[i]$$

To estimate the time of flight resolution for events with hit in ToF Wall bar  $i$  it has to be noted that the ToF is affected by the flight path. Hence the the time of flight should be written as:

$$\widetilde{\text{ToF}} = \frac{\overline{L[i]}}{\frac{L[i]}{\text{ToF}[i]}}$$

$\overline{L[i]}$  is the mean pathlength, whereas  $L[i]$  and  $\text{ToF}[i]$  are eventwise selected. By reconstructing the fligh-path as described in subsection 5.1.1 and employment of the mentioned time calibration steps the average time resolution  $\sigma_t$  results  $\approx 90 \text{ ps}$ <sup>35</sup>.

## 5.2 Event Selection

For the precise measurement of the total interaction cross section  $^{12}C + ^{12}C$ , as detailed in the section 4, event selection was of critical importance, requiring stringent cuts on the TPats (see table 5), as well as on the charge and position of the incoming particles. In contrast, for this qualitative QFS analysis, these factors played a minor role, allowing for only minimal cuts on the incoming ions:

- Both left and right preamplifiers of the start detector have seen a coincident signal.
- Exactly one hit in MWPC0 in the hit-level data.

However, for the identification of fragments downstream of the target, various detector signals and event parameters are required:

- One hit (in the hit-level data) in the MWPC tracking detectors, MWPC1 and MWPC2 upstream to GLAD, MWPC3 downstream to GLAD.
- Charge measurement in the TWIN-MUSIC.
- One hit scintillation bar in ToF Wall with signal from both up/down PMTs.

---

<sup>35</sup>To remove events with large angular straggling, a cut of  $\pm 20 \text{ mm}$  on the beam spot for the y-position on the MWPC3 was applied.

### 5.3 Fragment Identification

The first step for the identification of the QFS-reaction channel  $^{12}C(p, 2p)^{11}B$  is the identification of the fragment  $^{11}B$  via the formula for the magnetic rigidity:  $B \cdot r = \gamma\beta m/q$  where the  $\gamma$  factor accounts for the increase in momentum for relativistic particles. From the flightpath reconstruction and the ToF measurement as described in previous sections  $r, \beta$  and  $\gamma$  are obtained whereas the charge of the fragment  $q$  is measured by the energy loss ( $\Delta E \sim Z^2$ ) in the TWIN MUSIC detector.

The measured values for  $\frac{A}{q}$  and  $q$  are shown in figure 46 where the fragment of interest  $^{11}B$  is expected to be at  $\frac{A}{q} = 11/5 \approx 2.2$  and  $q = 5$ . The correlation plot exhibits a broad distribution in  $\frac{A}{q}$ , which may result from misidentification of hit positions in one of the MWPC tracking detectors when multiple signal hits occur. Even minor deviations in MWPC1 and MWPC2 can significantly affect the radius reconstruction, thereby impacting the accuracy of the  $\frac{A}{q}$  determination.

An intriguing feature is the distinct cluster observed at  $Z \approx 8.5$  and  $\frac{A}{q} \approx 2$ , which corresponds to pileup events. These occur when two ion signals arrive within a short time window in the TWIN MUSIC detector, preventing them from being resolved as separate events and instead being reconstructed as a single signal<sup>36</sup>. Moreover attention should be paid that it seems to be there a cut from analysis side at  $Z \approx 4$ . This is actually not the case. The TWIN MUSIC was optimized for the subsequent experimental run S467 with *Ca* isotopes and therefore the charge measurement was optimized for  $Z \approx 20$ . Everything below  $Z \approx 4$  was below the signal threshold of TWIN MUSIC.

Furthermore, it is important to note the apparent cut at  $Z \approx 4$  in the data. However, this is not an artifact of the analysis but rather a consequence of the experimental setup. The TWIN MUSIC detector was optimized for the subsequent S467 experiment, which focused on calcium isotopic chain ( $Z = 20$ ). As a result, the charge measurement was calibrated for  $Z \approx 20$ , and signals corresponding to  $Z \lesssim 4$  fell below the detection threshold of TWIN MUSIC.

For this qualitative analysis, the upper charge bound of  $^{11}B$  was determined by locating the intersection point of the Gaussian-fitted distributions corresponding to the  $Z = 5$  and  $Z = 6$  peaks. The lower bound was set by applying an offset of minus one unit.

A similar approach was employed to select the specific boron isotope  $^{11}B$ . The charge selection was performed using the previously defined boundary cuts. To isolate the  $^{11}B$  isotopes, the lower bound was determined by identifying the intersection point of

---

<sup>36</sup>For instance, if two carbon ions ( $Z = 6$ ) interact simultaneously, the total energy loss within TWIN MUSIC is approximately twice that of a single ion. Since the energy loss follows the relation  $\Delta E \sim Z^2$ , the reconstructed charge is given by  $\sqrt(2) Z_{carbon} \approx 8.5$ .

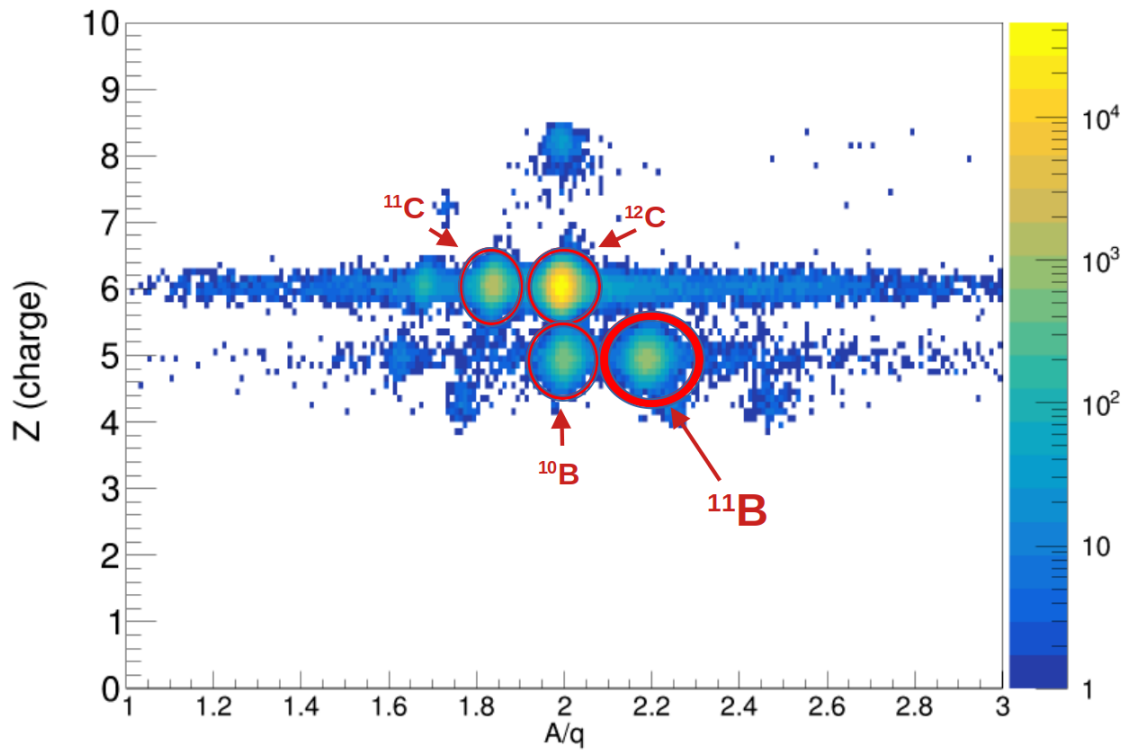


Figure 46: Fragment identification is performed using the correlation between the atomic number  $Z$  and the mass-to-charge ratio  $\frac{A}{q}$ . For the quasi-free scattering (QFS) analysis of the reaction  $^{12}C(p,2p)^{11}B$ , the fragment of interest is  $^{11}B$ , which is emphasized with a bold red circle.

the Gaussian-fitted distributions corresponding to the  $^{10}B$  and  $^{11}B$  peaks. The upper bound was established by measuring the distance from this intersection point to the peak of  $^{11}B$ .

## 5.4 QFS-Protons

Following the identification of the fragments through precise flight path reconstruction and time measurement, as detailed in the previous subsection, and the subsequent selection of the  $^{11}B$  isotope, the analysis focuses on the two correlated protons to fully characterize the quasi-free scattering channel  $^{12}C(p, 2p)^{11}B$ .

For a proper interpretation of the data, it is essential to consider the geometric acceptance of CALIFA during the S444 experiment in 2020. The central *BARREL* region (Ring 3 and Ring 4), covering the polar angular range from  $43^\circ$  to  $88^\circ$ , was fully operational. In contrast, the forward region, referred to as *iPhos* ( $19^\circ$  to  $43^\circ$ ), was only partially equipped, with a coverage of approximately 35%. The forward endcap, known as *CEPA*, was not installed, and the backward barrel remained unoccupied. The corresponding geometry is illustrated in figure 47.

For the proton selection and the application of reasonable cuts it is important to un-

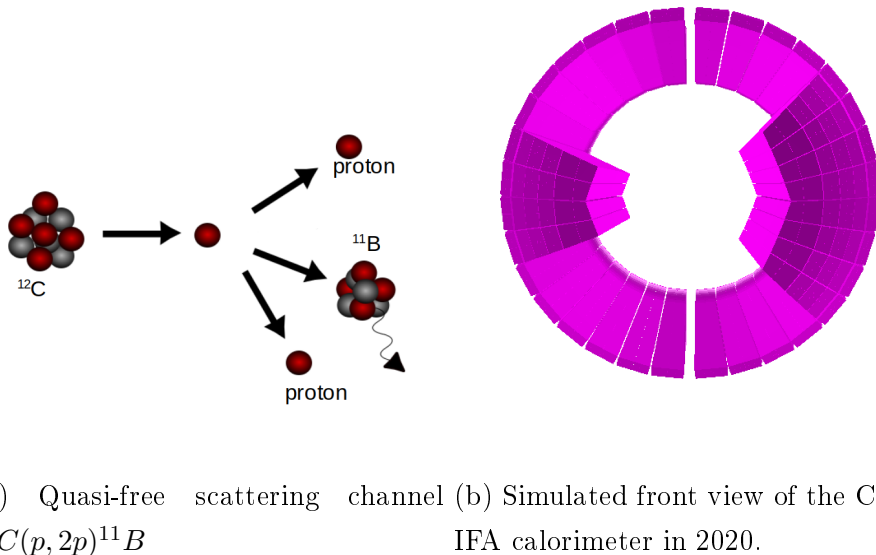


Figure 47: Tagging the  $^{12}C(p, 2p)^{11}B$  channel with only partly filled CALIFA calorimeter for the detection of the two correlated protons.

derstand the processing steps of the raw *mapped* level data to the *cal* level and finally *hit* level data. The *mapped* level data has following structure for each CALIFA hit: For an accurate proton selection and the application of appropriate cuts, it is crucial

to understand the data processing steps from the raw *mapped*-level to the *cal*-level and finally to the *hit*-level. The *mapped*-level data for each CALIFA hit is structured as follows:

- CrystalID: each crystal channel gets assigned a unique ID. Gamma range channels are in the range up to 2550, proton range ones from 2550 up to ..
- Uncalibrated Energy
- Slow Component  $N_s$ , extracted from the signal shape, see [43], section 2.
- Fast Component  $N_f$ , extracted from the signal shape, see [43], section 2.
- WRTS: White Rabbit Time Stamp[58], interpolated from FEBEX inner clock.
- Time over Threshold, optionally activated for  $\gamma$ -range channels to reconstruct energies beyond range.

The *cal*-level data is structured as in the *mapped*-level, however with calibrated energy by applying the calibration parameters from calibration run to each crystal channel.

For the calibration runs a  $^{22}Na$  (with peaks at 511keV and 1275keV) or a  $^{60}Co$  (with peaks at 1173keV and 1332keV) source is used. For each crystal channel a linear fit on the two photopeaks is performed. Using this fitting function, the uncalibrated energy, expressed in energy channels, can be converted into calibrated energy values.

For the final *hit*-level data, the energy-calibrated hits from the *cal*-level are merged into clusters. High-energy proton hits ( $E_{hit} > 15MeV$ ) and low-energy  $\gamma$  hits are first listed and sorted in descending energy order. Clusters are then formed using a cone-shaped approach, where each cluster is centered around the highest-energy hit with a half-opening angle of  $\theta_c = 14.3^\circ$ . All hits within this angular region are merged into the cluster. This process is iteratively repeated until both the high- and low-energy lists are empty. To improve the signal-to-noise ratio in this analysis, hits with energy values below the threshold of  $E_{thr} = 100keV$  are discarded during clustering.

The resulting correlations in azimuthal and polar angles, with the only cut to have at least two high energy clusters with energy larger 15 MeV, with respect to the simulated  $p2p$ -simulations are shown in figure 48 and figure 49 accordingly.

From the azimuthal correlation plot in Figure 48, the geometric acceptance limitations of CALIFA become evident. In the so-called *iPhos* region, CALIFA was instrumented only within the azimuthal ranges of  $\pm 45^\circ$  and  $157.5^\circ$  to  $202.5^\circ$ . Due to relativistic kinematics, both protons undergo a forward boost, leading to their predominant detection in the iPhos array. Consequently, any acceptance loss in this region has a substantial

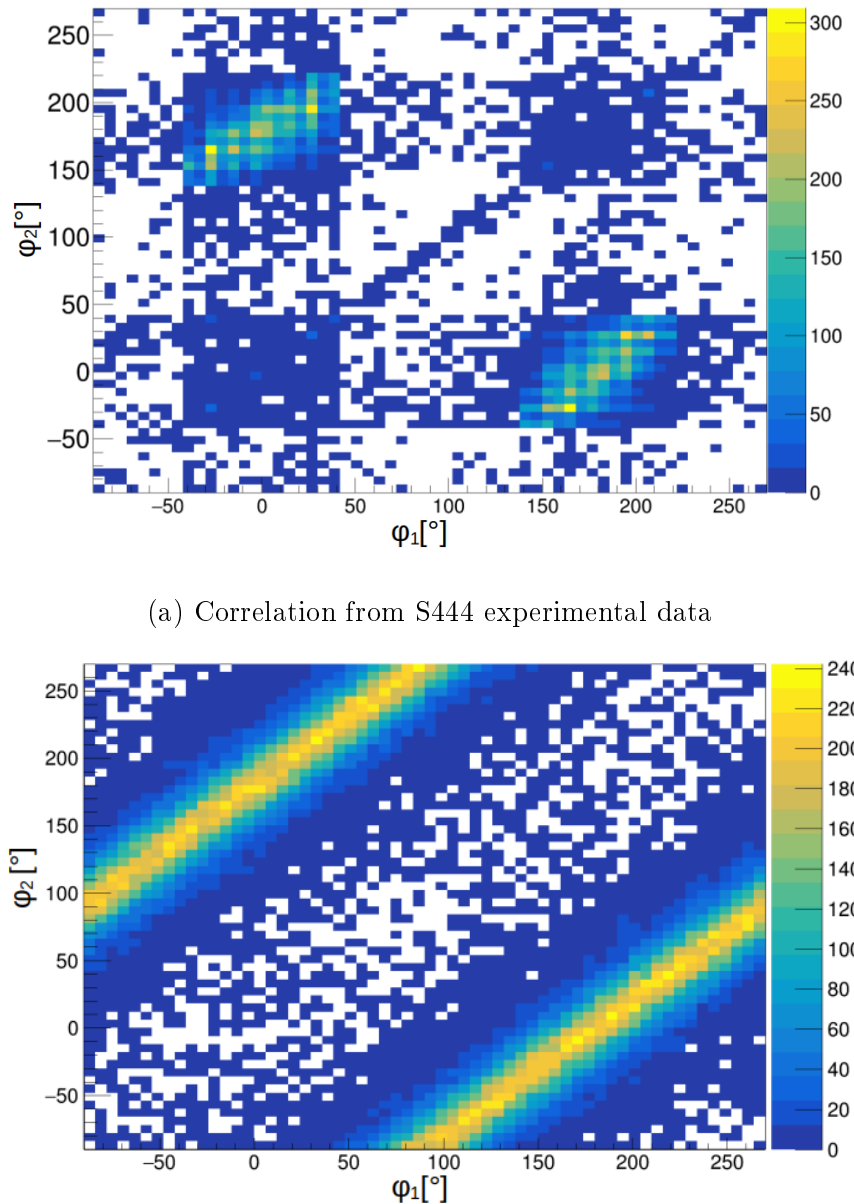


Figure 48: Azimuthal angular correlation  $\varphi_1$  versus  $\varphi_2$  of the two clusters with highest energy in CALIFA

impact on the overall detection efficiency.

Moreover, the correlation plot exhibits a distinct correlation line at  $\varphi_1 \approx \varphi_2$ . This feature primarily arises from inaccuracies in cluster reconstruction, where proton cluster hits fall outside the predefined cone size of the reconstruction algorithm, resulting in the erroneous identification of two separate hits. This effect is particularly pronounced in the *iPhos* region as it is the primary detection region for the protons. Such misidentified events are systematically excluded in analyses focusing on the clean  $^{12}C(p, 2p)^{11}B$  channel.

The polar angular correlation in figure 49 shows as expected a strong anti-correlation between the two proton clusters. For beam energies up to approximately 500 AMeV the anti-correlation line is expected to be uniformly distributed over the polar range as the momentum transfer  $t = -Q^2$ , which defines the angular distributions  $\theta_{1/2}$ , does not effect the cross section in this energy regime<sup>37</sup>.

Moreover in figure 49 the two off-diagonal lines should be noted. This artifact arises from wrong cluster reconstruction where proton cluster hits fall outside the predefined cone size of the reconstruction algorithm, resulting in the erroneous identification of two separate hits. As the resulting clusters are in close proximity, they exhibit a systematic offset from the diagonal in the polar angular correlation plot.

The information of azimuthal and polar angles of the two protons can merged in the opening angle of the two reconstructed protons via the geometric formula:

$$\theta_{p2p} = \arccos(\sin(\theta_1)\sin(\theta_2)\cos(\varphi_2 - \varphi_1) + \cos(\theta_1)\cos(\theta_2)) \quad (36)$$

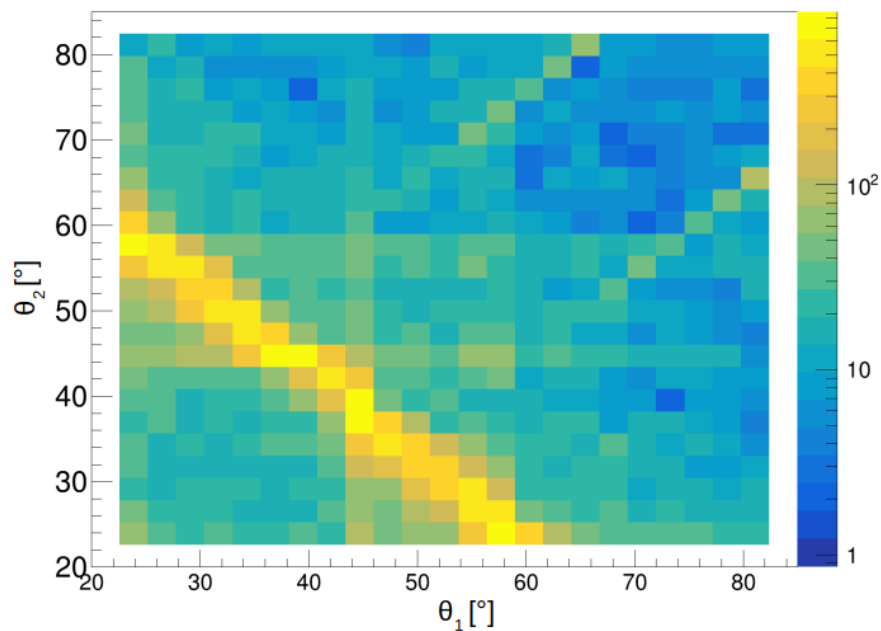
Figure 50 presents the opening angle  $\theta_{p2p}$  for the reconstructed protons. In both the simulated and experimental data, the distribution exhibits a peak at approximately 81°. While the simulated distribution shows a strict upper limit around 82°, the experimental data features a pronounced tail extending toward larger values. This effect is primarily attributed to final-state interactions (FSI) and can be significantly reduced by applying appropriate selection criteria to the polar and azimuthal angular correlations of the two reconstructed high-energy hits.

Herefore in the next considerations only events with following criteria are selected:

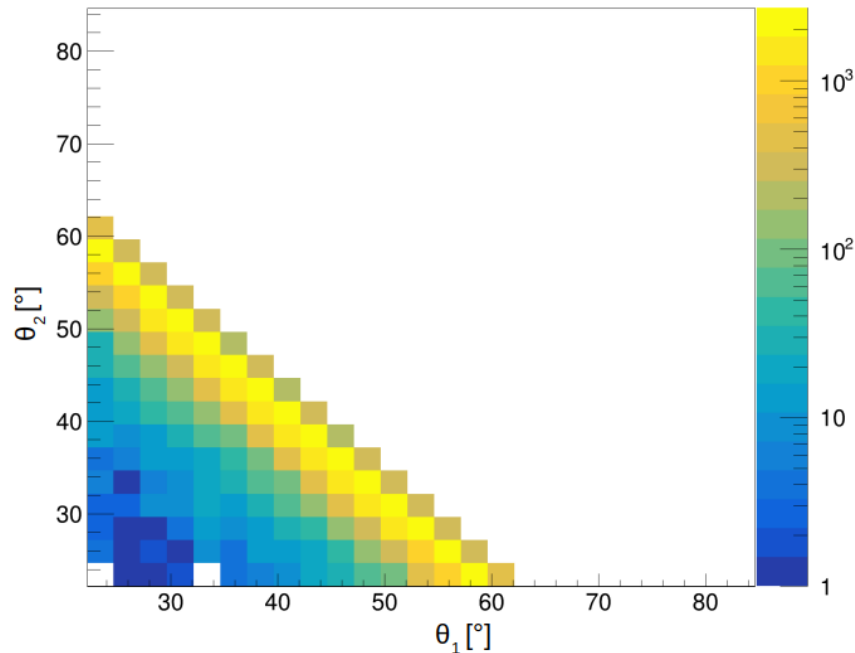
- $\theta_1 + \theta_2 < 90^\circ$
- $\Delta\varphi < 180 \pm 40^\circ$

---

<sup>37</sup>At higher beam energies, parameterizations of the cross section as a function of  $t$  often take the form  $\frac{d\sigma}{dt} = Ce^{bt}$ , where  $C$  and  $b$  are empirically determined parameters.



(a) Correlation from S444 experimental data



(b) Simulated data using based on QFS kinematical code by Leonid Chulkov, GSI.

Figure 49: Polar angular correlation  $\theta_1$  versus  $\theta_2$  of the two clusters with highest energy in CALIFA

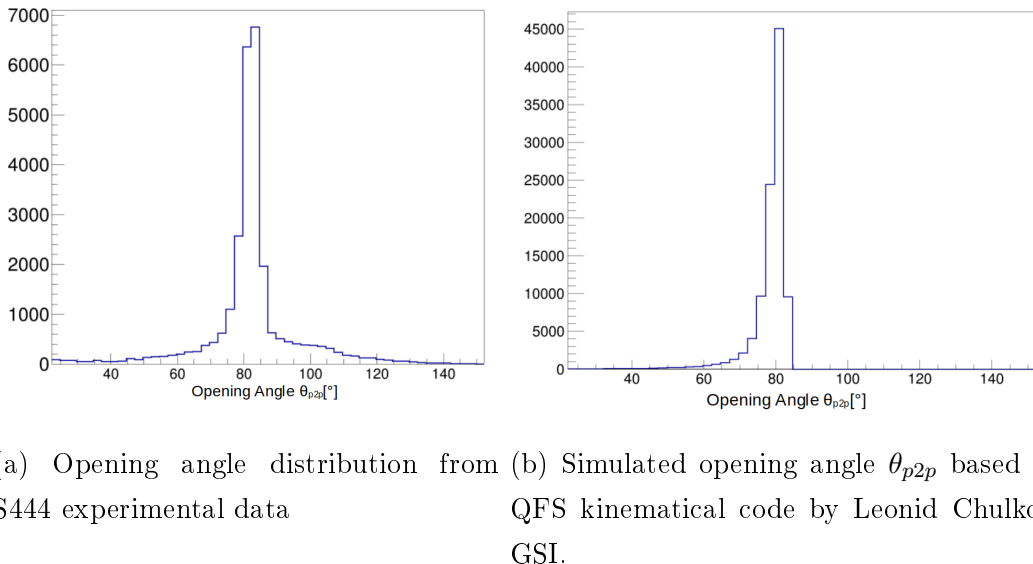


Figure 50: Reconstruction of the opening angle  $\theta_{p2p}$  as in equation 36 from the two clusters with highest energy in CALIFA

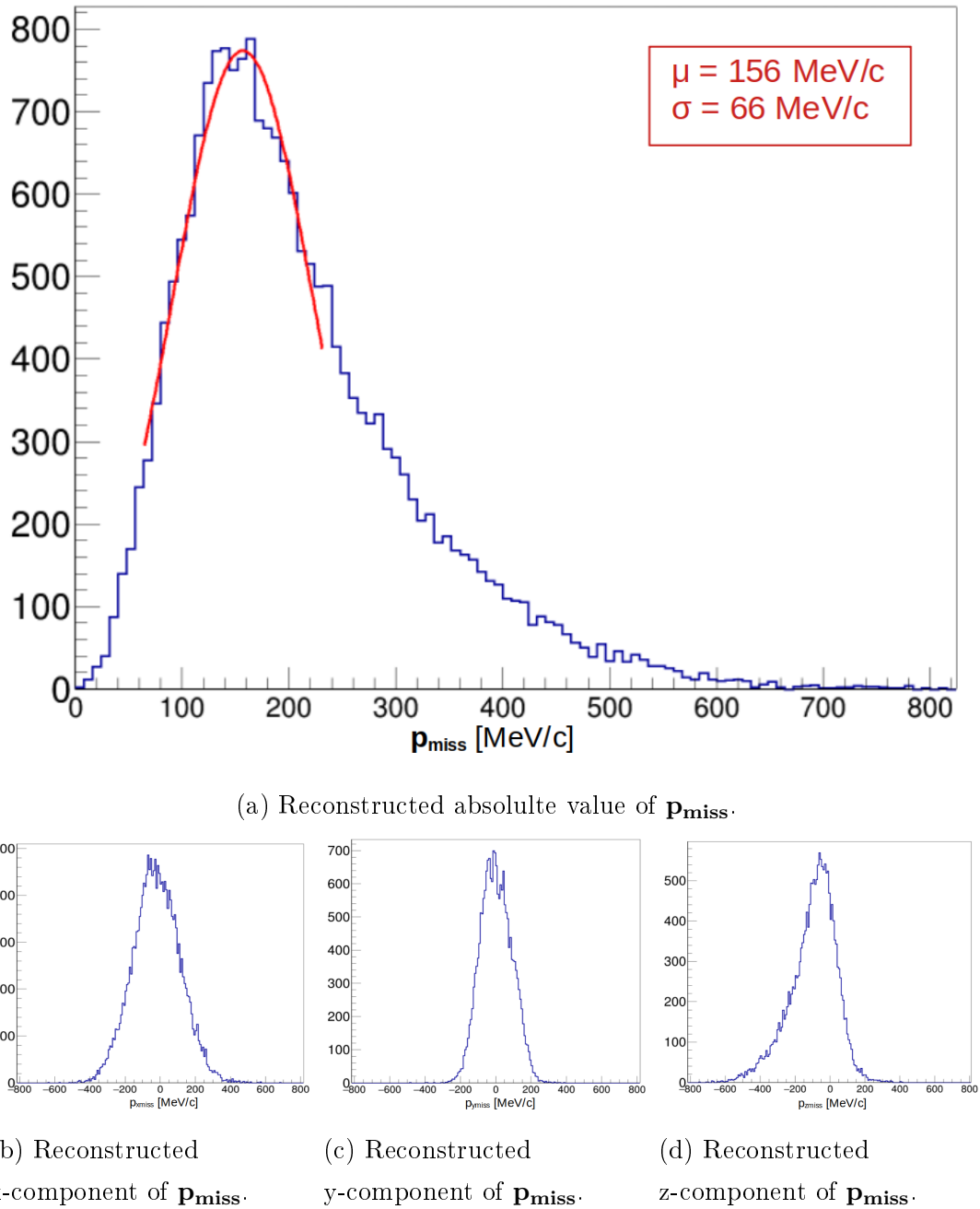
#### 5.4.1 Missing Momentum $\mathbf{p}_{\text{miss}}$ Reconstruction

As discussed in Section 2.5, the momentum of the knocked-out proton inside the  $^{12}C$  nucleus can be reconstructed, assuming higher-order perturbations are negligible, as described by Equation 4. For this reconstruction, the momenta of the two detected protons,  $\mathbf{p}_{1/2}$ , and the initial target proton,  $\mathbf{p}_0$  (which is approximately zero in the laboratory frame), must be known and transformed into the center-of-mass frame of the  $^{12}C$  nucleus. The resulting distribution of the missing momentum,  $\mathbf{p}_{\text{miss}}$ , obtained from experimental data, is presented in Figure 51.

Compared to previous experimental results, such as those reported in Ref. [59], where the measured Fermi momentum for  $^{12}C$  was determined to be  $221 \pm 5$  MeV/c, corresponding to a mean internal proton momentum of 171 MeV/c, the reconstructed mean value in the present analysis is found to be 156 MeV/c.

While this value is slightly lower than the reference, it is important to consider the specific experimental conditions. The geometric acceptance of CALIFA, particularly in the forward region, was not fully instrumented, which may introduce some distortions in the reconstructed  $\mathbf{p}_{\text{miss}}$  distribution. Nevertheless, the obtained results remain consistent within the expected systematic uncertainties.

Furthermore, the beam energy, assumed to be constant at 400, AMeV, plays a crucial role in transforming the reconstructed proton momenta into the center-of-mass frame of the  $^{12}C$  nucleus. Small variations in the actual beam energy could have a non-negligible

Figure 51: Reconstructed  $\mathbf{p}_{\text{miss}}$  and its components in the  $^{12}\text{C}$  rest frame

impact on the missing momentum reconstruction. Since no precise event-by-event beam energy information was available for this analysis, a constant value of 400 AMeV was used.

Additionally, as shown in Figure 51d, the distribution of the z-component of  $\mathbf{p}_{\text{miss}}$  exhibits a slight asymmetry, with a tail extending toward lower values. Since the z-component is particularly sensitive to deviations in the mean beam energy, this effect further contributes to the shift of the mean  $\mathbf{p}_{\text{miss}}$  value toward lower values. Future studies with improved acceptance corrections and access to event-wise beam energy measurements could further refine the results and enhance the accuracy of the  $\mathbf{p}_{\text{miss}}$  reconstruction.

#### 5.4.2 Correlations between $^{11}B$ Fragment and the reconstructed inner Proton

In Subsection 5.4.1, the momentum of the inner proton,  $\mathbf{p}_{\text{miss}}$ , was reconstructed using data exclusively from the CALIFA calorimeter. As a next step, this reconstructed momentum can be correlated with the momentum of the  $^{11}B$  fragment in the rest frame of the  $^{12}C$  nucleus.

Since the total momentum in the rest frame must be zero by definition, the momentum vectors of the inner proton and the  $^{11}B$  fragment should be directed oppositely. Consequently, the cosine of the angle  $\gamma$  between these two constituents should be approximately  $-1$ , which is confirmed by the experimental data, as shown in Figure 52a.

Furthermore, Figures 52b and 52c illustrate the correlation between the x- and y-components of  $\mathbf{p}_{\text{miss}}$  and the corresponding components of the  $^{11}B$  fragment. A strong anti-correlation is observed in both cases. While the correlation in the y-component is relatively sharp, the x-component exhibits a more blurred distribution.

This effect arises from the geometry-dependent resolution of the subdetectors:

- For the x-component, it is important to consider that only the lateral halves of CALIFA were instrumented in the *iPhos* region ( $\varphi_{1/2}$  within  $\pm 45^\circ$  and  $157.5^\circ$  to  $202.5^\circ$ ). The azimuthal resolution is moderate ( $\approx \frac{6^\circ}{\sqrt{12}}$ ), and since the x-component is reconstructed as  $\propto \cos(\varphi)$ , the derivative  $\sin(\varphi)$  remains small for  $\varphi \approx 0$ , leading to lower sensitivity in this region.
- The x-component of the  $^{11}B$  fragment is reconstructed from position measurements immediately after the target, where the lever arm for momentum recon-

struction is relatively short.

- In contrast, the y-component of the  $^{11}B$  fragment is determined from its position in MWPC3 after GLAD, where the larger lever arm improves resolution. Moreover, the y-component remains largely unaffected by the GLAD magnet, further enhancing its reconstruction accuracy.

TODO:->Maybe also correlations between fragment and proton pair, see Chulkov.

#### 5.4.3 Proton Separation Energy $S_p$

The proton separation energy  $S_p$  of  $^{12}C$  from the reaction channel  $^{12}C(p, 2p)^{11}B$  is defined by the masses and energies of the initial and final state particles in the  $^{12}C$  rest frame. One can write the full energy conservation in the rest frame of  $^{12}C$ :

$$M_{^{12}C} + \gamma \cdot m_p = E_1^* + E_2^* + (M_{^{11}B} + E_{ex}) + T_{^{11}B^*} \quad (37)$$

where  $E_1^*$  and  $E_2^*$  are total energies of the two protons in the  $^{12}C$  rest frame,  $E_{ex}$  is residual excitation in  $^{11}B$  and  $T_{^{11}B^*}$  the kinetic energy of the  $^{11}B$  in the  $^{12}C$  rest frame. Using this equation, one can express the total binding energy  $B$  of the knocked out nucleon:

$$B = S_p - E_{ex} = M_{^{12}C} - M_{^{11}B} - E_{ex} - m_p = E_1^* + E_2^* + T_{^{11}B^*} - \gamma \cdot m_p - m_p \quad (38)$$

Using Lorentz transformation from lab to  $^{12}C$  rest frame one can obtain for  $E_1^*/E_2^*$ :

$$E_{1/2}^* = \gamma \cdot m_p + \gamma \cdot T_{1/2} - \beta \cdot \gamma \cdot p_{1/2} \cdot \cos(\theta_{1/2})$$

The kinetic energy of the  $^{11}B$  in the  $^{12}C$  rest frame can be written as:

$$T_{^{11}B^*} = \frac{p_i^2}{2 \cdot M_{^{11}B}}$$

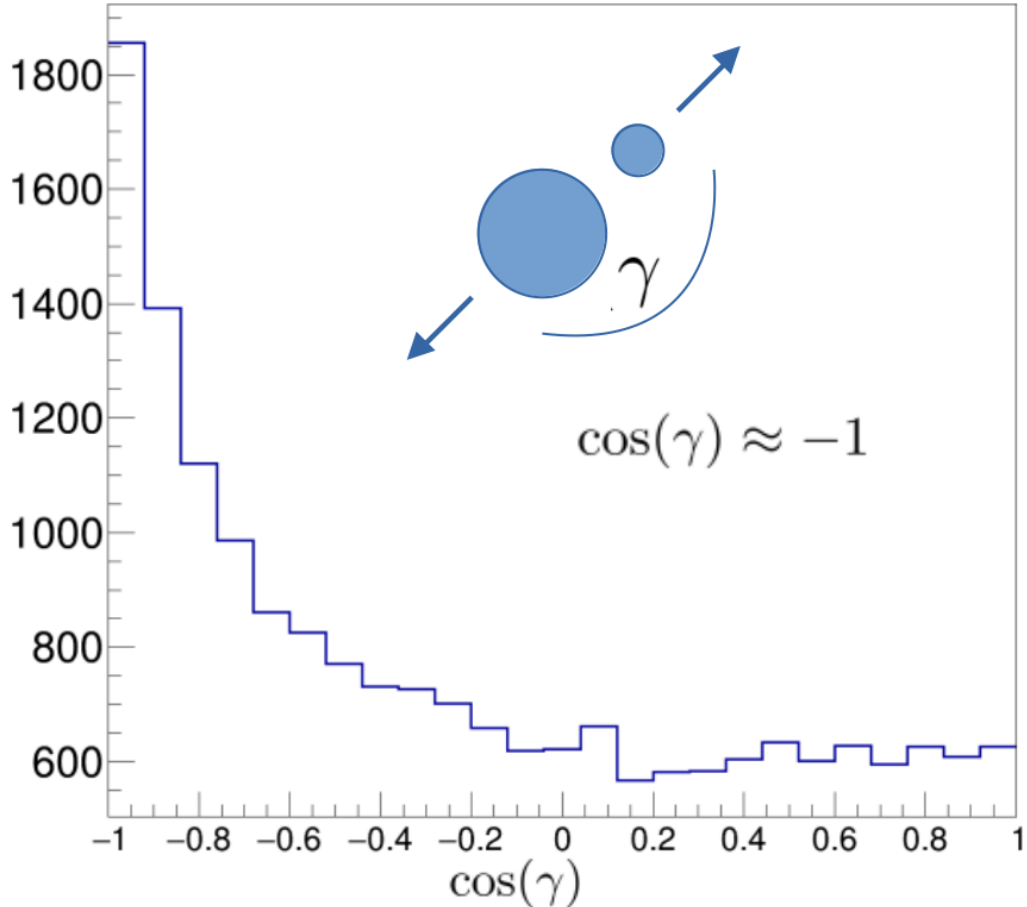
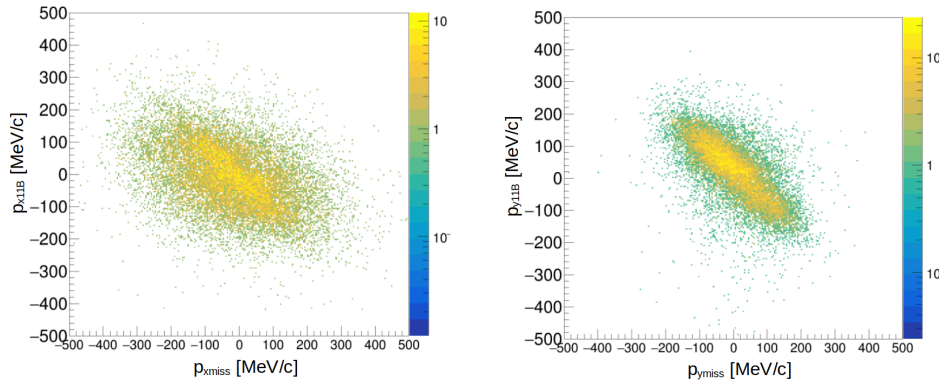
with  $p_i$  the inner momentum of the proton knocked out of the  $^{12}C$  projectile, see equation 4. Putting this in the previous equation one finally gets for the binding energy  $B$ :

$$B = (\gamma - 1) \cdot m_p + \gamma \cdot (T_1 + T_2) - \beta \cdot \gamma \cdot (p_1 * \cos(\theta_1) + p_2 * \cos(\theta_2)) + T_{^{11}B} \quad (39)$$

For  $E_{ex} = 0$ , i.e. the fragment  $^{11}B$  in the ground state, the binding energy  $B$  is equal to the one proton separation energy  $S_p$ <sup>38</sup>.

---

<sup>38</sup>Since the  $^{11}B$  fragment predominantly remains in its ground state—implying that, in most cases, the outermost protons are removed—the binding energy  $B$  and the proton separation energy  $S_p$  are used interchangeably, also due to the limited energy resolution.

(a) Cosine of the angle  $\gamma$  between inner proton and  $^{11}B$ .(b) x-component correlation between inner proton and  $^{11}B$ .(c) y-component correlation between inner proton and  $^{11}B$ .Figure 52: Correlation plots between inner proton and  $^{11}B$  in the  $^{12}C$  rest frame.

As for the S444 experiment no target detector tracking system was available. Consequently the energies as well as the azimuthal ( $\varphi$ ) and polar( $\theta$ ) angles of the two correlated protons had to be fully reconstructed using the CALIFA calorimeter. The calorimeter

provided an energy resolution  $\frac{\Delta E}{E}(@100\text{MeV}) \lesssim 1\%$ , along with angular resolutions of approximately  $\Delta\varphi \approx \frac{6^\circ}{\sqrt{12}}$ , and  $\Delta\theta \approx \frac{2^\circ}{\sqrt{12}}$ . The best way to visualize the separation energy  $S_p$  is to plot it against the summed energy of the two protons in the  $^{12}\text{C}$  rest frame as shown in figure 53. Two vertical lines are visible. They correspond to the two QFS-reaction types within the  $\text{CH}_2$  target: the proton within the  $^{12}\text{C}$  projectile can either scatter on the hydrogen (proton-like) part or on the carbon part of the plastic target. For the first case only the separation energy  $S_p$  as derived in equation 5.4.3 is necessary to remove the proton of the projectile within the  $^{12}\text{C}$  nucleus. In the second case the QFS-reaction is between two protons both bound within a carbon nucleus – the projectile carbon and the target carbon part. Therefore more energy is needed to free both protons from their nuclear bond. This corresponds to the left vertical line in figure 53. It should be noted that the reconstructed one-proton separation energy  $S_p$  is shifted with respect to the mean value of  $\approx 16\text{MeV}$ . For a precise measurement the accurate position of the target and the reaction vertex would be needed, as well as a precise measurement of the kinetic energy of the incoming  $^{12}\text{C}$  would be required (for the actual measurements the beam energy value was set to  $400\text{AMeV}$ ).

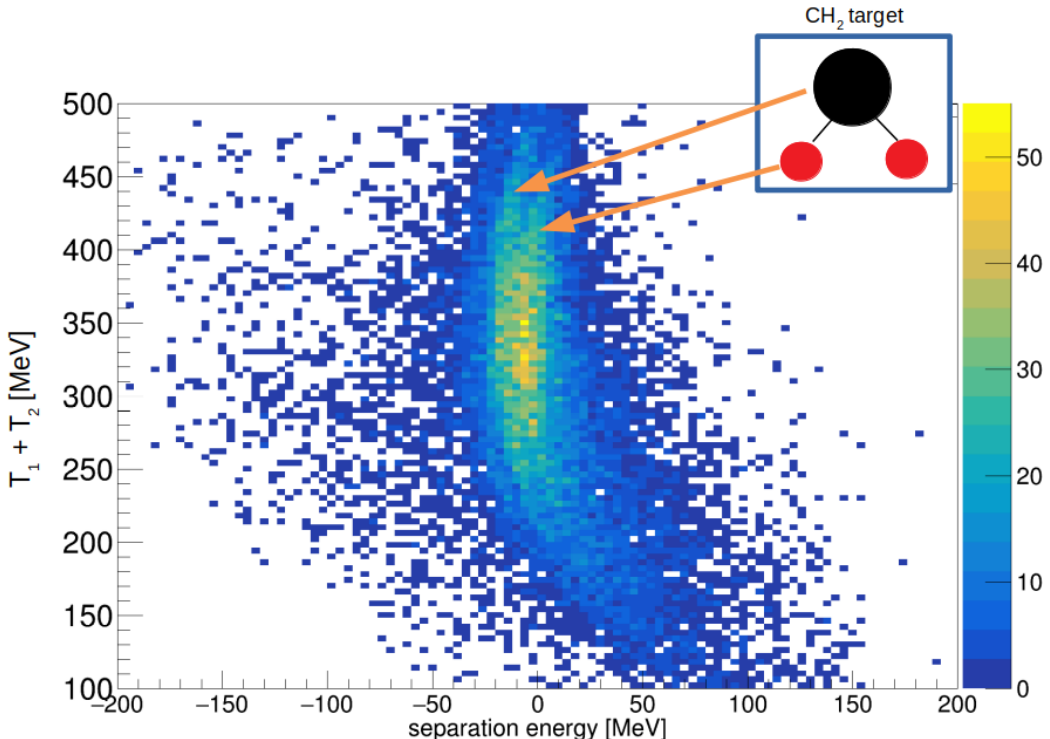


Figure 53: Sum of the kinetic energies of the two correlated protons ( $T_1/T_2$ ) versus the one proton separation energy  $S_p$ . Since this energy is needed to solve the proton from the nucleus' core, its value has conventionally a negative sign.

## 5.5 Reconstruction of excited $^{11}B$ states

->Show level scheme of  $^{11}B$ , explain excited states and why it is not expected to see any peaks at 4.4 MeV. ->Explain Doppler correction (this is really the key point of the CALIFA, why it is highly segmented) -> show all conditions that you apply -> This comm. exp. has shown that we can really pin down reaction mechanism and we are ready for exciting p2p experiments -> Limitations: CALIFA was only partly filled for this exp.

## 5.6 Fission via Quasi-Free Scattering reaction

In 2021, the S455 experiment conducted at the R<sup>3</sup>B experiment marked a significant advancement in experimental nuclear physics through the realization of an unprecedented fission study employing quasi-free scattering as a reaction mechanism. This approach induces fission via particle-hole excitations, which can span excitation energies from a few MeV up to several tens of MeV.

Over the past decades, Coulomb-induced fission reactions in inverse kinematics have served as a powerful tool to investigate fission dynamics and the nuclear structure of both stable and unstable heavy nuclei at large deformations. These reactions, however, provide only averaged information over many fission events, thereby limiting their ability to resolve the detailed topography of the potential-energy surface (PES). Consequently, they offer only indirect access to the fission barrier through measurements of integrated fission yields, making it difficult to probe finer aspects of fission dynamics. Coulomb-induced fission has confirmed the broad features predicted by macroscopic models such as the liquid-drop model, which typically exhibits a single, smooth rise in the PES leading to fission, as illustrated in Figure 1. However, when microscopic effects—such as nuclear shell corrections and pairing interactions—are taken into account, the PES becomes substantially more complex and requires higher-resolution experimental techniques for validation.

To test these more nuanced theoretical predictions, a detailed and differential mapping of the PES is necessary. Fission induced via QFS reactions offers a promising experimental approach for this purpose. In QFS-induced fission, the projectile interacts with an individual nucleon within the target nucleus, leading to localized and controlled excitation of the residual system. This allows for event-by-event measurement of the fission process, enabling a direct correlation between the excitation energy and the resulting fission fragment charge and mass distributions, as well as the fission probabilities.

Such differential data facilitate a more precise determination of the temperature dependence of the fission process and the underlying fission barrier heights for exotic,

neutron-rich heavy nuclei. By systematically analyzing these correlations, QFS-induced fission can provide critical constraints on theoretical models of the PES and improve our understanding of fission dynamics far from stability.

-> shortly explain the challenges behind, idea should be in the theory part. Also mention that this was complementary experiment to Coulex Exp, where nature paper was submitted -> mention that TUM Munich group was strongly involved -> Charge reconstruction is done, mention the papers and publications -> One really interesting aspect would have been to pick out specific reaction channels, eg. with one fission fragment being a thin isotope and look at the gamma spectrum. -> the issue there is of course that precise thin isotope cannot be selected yet. But from CALIFA side this was motivation to improve the clustering algorithm, especially for fission reactions, where you have lot more hits in CALIFA. And there especially looking at low energy hits from gammas, which can be quite sparse. -> This should then be the introduction for the next section about clustering.

## 6 Machine Learning for the Cluster Reconstruction in the CALIFA Calorimeter at R<sup>3</sup>B

shortly recapitulate how the clustering is done Motivate with single/double escape peak stuff Mention that we have time information in CALIFA but we do not use it WORK IN PROGRESS WITH PAPER WRITING

### 6.1 Data Simulation and Selection

### 6.2 Agglomerative Clustering Model

### 6.3 "Edge Model" - Graphical NN

#### 6.3.1 Combination of both methods

### 6.4 Results

# Appendices

## A TWIN MUSIC Geometric Acceptance Correction via Efficiency Measurement

Instead of correcting the limited geometric acceptance of TWIN MUSIC via graphical fitting (see section 4.4) it is also feasible correcting via TWIN MUSIC efficiency measurement. The correction factor is given by:

$$\epsilon_{geo\_corr} = \frac{N_{MWPC1,MWPC2}}{N_{MWPC1,MWPC2,TWIN}} \quad (40)$$

where  $N_{MWPC1,MWPC2}$  corresponds to the number of events with a hit in MWPC1 and MWPC2 whereas  $N_{MWPC1,MWPC2,TWIN}$  imposes the further condition having a hit in TWIN MUSIC too.

The corresponding correction factor  $\epsilon_{geo\_corr}$  is consequently applied on all target and empty runs. The resulting corrected charge changing cross section is shown in figure 54. The same correction factor can be applied to the total interaction cross section as

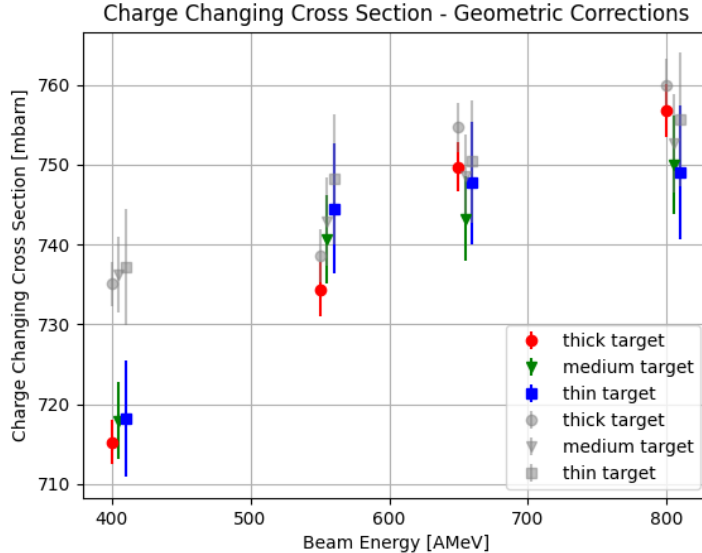


Figure 54: Charge changing cross section correction due to limited geometric acceptance of TWIN MUSIC via efficiency correction with MWPC1 and MWPC2. In gray: charge changing cross section measurements before applying corrections, as in figure 26

in figure 55.

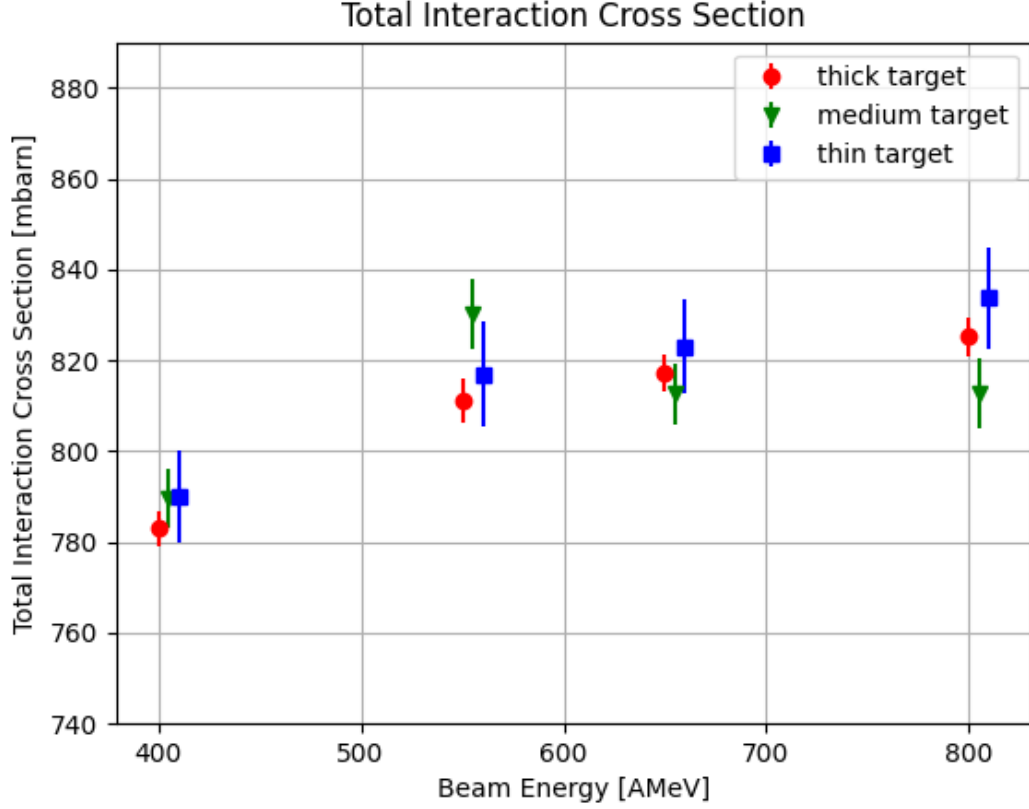


Figure 55: Total interaction cross section of  $^{12}\text{C} + ^{12}\text{C}$  using the TWIN MUSIC efficiency correction factor, see equation 40, to compensate for the limited geometric acceptance in TWIN MUSIC.

## B Flight-Path Reconstruction

The first step in the radius and flightpath reconstruction is expressing the entrance point on the GLAD field  $(z_1, x_1)$  and the exit point  $(z_2, x_2)$  with the center of the circle path  $(z_0, x_0)$  as reference, see figure 56:

$$\begin{aligned}
 z_1 &= z_0 - r \cos(90^\circ - \theta_i) = z_0 - r \sin(\theta_i) \\
 x_1 &= x_0 + r \sin(90^\circ - \theta_i) = x_0 + r \cos(\theta_i) \\
 z_2 &= z_0 + r \cos(90^\circ - \theta_o) = z_0 + r \sin(\theta_o) \\
 x_2 &= x_0 + r \sin(90^\circ - \theta_o) = x_0 + r \cos(\theta_o)
 \end{aligned}$$

The slope  $m_1$  of the intersection line between  $(z_1, x_1)$  and  $(z_2, x_2)$  is given by:

$$m_1 = \frac{x_2 - x_1}{z_2 - z_1} = \frac{\cos(\theta_o) - \cos(\theta_i)}{\sin(\theta_o) + \sin(\theta_i)}$$

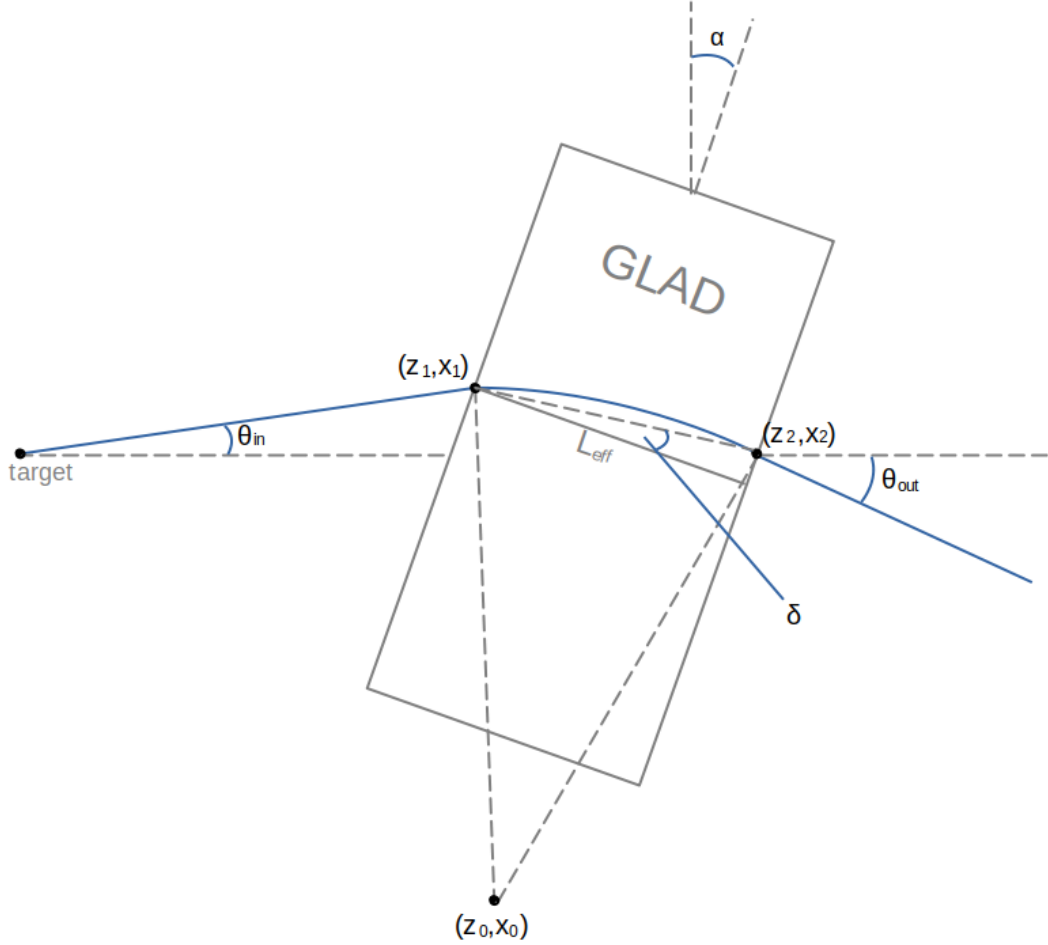


Figure 56: Flightpath reconstruction with reference positions  $(z_0, x_0)$ ,  $(z_1, x_1)$  and  $(z_2, x_2)$ . The GLAD magnet is tilted by  $\alpha = 14^\circ$ .

and with the distance between the two points given by:

$$\begin{aligned}\Delta_{i/o}^2 &= r^2 \left[ (\cos\theta_o - \cos\theta_i)^2 + (\sin\theta_o + \sin\theta_i)^2 \right] \\ &= 4r^2 \sin^2\left(\frac{\theta_i}{2} + \frac{\theta_o}{2}\right) \\ \Rightarrow \Delta_{i/o} &= 2r \sin\left(\frac{\theta_i}{2} + \frac{\theta_o}{2}\right)\end{aligned}$$

To describe the distance between  $(z_1, x_1)$  and  $(z_2, x_2)$  with the given effective GLAD length  $L_{eff}$  ( $= 2.06\text{ m}$ ) the tilting angle  $\alpha$  (see figure 56) of GLAD in relation to the incoming beam line direction has to be considered. Consequential the angle  $\delta$  between the trajectory connecting  $(z_1, x_1)$  and  $(z_2, x_2)$  and the line parallel to the GLAD magnet

width  $L_{eff}$  can be determined as:

$$\tan(\delta) = \left| \frac{m_1 - m_2}{1 + m_1 \cdot m_2} \right|$$

with  $m_2 = -\tan(\alpha)$ :

$$\delta = \text{atan} \left( \frac{\frac{\cos\theta_o - \cos\theta_i}{\sin\theta_o + \sin\theta_i} + \tan\alpha}{1 - \frac{\cos\theta_o - \cos\theta_i}{\sin\theta_o + \sin\theta_i} \cdot \tan\alpha} \right)$$

The final relation between  $L_{eff}$  and the bending radius  $r$  of the fragment within GLAD can be written as:

$$\begin{aligned} L_{eff} &= 2r \sin\left(\frac{\theta_i}{2} + \frac{\theta_o}{2}\right) \cdot \cos\delta \\ &= 2r \sin\left(\frac{\theta_i}{2} + \frac{\theta_o}{2}\right) \cdot \frac{1}{\sqrt{\delta^2 + 1}} \end{aligned} \quad (41)$$



## References

- [1] O. Chamberlain and E. Segrè, “Proton-proton collisions within lithium nuclei,” *Physical Review*, vol. 87, no. 1, p. 81, 1952.
- [2] J. Cladis, W. Hess, and B. Moyer, “Nucleon momentum distributions in deuterium and carbon inferred from proton scattering,” *Physical Review*, vol. 87, no. 3, p. 425, 1952.
- [3] T. Maris, P. Hillman, and H. Tyrén, “Quasi-elastic scattering and nuclear structure,” *Nuclear Physics*, vol. 7, pp. 1–9, 1958.
- [4] M. Patsyuk, J. Kahlbow, G. Laskaris, M. Duer, V. Lenivenko, E. Segarra, T. Atovullaev, G. Johansson, T. Aumann, A. Corsi, *et al.*, “Unperturbed inverse kinematics nucleon knockout measurements with a carbon beam,” *Nature physics*, vol. 17, no. 6, pp. 693–699, 2021.
- [5] P. Hansen and J. Tostevin, “Direct reactions with exotic nuclei,” *Annual Review of Nuclear and Particle Science*, vol. 53, no. 1, pp. 219–261, 2003.
- [6] W. Dickhoff and C. Barbieri, “Self-consistent green’s function method for nuclei and nuclear matter,” *Progress in Particle and Nuclear Physics*, vol. 52, no. 2, pp. 377–496, 2004.
- [7] A. S. Goldhaber, “Statistical models of fragmentation processes,” *Physics Letters B*, vol. 53, no. 4, pp. 306–308, 1974.
- [8] H. Feshbach and K. Huang, “Fragmentation of relativistic heavy ions,” *Physics Letters B*, vol. 47, no. 4, pp. 300–302, 1973.
- [9] L. Chulkov, F. Aksouh, A. Bleile, O. Bochkarev, D. Cortina-Gil, A. Dobrovolsky, P. Egelhof, H. Geissel, M. Hellström, N. Isaev, *et al.*, “Quasi-free scattering with 6, 8he beams,” *Nuclear Physics A*, vol. 759, no. 1-2, pp. 43–63, 2005.
- [10] V. Panin, T. Aumann, and C. Bertulani, “Quasi-free scattering in inverse kinematics as a tool to unveil the structure of nuclei: A tribute to mahir s. hussein,” *The European Physical Journal A*, vol. 57, pp. 1–13, 2021.
- [11] L. Atar, S. Paschalis, C. Barbieri, C. A. Bertulani, P. Díaz Fernández, M. Holl, M. A. Najafi, V. Panin, H. Alvarez-Pol, T. Aumann, *et al.*, “Quasifree ( $p, 2 p$ ) reactions on oxygen isotopes: observation of isospin independence of the reduced single-particle strength,” *Physical review letters*, vol. 120, no. 5, p. 052501, 2018.

- [12] M. Hjorth-Jensen, “The carbon challenge,” *Physics*, vol. 4, p. 38, 2011.
- [13] K. Sumiyoshi and G. Roepke, “Appearance of light clusters in post-bounce evolution of core-collapse supernovae,” *Physical Review C Nuclear Physics*, vol. 77, no. 5, p. 055804, 2008.
- [14] J. Mabiala, A. Cowley, S. Förtisch, E. Buthelezi, R. Neveling, F. Smit, G. Steyn, and J. Van Zyl, “Analyzing power and cross section distributions of the c 12 (p, p α) be 8 cluster knockout reaction at an incident energy of 100 mev,” *Physical Review C Nuclear Physics*, vol. 79, no. 5, p. 054612, 2009.
- [15] L. Johannsen, A. Jensen, and P. Hansen, “The 11li nucleus as a three-body system,” *Physics Letters B*, vol. 244, no. 3-4, pp. 357–362, 1990.
- [16] H. Simon, D. Aleksandrov, T. Aumann, L. Axelsson, T. Baumann, M. Borge, L. Chulkov, R. Collatz, J. Cub, W. Dostal, *et al.*, “Direct experimental evidence for strong admixture of different parity states in 11 li,” *Physical review letters*, vol. 83, no. 3, p. 496, 1999.
- [17] C. Bertulani and M. S. Hussein, “Geometry of borromean halo nuclei,” *Physical Review C Nuclear Physics*, vol. 76, no. 5, p. 051602, 2007.
- [18] W. Xing, X.-G. Wang, and A. W. Thomas, “Electromagnetic form factors for nucleons in short-range correlations,” *Physics Letters B*, vol. 846, p. 138195, 2023.
- [19] “Probing high-momentum protons and neutrons in neutron-rich nuclei,” *Nature*, vol. 560, no. 7720, pp. 617–621, 2018.
- [20] S. Paschalis, M. Petri, A. Macchiavelli, O. Hen, and E. Piasetzky, “Nucleon-nucleon correlations and the single-particle strength in atomic nuclei,” *Physics Letters B*, vol. 800, p. 135110, 2020.
- [21] G. García-Jiménez, H. Alvarez-Pol, A. Graña-González, J. Rodríguez-Sánchez, J. Benlliure, D. Cortina-Gil, L. Atar, L. Audouin, G. Authelet, A. Besteiro, *et al.*, “Study of (p, 2p) fission reactions in inverse kinematics using the r3b set-up,” in *EPJ Web of Conferences*, vol. 290, p. 02009, EDP Sciences, 2023.
- [22] J. Graña-González, J. Rodríguez-Sánchez, J. Benlliure, G. García-Jiménez, H. Alvarez-Pol, D. Cortina-Gil, L. Atar, L. Audouin, G. Authelet, A. Besteiro, *et al.*, “Fission studies in inverse kinematics with the r3b setup,” in *EPJ Web of Conferences*, vol. 290, p. 02015, EDP Sciences, 2023.

- [23] J. Gerl, “Nuclear spectroscopy studies at gsi—from rising to hispec/despec.,” *Acta Physica Polonica B*, vol. 40, no. 3, 2009.
- [24] T. Galatyuk, H. Collaboration, *et al.*, “Hades overview,” *Nuclear Physics A*, vol. 931, pp. 41–51, 2014.
- [25] H.-J. Kluge, T. Beier, K. Blaum, L. Dahl, S. Eliseev, F. Herfurth, B. Hofmann, O. Kester, S. Koszudowski, C. Kozhuharov, *et al.*, “Hitrap: a facility at gsi for highly charged ions,” *Advances in Quantum Chemistry*, vol. 53, pp. 83–98, 2008.
- [26] Z. Major, U. Eisenbarth, B. Zielbauer, C. Brabetz, J. Ohland, Y. Zobus, S. Roeder, D. Reemts, S. Kunzer, S. Götte, *et al.*, “High-energy laser facility phelix at gsi: latest advances and extended capabilities,” *High Power Laser Science and Engineering*, vol. 12, p. e39, 2024.
- [27] C. E. Düllmann, M. Block, F. P. Heßberger, J. Khuyagbaatar, B. Kindler, J. V. Kratz, B. Lommel, G. Münzenberg, V. Pershina, D. Renisch, *et al.*, “Five decades of gsi superheavy element discoveries and chemical investigation,” *Radiochimica Acta*, vol. 110, no. 6-9, pp. 417–439, 2022.
- [28] “Starting point of the gsi accelerator facility: Ion sources.” Accessed: 2025-04-03.
- [29] “Ring accelerator sis18—the record holder.” Accessed: 2025-04-03.
- [30] C. Nociforo, “Time-of-flight measurements at the super-frs,” *Journal of Instrumentation*, vol. 9, no. 01, p. C01022, 2014.
- [31] L. Ponnath, T. Aumann, C. Bertulani, R. Gernhäuser, M. Heil, T. Almusidi, H. Alvarez-Pol, L. Atar, L. Atkins, Y. Ayyad, *et al.*, “Measurement of nuclear interaction cross sections towards neutron-skin thickness determination,” *Physics Letters B*, vol. 855, p. 138780, 2024.
- [32] G. Charpak, R. Bouclier, T. Bressani, J. Favier, and Č. Zupančič, “The use of multiwire proportional counters to select and localize charged particles,” *Nuclear Instruments and Methods*, vol. 62, no. 3, pp. 262–268, 1968.
- [33] J.-F. Martin, J. Taïeb, G. Boutoux, A. Chatillon, T. Gorbinet, E. Pellereau, L. Audouin, A. Heinz, H. Alvarez-Pol, Y. Ayyad, *et al.*, “Fission-fragment yields and prompt-neutron multiplicity for coulomb-induced fission of u 234, 235 and np 237, 238,” *Physical Review C*, vol. 104, no. 4, p. 044602, 2021.

- [34] GSI Helmholtzzentrum für Schwerionenforschung GmbH, “Large-acceptance dipole magnet glad.” [https://www.gsi.de/fileadmin/Kernreaktionen/GLAD\\_in\\_CaveC.jpg](https://www.gsi.de/fileadmin/Kernreaktionen/GLAD_in_CaveC.jpg), 2013. [Online; accessed September 09, 2024].
- [35] “Technical report for the design, construction and commissioning of the califa barrel.” [https://igfae.usc.es/~r3b/documentos/TDR/CALIFA\\_BARREL\\_TDR.pdf](https://igfae.usc.es/~r3b/documentos/TDR/CALIFA_BARREL_TDR.pdf). Accessed: 2024-09-24.
- [36] M. Bendel, *Entwicklung einer neuartigen Nachweismethode hochenergetischer Teilchen im CALIFA-Kalorimeter*. Dr., Technische Universität München, München, 2014. Technische Universität München, Diss., 2014.
- [37] “Technical report for the design, construction and commissioning of the califa endcap.” [https://edms.cern.ch/ui/file/1833748/2/TDR\\_R3B\\_CALIFA\\_ENDCAP\\_public.pdf](https://edms.cern.ch/ui/file/1833748/2/TDR_R3B_CALIFA_ENDCAP_public.pdf). Accessed: 2024-09-24.
- [38] R. Murray and A. Meyer, “Scintillation response of activated inorganic crystals to various charged particles,” *Physical Review*, vol. 122, no. 3, p. 815, 1961.
- [39] S. Zazubovich, “Physics of halide scintillators,” *Radiation Measurements*, vol. 33, no. 5, pp. 699–704, 2001.
- [40] M. Bendel, *Entwicklung einer neuartigen Nachweismethode hochenergetischer Teilchen im CALIFA-Kalorimeter*. PhD thesis, Technische Universität München, 2014.
- [41] I. Holl, E. Lorenz, and G. Mageras, “A measurement of the light yield of common inorganic scintillators,” *IEEE Transactions on Nuclear Science*, vol. 35, no. 1, pp. 105–109, 1988.
- [42] A. Syntfeld-Kazuch, L. Swiderski, W. Czarnacki, M. Gierlik, W. Klamra, M. Moszynski, and P. Schotanus, “Non-proportionality and energy resolution of csi (tl),” *IEEE Transactions on Nuclear Science*, vol. 54, no. 5, pp. 1836–1841, 2007.
- [43] M. Winkel, *Implementierung und Erprobung einer digitalen Pulsformanalyse zur Auslese von Kalorimetern*. PhD thesis, Diplomarbeit, 2011.
- [44] M. O. Winkel, *Komplexe Pulsformalgorithmen und Teilchenidentifikation zur Echtzeit-Implementierung in CALIFA*. PhD thesis, Technische Universität München, 2016.

- [45] A.-L. Hartig, “Evolution of califa: From single detector modules to benchmark reactions,”
- [46] “Mesytec.” <https://www.mesytec.com/>. [Online; accessed September 29, 2024].
- [47] “Febex 3b-front end board with optical link extension.” <https://www.gsi.de/fileadmin/EE/Module/FEBEX/febex3b.pdf>. [Online; accessed September 30, 2024].
- [48] K. Philipp, *Gamma detection with CALIFA*. PhD thesis, Technische Universität München, 2024.
- [49] GSI Helmholtzzentrum für Schwerionenforschung GmbH, “Exploder.” <https://www.gsi.de/en/work/forschung/experimentelektronik/digitalelektronik/digitalelektronik/module/lwl/exploder>. [Online; accessed September 30, 2024].
- [50] A. Bail, J. Taieb, A. Chatillon, G. Belier, B. Laurent, and E. Pellereau, “Time of flight measurement on the sofia experiment,” in *2011 2nd International Conference on Advancements in Nuclear Instrumentation, Measurement Methods and their Applications*, pp. 1–4, IEEE, 2011.
- [51] K. Boretzky, I. Gašparić, M. Heil, J. Mayer, A. Heinz, C. Caesar, D. Kresan, H. Simon, H. T. Törnqvist, D. Körper, *et al.*, “Neuland: The high-resolution neutron time-of-flight spectrometer for r3b at fair,” *Nuclear Instruments and Methods in Physics Research Section A: Accelerators, Spectrometers, Detectors and Associated Equipment*, vol. 1014, p. 165701, 2021.
- [52] K. Boretzky, G. Alkazov, L. Atar, T. Aumann, and C. Beinrucker, “Neuland-from double-planes to the demonstrator,” *GSI Sci. Rep.*, vol. 200, p. 2015, 2014.
- [53] L. Ponnath, *Precise Measurement of Nuclear Interaction Cross Sections with R3B*. PhD thesis, Technische Universität München, 2023.
- [54] “Mdpp-16 detector readout systems, mesytec.” <https://www.mesytec.com/products/nuclear-physics/MDPP-16.html>. [Online; accessed October 18, 2024].
- [55] K. Lau and J. Pyrlik, “Optimization of centroid-finding algorithms for cathode strip chambers,” *Nuclear Instruments and Methods in Physics Research Section A: Accelerators, Spectrometers, Detectors and Associated Equipment*, vol. 366, no. 2-3, pp. 298–309, 1995.

- [56] O. Bertini, *Study of 3 Lambda H and 4 Lambda H in the reaction of 6 Li+ 12 C at 2 A GeV.* PhD thesis, Dissertation, Mainz, Johannes Gutenberg-Universität Mainz, 2013.
- [57] E. Bayer and M. Traxler, “Development of a high-resolution ( $< 10$  ps rms) 32-channel tdc in a field-programmable-gate-arrays,” *Instruments-Methods-45, GSI Scientific Report 2009*, p. 325, 2009.
- [58] J. Serrano, M. Lipinski, T. Wlostowski, E. Gousiou, E. van der Bij, M. Cattin, and G. Daniluk, “The white rabbit project,” 2013.
- [59] E. J. Moniz, I. Sick, R. Whitney, J. Ficenec, R. D. Kephart, and W. Trower, “Nuclear fermi momenta from quasielastic electron scattering,” *Physical Review Letters*, vol. 26, no. 8, p. 445, 1971.